SYNTHESIS AND CHARACTERIZATION OF NANO-HYBRID SYSTEMS WITH INDUCED POROSITIES VIA ICE TEMPLATION

A Dissertation

Presented to the Faculty of the Graduate School

of Cornell University

In Partial Fulfillment of the Requirements for the Degree of

Doctor of Philosophy

by

Luis Estevez

August 2013

SYNTHESIS AND CHARACTERIZATION OF NANO-HYBRID SYSTEMS WITH INDUCED POROSITIES VIA ICE TEMPLATING

Luis Estevez, Ph.D.

Cornell University 2013

Inorganic-organic hybrid systems are a class of materials that can combine the properties of each constituent material into novel materials with properties that are enhanced or even obtainable where previously unattainable. At nano length scales, these properties can be enhanced via various nano-effects that enable these materials to be tailorable to specific applications. When ice templating (a technique that induces porosity via a sacrificial ice template) is combined with these nano-hybrid systems, a new class of porous materials becomes available that can be imbued with targeted properties as required by the specific application. This dissertation focuses on using these techniques to synthesize novel materials with prerequisite properties as well as to fabricate nano-hybrid porous systems to be used as intermediate precursor materials.

This dissertation will first describe work focused on the catalyst layer in PEM fuel cells. In these fuels cells, there is a classic materials science problem where there is a need for a particular material that can accomplish multiple tasks at once. To synthesize a material with all of the prerequisite properties, traditional nanocomposite techniques were combined with ice templating and a dual in situ reduction technique to produce an interconnected porous nano-hybrid scaffold with electrical conductivity (graphene sheets), ionic conductivity (Nafion) and catalytic platinum nanoparticles.

Next, the dissertation will focus on ice templating techniques applied to carbon systems to synthesize hierarchical porous carbon (HPC) materials. This new family of carbon materials has a hierarchical porosity across all three length scales (micro-, meso and macro-) and enable the HPCs to have tunable porosities across all three pore length scales. The consequent material is an open, vascular network of interconnected macropores, whose pore walls are made up of mesopores and micropores. This results in a material with easy ingress/egress to the high surface area (up to 2000+ m^2/g) meso/micropores by way of the interconnected macroporous network. Finally, initial results of applications for the HPCs will be explored including electric double layer capacitors (EDLCs), Li-sulfur batteries, and scaffolds for CO_2 capture. In this regard, the HPCs showed an excellent capability to be used as effective EDLC electrodes with a maximum charge storage capability of 6 W·h/kg and a maximum power density of 14 kW/kg. When used as a carbon support for a Li-S battery cathode, a charge capacity of roughly 600 mAh/g_{sulfur} at a relatively high charge/discharge rate of 1C was obtained, while maintaining good columbic efficiency (> 85%). The HPCs also demonstrated an exceptional ability when used as scaffolds for amine based CO_2 capture, achieving a maximum CO_2 capacity of 4.2 mmol/g.

BIOGRAPHICAL SKETCH

Luis Estevez was born and raised in New York City, in Queens. He was brought up with a younger brother and sister as first generation Americans, after both his parents immigrated to America from different countries (his mother from Chile and his father from Spain). Lou went to work in the family restaurant business at a young age following his dad into the kitchen peeling potatoes, eventually working his way up to maître de, while helping his parents in the running of the family business.

After running the restaurant for roughly six years, meeting and speaking to many clients with varied careers, Lou realized a career in engineering appealed to him. He was always fascinated with how devices worked and had enjoyed the sciences and especially loved mathematics, so a career in mechanical engineering seemed to make the most sense. Lou spoke with his girlfriend (now his wife) Erin about it, worried that maybe his chance had passed him by, but Erin convinced Lou that it was not too late to pursue his dreams and thus Lou was inspired to pursue his dream at the "tender age" of 30.

In deciding which school he would obtain his undergraduate degree at (Erin said, "It might be nice to live in Maine", to which Lou responded, "Hey look, the University of Maine has a great engineering program") Lou decided on the mechanical engineering program at the University of Maine at Orono (UMO). At UMO, Lou lucked into a great class of really smart and dedicated students, with whom he simulated and empirically verified pine car derby racers as well as designed, built and tested a dogsled to be run in the Alaskan Iditarod. Lou also took many stimulating classes with a variety of excellent professors too numerous to list. One professor in particular, Mick Peterson, took a chance on Lou and had him work on a bio-mechanics research project. Enjoying the experience, Lou applied and was accepted to a summer

internship at Los Alamos National Laboratory (LANL).

Lou's experience at LANL ended up being a turning point in his career. At LANL, he was introduced to a very high level of research (with awesome and expensive ~~toys~~ pieces of equipment) and open ended projects that were incredibly exciting to work on. Lou couldn't believe people got paid to do such work and when he asked how he could obtain such a job, he was informed he needed to get a PhD. That summer when Lou returned to Maine, he proceeded to apply to various PhD programs. Lou knew that he wanted to work in the emerging field of nanotechnology, using nano-scale capabilities to design materials that could make superior energy based devices. After narrowing it down to a few programs, Lou decided to attend Cornell University and work for Emmanuel P. Giannelis in the field of Materials Science and Engineering.

Before arriving at Cornell, Lou accomplished as many stressful things as possible by graduating from UMO, proposing to Erin, planning a wedding in six weeks, and moving to Ithaca to start graduate school—all within 3 months! At Cornell, Lou plunged headfirst into research, helped by the fact that the Giannelis group had many friendly senior grad students and post docs that he could collaborate with, as well as an advisor that encouraged his scientific curiosity. Lou was trained (by the famous TEM-Jedi Master: John Grazul) and became proficient at electron microscopy and this led him to collaborate and contribute to various research projects he would have never had the chance to work on otherwise.

As for his own research, Lou started by working on ionic polymer based actuators (IPMCs) which gave him an ability to work with Nafion® based nanocomposites. Using this accrued knowledge Lou went on to develop electrodes for proton exchange membrane fuel cells and eventually: high surface area porous carbon materials (currently being developed for batteries and super capacitor applications). In

both these projects Lou was able to capitalize on his dream to use nano-scale scientific advances to make superior materials for energy based applications.

Throughout it all, Lou realized he has really lived a charmed life and though he has loved his time at Cornell, he is eager to see what his next scientific adventures will entail. Lou hopes to continue “knocking out science” and keep getting paid for something he would do for free—life is good!

Dedicated to all the folks that helped get me here, but especially to my wife Erin: for always supporting me, encouraging me and for being an inspiration to me.

ACKNOWLEDGMENTS

First and foremost, I would like to express my gratitude to my family. To my parents, Jose Luis and Carmen, for teaching me what type of man I should aspire to be and for instilling a strong work ethic in me through their example. I would also like to acknowledge my two siblings, Tony and Deli who were and still are my best friends in the world. Finally to my wife, Erin, I must thank you for your incredible love, support and the joy you bring to me every day. You are easily the best thing that has ever come into my life and I am so grateful for everything about you, especially the tremendous patience you've shown me while I finished this degree!

To Emmanuel, thank you for accepting me into your group all those years ago, I really feel like I hit the lottery working for you. You gave me so much freedom to explore various scientific rabbit holes, but always intuitively knew when to pull me back out. Thank you for teaching me how to be a proper scientist, but most importantly, for taking the mentorship aspect of your role as advisor as seriously as you did. Thank you for your advice, support, guidance and friendship; I have learned so much from you and I am eternally grateful.

To my committee members, Chris Ober and Francis DiSalvo, thank you for agreeing to be on my committee, despite your busy schedules. Prof. Ober, your questions and comments at my talks were always spot on. Your ability to think and analyze presented work is always something I've admired and tried to emulate. Prof. DiSalvo, your obvious curiosity for science seems unabated despite your considerable experience in the field—you are an inspiration. I hope to continue our talks in the future; I always left your office with an extra bounce in my step and numerous thoughts in my head.

I would also like to acknowledge collaborators to the work presented here in

this dissertation. For the catalyst layer electrode work presented in the JACS manuscript, there were helpful discussions involving Kausik Dana, John Grazul, Semma Ansari and Genggeng Qi; while Scott Gilje provided materials and Deli Wang was able to help with electrochemical characterization. Finally, Emanuel Giannelis, Antonios Kelarakis, Eman Da'as and Qianming Gong all contributed to the work and the manuscript. For the high surface area carbon work, Rubal Dua, from the Peng Wang research group in KAUST came into our group at just the right time as we were starting this project; his expertise and driven nature pushed the work forward and he is an equal contributor. I also would like to thank Dr. Peng Wang and his research group for their hospitality while I was collaborating with them on this project in Saudi Arabia at KAUST. From my research group: Emmanuel Giannelis, Ritu Sahore, Anirudh Ramanujapuram (my *bhai*), Su-Hou Pai, Natasha Hjerrild, Nidhi Bhandari, Panos Dallas and Genggeng Qi all helped with aspects of the work and/or manuscript at some point. I must also acknowledge collaborators from EMC^2 and in particular, PhD candidate Joerg Werner (a fellow carbon-phile from the Wiesner group) for helpful discussions.

To my research group, I cannot thank you enough. I was very lucky in many ways to start in a research group filled with friendly senior grad students (Loan, Jason and Robert) and post doctoral researchers (Hui-chin, Haris, Antonios, Suren and Seema) that were very happy to take a fresh faced "babe-in-the-woods" graduate student under their wings and introduce him to the joy/pain/ardor of research. Since then the flux of students, post docs, visiting scientists and staff that have come through our group has been immense, but the constants that I remember always encountering are great science and amazing people. I think I have had the pleasure of collaborating, to some degree, with just about every member of the Giannelis group that has come through while I was in the group. I also have to point out our *carbon strike force seal*

team six members (Ritu, Ani, Pai, Natasha, Tiff and Turki) for contributing to various parts of my later carbon work and for carrying it on to greater glory after I leave. I also have to acknowledge Qi, an incredibly skillful chemist (and my *shun-di*) who was always willing to help answer questions and help with experimental set ups.

To my fellow PhD students outside of my research group, there are too many awesome people to list, but thank you all for the memories (parties, paintball and skiing come to mind) and good times; particularly Spoerg (an amazing bio-hybrid material with superior festive properties), Nik and Srikant for always being down for good times. A special shout out goes to the class I came into the department with (Michelle, Alwin—*WWAD*, Erin, Debra, Mike, Miki, Hiro, Qi, Xinwei and Trina). You have not only helped me immeasurably with research and surviving the Q exam (in a bonding experience that can best be described in a very Shakespearian—*He who sheds blood with me I shall call my brother*—sort of way), but you have helped me move a ton of stuff (some of you twice!) and provided incredible friendships, thank you. To Mike, thanks for being my coffee buddy, the unlimited coffee cup from College Town Bagels was great, but what I really remember are our awesome "figuring out the whole universe" talks we had on the way there and back. To Jason, Rachel & John, Anna & Brendan, Miki and Daveed; thanks for having massive amounts of people over at your respective houses for various parties and functions. Finally, thanks to the administrative staff of the MSE department as well as the KAUST-CU office. Thank you for all the help you have provided to me. I may be able to handle myself in the lab, but my kryptonite is red tape and paperwork; thank you for all your help in that area and doing it with a smile and in an affable manner! I also wish to acknowledge the folks at the Cornell Center for Materials Research (CCMR); their expertise is only matched by their friendliness. Finally, this work has been aided tremendously by copious amounts of caffeine provided by College Town Bagels and

various podcasts while going through TEM sample preparation (listening to *Radio Lab*, *This American Life* and *The Dan Patrick Show* all kept my passion bucket for science constantly filled to the brim).

My work has been supported by the Alfred P. Sloan Foundation via a Sloan fellowship, the Energy Materials Center at Cornell (Award No. DESC0001086), the King Abdullah University of Science and Technology (Award No. KUS-C1-018-02), the Grassroots GK-12 program (award no. DGE 1045513) and has made use of the Cornell Center for Materials Research Shared Facilities supported through the NSF MRSEC program (DMR-1120296).

TABLE OF CONTENTS

LIST OF FIGURES

LIST OF TABLES

CHAPTER 1

INTRODUCTION

1.1 Organic-Inorganic Nano-hybrid Materials

The term "hybrid" has seen much use lately, particularly when referring to vehicles powered by hybrid power plants. In materials science, hybrid materials refer to the combination of two or more differing materials into one conglomerate material. A further subset are organic-inorganic hybrid materials, where as the name suggests, organic and inorganic materials are combined to form a new composite material. As organic and inorganic materials can have vastly varying properties, the new composite material can be made to take the best of each component material's properties. Examples of such materials (Figure 1.1) include certain automotive tires, fiberglass, nacre and Euplectella sp. (a hexactinellid sponge). All of these composite materials greatly improve upon the parent materials' mechanical properties by using a high strength, low ductility inorganic material with a low strength, high ductility organic material; combining them into a superior composite material with both high strength and high ductility.

When at least one of the hybrid material's constituent parts resides in the nano-length regime (< 100 nm), these materials can be classified as nano-hybrid materials. This is an important distinction, because at nanometer length scales certain size effects can become prevalent [1, 2]. Since Nobel Laureate Richard Feynman's famous and visionary talk, "There is plenty of room at the bottom", he gave December 29th, 1959

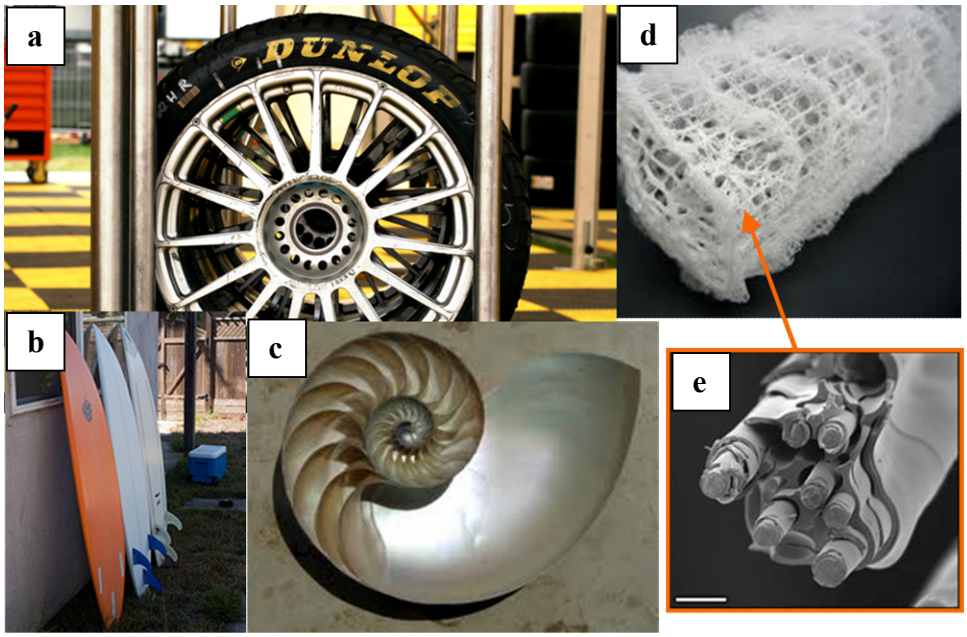

Figure 1.1: Images of a) certain silica-rubber composite tires and b) fiberglass composites as commercial products. Photos of naturally occurring composite materials c) nacre and d) sea sponge with an SEM image e) of one of the sea sponge single beams revealing its ceramic fiber-composite structure (scale bar, 20 μm). Images a)-d) reproduced with permission under the Creative Commons Attribution-Share Alike 3.0 Unported license, image e) reproduced with permission from Aizenberg et al. (2005) [90].

at the annual meeting of the American Physical Society [3], the field of nanotechnology has exploded. The synthesis of nano sized (<100 nm) materials, called nanomaterials, has since become standard practice. This ease of synthesis has enabled scientists to easily fabricate nanomaterials with unique (and often times superior) photonic [4, 5], electronic [6, 7], mechanical [8-10] and catalytic [11] properties when compared to larger macro-sized materials. Furthermore, the miniaturization of inorganic materials has allowed these nanomaterials to be on the same length scale (or smaller) of organic materials such as proteins, DNA and polymers leading to the facile integration of the two systems into nano-hybrids.

In these nano-hybrid systems, the inorganic nanomaterial can often be used to imbue its inherent properties into an organic system. Examples of these systems include nanoparticles (NPs) introduced to biomolecules for their plasmonic properties [12, 13], electrical conductivity [14], and magnetic properties [15]. Additionally, the combination of organic/inorganic distinct systems has even been shown to develop new classes of nano hybrid materials [16-18]. These nano-hybrid systems can take advantage of the inorganic materials' inherent properties to introduce new functionalities, as well as tune the properties of the system as a whole through the synergistic interaction of the two different components.

The enhanced and novel properties possible in nano-hybrid materials makes them very promising for solving various materials based problems central to a multitude of applications. As we continue to make the synthesis of these materials facile and cost effective, we can expect to find more and more of these nano-hybrid systems in our every day products and devices. These nano-hybrid materials should be thought of less as a combination of two different materials, but rather a new class of materials unto themselves.

1.2 Nanocomposites

Similar to nano-hybrids, a special class of materials exists that use an organic polymer matrix with nanoparticle fillers to take advantage of these nano size effects. These materials are called nanocomposites. When the filler material is an inorganic material,

nanocomposites can also be a subset of nano hybrid materials. Nanocomposite materials have come very far since gaining prominence for enhancing a polymer's properties by adding nanoparticle fillers to the polymer matrix [19-22]. As shown in Figure 1.2, the fillers can be fit into one of three categories: 1) nanoparticles – where the filler's three dimensions are on the order of nanometers, can be called nanogranules or nanocrystals (colloidal silica for example), 2) nanotubes – where two dimensions are on the order of nanometers, can be called nanorods or whiskers (examples are carbon nanotubes and cellulose whiskers) or 3) nanolayers – where only one dimension is restricted to the nanometer length scale, usually referred to as nanoplatelets (examples are nanoclays and graphene sheets).

Nanocomposites differ from their macro sized traditional composite materials in that a very small amount of the filler is needed to improve upon (or add novel) properties to the polymer matrix; typically less than 10 % by weight [24]. This minute addition of filler results in little extra weight being added for the improved properties bestowed. Furthermore, since the nanocomposite is mostly made up of the original polymer matrix, the nanocomposite can easily take advantage of common polymer commercial techniques. Finally, advances in nanocomposite synthesis such as melt processing [25], have further reduced scalability barriers so that certain nanocomposites have seen commercial product adoption. One of the better examples of the commercialization of this technology has been the Toyota Motor Corporation, which not only initiated the groundbreaking work on clay based nanocomposites [26], but has developed nanocomposite products for use in their vehicles such as timing belt and engine covers. Other products include beverage containers that take advantage

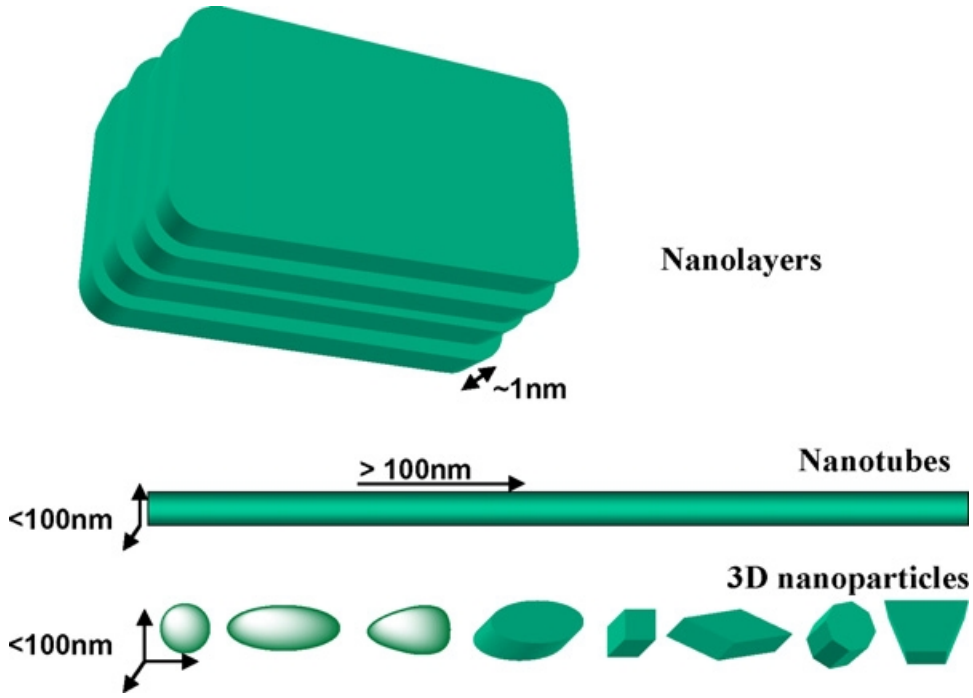

Figure 1.2: Images showing the three different classifications for nano-fillers, reproduced with permission from Kumar et al. (2009) [23].

of the superior barrier properties of nanocomposites to mitigate the permeability of oxygen when compared to the neat polymer material.

Even with some commercial success in nanocomposites, they remain a vibrant research field. As new advances in nanotechnology result in novel nanomaterials and/or make the synthesis of previous nanomaterials easier or more cost effective, new classes of nanocomposites can be realized. The continuous advent of newer nanomaterials can ensure that the field of nanocomposites will continue to grow and flourish.

1.3 Carbon Filler Based Nanocomposites

Carbon based nano-fillers have attracted a great deal of attention due to the relatively high intrinsic electrical conductivity and mechanical strength of the filler when compared to that of the typical polymer matrix. All three categories of fillers (Figure 1.3) have been explored for carbon including carbon black as nanoparticles [27], carbon nanotubes (CNTs) as of course, nanotubes [28] and graphene sheets as nanolayers [29]. Of the three, carbon nanoparticles have seen the most use as they are now ubiquitous in research and have been commercialized in reinforcement for automotive tire applications. CNTs have seen an explosion of research since the seminal work by Sumio Iijima in discovering CNTs [30] in 1991. Since CNTs are theoretically sheets of hexagonally bonded carbon atoms (with sp^2 orbitals) that can be envisioned as rolled into tubes, CNTs can have incredibly high mechanical strength and electrical conductivity. These CNT characteristics have led to the extensive exploration of many nanocomposites based on both of these properties in the literature [31, 32].

As with CNTs, graphene sheets have more recently undergone a similar explosion in research, especially after the Nobel Prize in Physics was awarded to Novoselov and Geim in 2010, for their “groundbreaking experiments regarding the two-dimensional material graphene”. Though the Nobel Prize was awarded in 2010, intensive research in graphene has been ongoing since the pair’s seminal publication in 2004 [33]. The

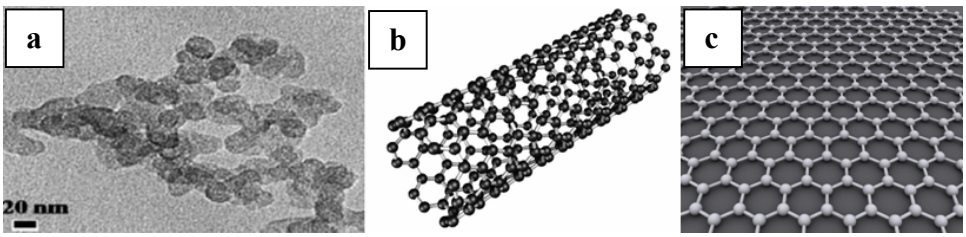

Figure 1.3: Images showing a) carbon black nanoparticles, b) a carbon nanotube and c) a sheet of one atom thick graphene. Image a) reproduced with permission from Guo et al. (2010) [91] and images b) and c) reproduced with permission under the Creative Commons Attribution-Share Alike 3.0 Unported license.

seductive properties of a sheet of graphene are apparent: ballistic electrical conductivity [34], high mechanical properties [35] and the fact that a graphene sheet (GS) is one atom thick means that the theoretical surface area of a GS is 2630 m^2/g [36]; roughly an American football field of area in 2 grams of material. This high specific surface area becomes an important parameter when using GS as filler in a polymer nanocomposite system. This is due to the fact that the low filler amount needed for high desired properties in the nanocomposite is directly attributable to the filler's high surface area to volume ratio [37]. This high ratio allows a low nanofiller amount needed before the filler forms a continuous percolated network throughout the polymer matrix. Taking advantage of the high specific surface area of GS, recent literature [38] has shown that a T_g shift of 30 °C is achievable at a loading of merely 0.05 wt % for a graphene nanocomposite. This shift in T_g at such low loading, indicates that a percolated network can be achieved with minimal GS present. These low loadings have made optical transparency possible while also simplifying processes.

One of the major hurdles that has proven challenging and has prevented the widespread use of GS based nanocomposites, has been processing the parent material (graphite) into graphene. Graphite is the stacking of several layers of graphene (≥ 10 layers). Technically graphene is solely one atomic layer thick, but in reality, the majority of graphene utilized in the literature is a few (1-4+) layers thick. Separating graphene to even a few layers thick has only been recently achieved, as previous exfoliation methods have only managed to produce graphite materials of about 100 nm in thickness [39, 40]. Recent work [41] has shown that by employing a modified method for oxidizing graphite [42], the resultant graphite oxide (GO) can be more easily dispersed within an aqueous suspension. The method (Figure 1.4) involves chemical oxidation to introduce carboxylic, hydroxyl and other oxygen containing groups that disrupt the π-π interactions present in the graphite. This, combined with the hydrophilicy introduced by the oxygen groups makes it easy to disperse the GO sheets in water under sonication. Once suspended in water, the GO can be easily processed with various organic materials into GO-polymer systems. A simple post reduction step converts the GO into reduced graphite oxide (rGO) sheets. It is important to note that the rGO sheets may have defects from the oxidation and sonication, but enough C=C bonds will be created via reduction, to ensure many electron conducting pathways are present in the resultant material. Thus the rGO material will not be perfect GS, but the tradeoff in dispersion more than makes up for the minor loss from the properties of pristine GS. This two step procedure for producing well dispersed GS (or rGO) provides a valuable tool that enables the promise of GS-polymer nanocomposites to be realized [43, 44].

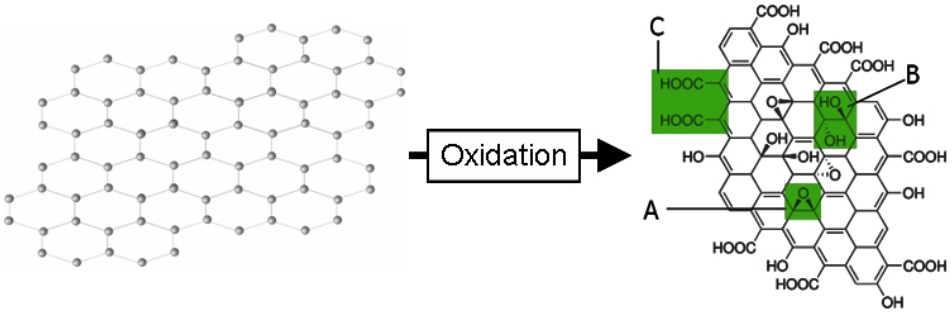

Figure 1.4: Image demonstrating a sheet of graphene being reduced into a sheet of graphite oxide, with the various proposed oxygen groups shown. Images reproduced with permission under the Creative Commons Attribution-Share Alike 3.0 Unported license.

1.4 Porosity Within Nano-hybrid Systems

Due to all of the advances made within nano-hybrid systems, the ability to attain superior materials for specific applications has been enhanced. The potential applications that can benefit by applying the technology of these nano-hybrid systems to porous materials broaden to include materials for absorption [45], catalysis [46], drug delivery [47, 48], fuel cell electrodes [49] and chemical sensor components [50]. Thus the ability to tune a nano-hybrid material's properties through its constituent components now provides a lever of control in porous materials. The porous material's properties can be tailored depending on the requirements of the application. This tunable functionality of the nano-hybrids, combined with the structural tunability (by using various pore forming synthesis techniques) has the potential to result in devices with superior performances across many disciplines.

Porous materials have been divided into three size regimes in accordance with

standards set by the International Union of Pure and Applied Chemistry (© 1994 IUPAC). Microporous, mesoporous and macroporous materials are deemed to be materials with pore widths of 0-2 nm, 2-50 nm and 50 nm and above, respectively [51]. IUPAC also describes density in three ways: 1) true density – the density of the material *excluding* pores and interparticle voids 2) apparent density – the density of the material *including* closed and inaccessible pores and 3) bulk density – the density of the material *including* pores and interparticle voids. The porosity in the porous material is merely the volume of void space with regard to the total volume, usually given as a percentage. Specific surface area (SSA) is an important property within porous materials and is usually measured on a per mass basis as m^2/g. Finally, pore volume, which is simply the amount of porosity or void space within the porous material on a per mass basis, is usually measured in cm^3/g.

Porous materials have certain structural properties that when compared to their bulk counterparts lend themselves to certain applications. For example, at larger length scales, macroporous systems have been employed for tissue growth, cell supports, separation technologies, and biocatalysts [52-53]. As the porosity length scale enters the mesoporous domain, the smaller pore sizes result in higher specific surface areas that can be as high as several hundreds or even 1000+ of m^2/g [54]. At these higher SSAs other applications such as catalyst supports [55] and absorption technologies [56] become prevalent. Furthermore, the mesopore sizes of these materials open up other separation applications previously unavailable such as the selection of noble metal and semiconductor by size, which is important for the high throughput commercialization of such nanoparticles [57]. Recently there has also been an

explosion of research based on using mesoporous conducting materials in electrochemical applications such as battery electrodes [58, 59]. At microporous length scales, the specific surface areas of these materials can reach 2000+ m^2/g [60, 61]. At these high SSAs applications such as electrodes for electrical double-layer capacitors (EDLCs) have the potential for very high performance as the specific capacitance theoretically scales up with SSA [62]. By introducing nano hybrid materials into either processing steps or the final material, the capacity to synthesize and/or optimize these materials can be dramatically improved.

1.5 Macroporous Materials

Current synthesis of macroporous materials has typically followed techniques that have been used for many decades for various systems. Macroporous ceramics, having been developed in the 1960s-1970s [63], have a diverse synthesis history with three basic techniques employed (Figure 1.5). These are facile, proven techniques with a track record of commercial success. These procedures are also important in that some modified aspect of the techniques usually make their way into the synthesis of porous materials for the other length scales. The first technique is the replica method and it is simply the process of replicating the porous structure of another material. In the case of ceramics, it is typically done by finding a macroporous polymeric sponge-like material that is then coated with a ceramic suspension until the internal pores are filled with the ceramic material. Rollers are then employed to remove the excess ceramic suspension, while leaving a thin ceramic coating over the polymeric sponge.

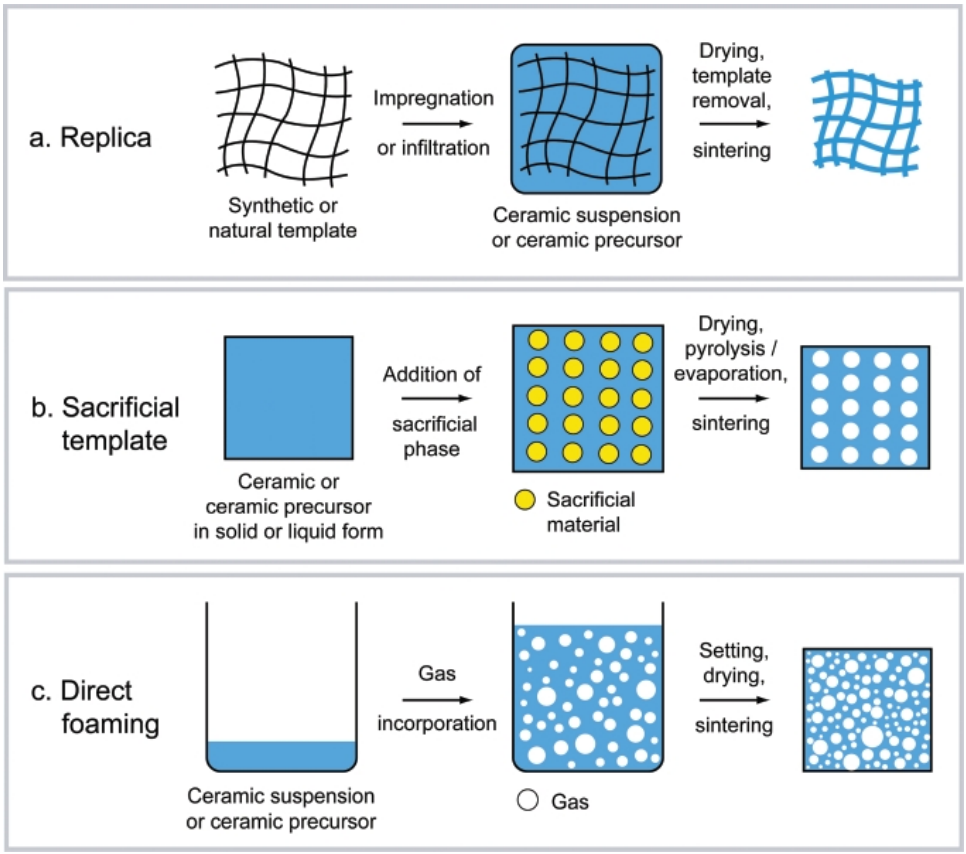

Figure 1.5: The three techniques typically employed for synthesizing macroporous materials, reproduced with permission from Studart et al. (2006) [63].

The material is then heated to remove the polymer sponge and finally sintered to complete the macroporous ceramic scaffold. The second method involves a removable material, but in this case the sacrificial template is what forms the pores. In this method, the template and the ceramic materials form a biphasic composite that is then treated in some manner to remove the template, leaving behind macropores in the ceramic material. This hard templating method is also common in the synthesis of mesoporous materials (vide infra). In the final method, direct foaming, the porous materials are produced by the incorporation of air into the suspension, which is then subsequently set to keep the macroporous structure formed by the air bubbles.

1.6 Ice Templating as a Macroporous Synthesis Route

One macroporous synthesis technique that has gained prominence recently is ice templating [50, 64-70]. Though the procedure of using ice crystals to induce porosity has been around since the 1940's [71, 72], the recent interest given to this method by researchers has pushed the technique in new directions, particularly when it is combined with the newer nanomaterials and current techniques. In ice templating, a suspension or solution is introduced to a colder temperature gradient. In an example of colloidal ceramic nanomaterials in an aqueous suspension (Figure 1.6), the cold temperature crystallizes the water introducing an ice front that moves along the suspension. As the crystals are formed, they expel the colloidal particles from the solidifying water. After the material is frozen, the two distinct phases are structured, whereby the ice is the sacrificial template. Subsequently, it is simply a matter of using freeze-drying (high vacuum sublimation of ice) to remove the ice without affecting the structured phase. Further work [65, 67, 69], has delved deeper into the ice formation mechanism and has revealed parameters that can control the ice solidification, giving researchers controls to better direct the final structure.

Of late, researchers have started to combine the attractive properties control of nano-hybrids with the facile synthesis of ice templating to produce porous materials scaffolds with imbued functionalities [50, 66-68]. Deville et al. in particular were able to recreate one of nature's materials science feats, by synthesizing a novel material not

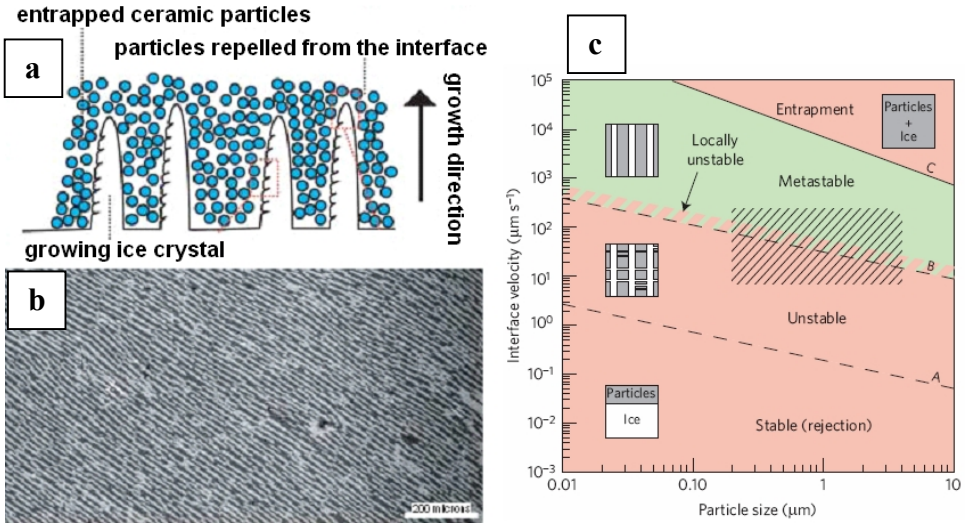

Figure 1.6: Images showing a) an ice front moving through a suspension, expelling the particles away as the solvent solidifies and b) the resultant templated structure is revealed after the sublimation of the frozen solvent, images a) and b) reproduced by permission by Deville et al. (2006) [67]. The graph represented by c) shows how the structuring can be controlled by the interface velocity and particle size, reproduced with permission from Deville et al. (2009) [65].

unlike nacre [67]. Nacre has consistently been recognized as a material found in nature that bears inspection. The naturally occurring hybrid material is made up of a platy inorganic phase (calcium carbonate) along with an organic phase (protein) to create a material with excellent toughness characteristics. By using ice templating, the researchers were able to compose their own hybrid material and use it as a guide to synthesize porous scaffolds for osseous tissue regeneration with strengths up to four times higher than those of current materials used for implantation.

Gutierrez et al. used a nano-hybrid system and employed ice templating for electrochemical applications [49]. The researchers used multiwall carbon nanotubes (MWCNTs), that had their surfaces decorated with platinum nanoparticles and

combined the nanomaterials with chitosan (CHI) via ice templating. The resultant material (Figure 1.7) was successfully utilized as an anode in a direct methanol fuel cell. Gutierrez and colleagues were able to tune the electrical conductivity of the nano-hybrid porous system by modifying the MWCNT content. This was an excellent demonstration of what was possible when combining the functionality of nano-hybrid systems with the ease and flexibility of ice templating to manufacture a material with specific properties for a specific application.

1.7 Microporous Materials

In the world of microporous materials, zeolites and activated carbons dominate the research landscape. Both are at the point of active commercialization, but are still undergoing research. Zeolites are highly crystalline aluminosilicate materials that have porosity in the micropore regime. They have been used extensively in ion exchange, absorption, separation and catalysis research [73, 74]. Zeolites have also been used as a sacrificial template for microporous carbon synthesis [75]. Activated carbon materials are also widely available commercially and have been used in research as well. The process for synthesizing activated carbons can be classified as chemical or physical and involves the carbonization of a carbon precursor/feedstock (typically lingnocellulostic materials) along with an activation process that induces microporosity. Chemical activation involves the co-carbonization of a parent feedstock with a chemical. Three specific chemicals have seen the most extensive use and include potassium hydroxide/carbonate, phosphoric acid and zinc chloride. For physical (also called thermal) activation, the process is quite different. The carbon has

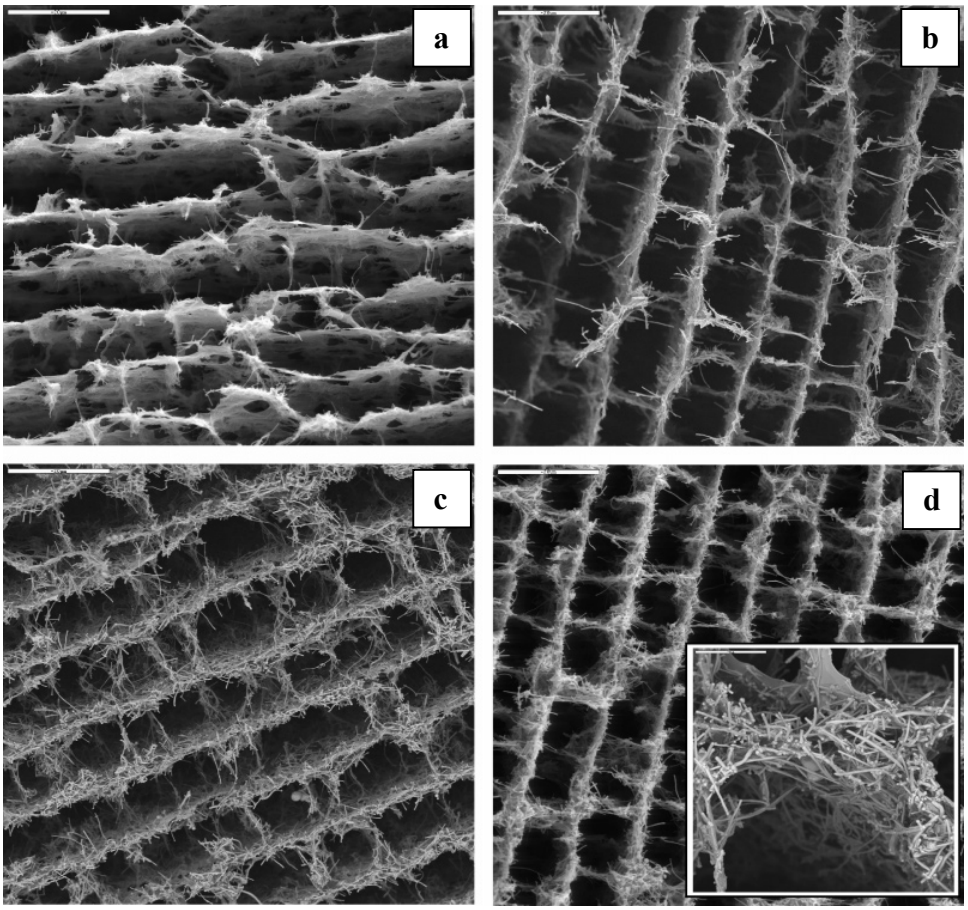

Figure 1.7: Ice templating SEM micrographs of cross-sectioned monolithic MWCNT/CHI 3D architectures with different MWCNT contents: (a) 66 wt %, (b) 80 wt%, (c) 85 wt%, and (d) 89 wt% (bars are 20 μm). The inset shows interconnected MWCNTs forming the walls of the structure (bar is 5 μm) reproduced with permission from Gutierrez et al. (2007) [49].

already been synthesized and one of two gasifying agents, either carbon dioxide or water vapor slowly "extract" carbon atoms from the structure of the porous carbon [76]. The mechanism for physical activation via carbon dioxide is important to aspects of this work and will be examined more thoroughly in Chapter 4.

1.8 Mesoporous Materials

Mesoporous materials can generally be divided into two specific synthesis techniques obtained by hard templating and soft templating. In soft templating, self assembly through the interaction of “soft” materials such as polymers and surfactants results in the formation of mesopores. Groundbreaking work by Kresge et al. in 1992 involved ordered surfactant micelles that would template the precursor material into mesoporous silica. The material was named MCM-41 [77]. A few years later, other seminal papers were published by Zhao et al. and Templin et al. that used block copolymers to direct the assembly of mesoporous silica materials [78, 79]. These seminal works set the foundation for the research that was to follow in synthesizing soft templated mesoporous materials.

Recently, there has been an interest in mesoporous carbon materials [74]. Unlike their silica counterparts, mesoporous carbon materials have good inherent electrical conductivity that enables them to expand their potential applications to include materials for electrochemical converters. As such, efforts have been made to template mesoporous carbon materials from soft templating methods as well. Recent work by Meng et al. [80] has demonstrated a new family of mesoporous carbon materials synthesized via triblock copolymer based self assembly. The synthesis technique (Figure 1.8) was able to produce three different mesoporous structures and could produce either mesoporous polymer or carbon materials.

Hard templating differs from soft templating in that there is a removable sacrificial template much as was shown previously when discussing macroporous materials. What is interesting from a synergistic point of view is that many of the mesoporous

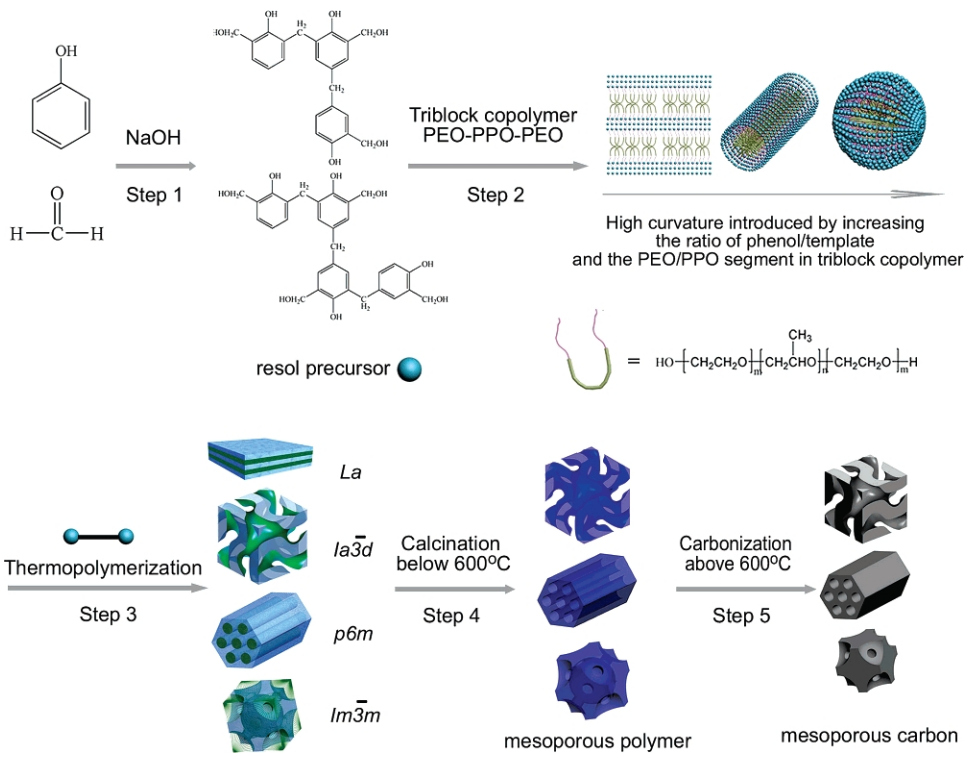

Figure 1.8: Scheme for the preparations of the ordered mesoporous polymer resins and carbon frameworks, reproduced with permission from Meng et al. (2006) [80].

systems that have been developed can be used as a hard template. This can conceptually work with mesoporous carbon templates as well, since carbon materials can easily be oxidized (and removed) at temperatures above roughly 200 ºC, but hard templating has mostly been accomplished through mesoporous silica templates. The silica template can be easily removed after templating by etching via hydrofluoric acid or sodium hydroxide. The preponderance of silica templates can at least partially be attributed to the earlier development of silica mesoporous materials, but whatever the reason, it has resulted in new sets of mesoporous carbon materials based on established mesoporous silica materials such as MCM-48 (related to the MCM-41 materials) and SBA-15. Using MCM-48 and SBA-15 as hard templates, mesoporous

carbons, CMK-1 and CMK-5, were synthesized, respectively [81, 82]. Silica nanoparticles have also been used as a hard template. Hyeon's group pioneered the technique (Figure 1.9) and synthesized mesoporous carbons from various silica nanoparticles [83, 84]. The technique is quite facile and the commercialization of colloidal silica nanoparticles of varying sizes gives the technique a good deal of flexibility. One important note was that in order to ensure tight mesoporous size control a surfactant had to be utilized. This was due to the silica changing from hydrophilic to hydrophobic during carbonization. The resultant change led to phase separation between the silica and the carbon precursor and thus aggregation of the silica particles—necessitating the use of the surfactant.

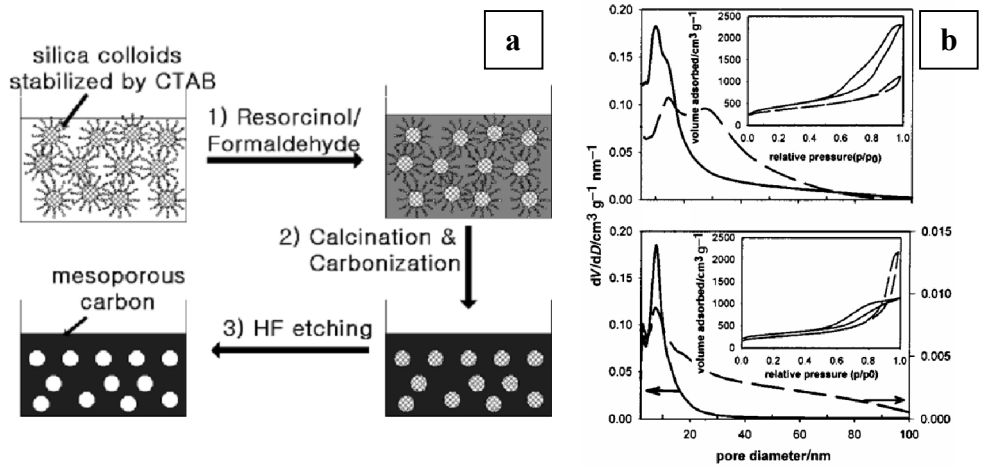

Figure 1.9: a) Scheme showing Synthetic strategy for uniform mesoporous carbons. 1) gelation of resorcinol and formaldehyde (RF) in the presence of CTAB-stabilized silica particles; 2) carbonization of RF gel–silica composite at 850 °C to obtain carbon–silica composite; HF etching of silica templates to obtain mesoporous carbons. b) Graphs of the pore size distributions calculated from the adsorption branch of the nitrogen isotherm by the BJH method and the corresponding N2 adsorption and desorption isotherms (insets) of mesoporous carbons. (top) (—) carbon prepared with CTAB-stabilized Ludox HS-40 silica sols as template and (---) carbon prepared with Ludox HS-40 silica sol aggregates as template. (Bottom) (—) carbon prepared with CTAB-stabilized Ludox SM-30 silica sols as template and (---) carbon prepared with Ludox SM-30 silica sol aggregates as template. Reproduced with permission from Hyeon et al. (1999) [83].

CHAPTER 2

NAFION/GS/Pt POROUS NAN0-HYBRID SYSTEM FOR PEMFC CATALYST LAYER: SYNTHESIS

2.1 Introduction

Proton exchange membrane (PEM), also called polymer electrolyte membrane, fuel cells have been in use since the Gemini space flights in the 1960's. The minimal amount of moving parts, acceptable operating temperatures (~80 °C) and high power densities make them attractive electrochemical converters in niche applications and some conventional applications.

Many of the limitations in PEM fuel cells have historically come from the fact that they employ a platinum catalyst which enables the oxidation of hydrogen and the reduction of oxygen. This use of platinum increases the expense and thus, has decreased the potential for commercialization. It is no surprise then, that much of the research on PEM fuel cells has concentrated on reducing the need for a platinum catalyst or reducing the amount of platinum needed for good performance [85, 86]. Since the 1980's there has been a considerable level of success in lowering the platinum content from about 4-10 mg/cm^2 to about 0.4 mg/cm^2 (though current research has lowered the platinum content even more), by the advent of ionomer (typically Nafion®) impregnated gas diffusion electrodes, extending the three dimensional reaction zone [87-89]. To see the full implications of this tremendous leap

in platinum efficiency one must have a good conceptual understanding of how a typical PEM fuel cell is organized.

2.1.1 PEM Fuel Cell Set Up and Mechanism

A typical PEM fuel cell consists of a physically symmetrical device where a proton exchange membrane separates each half of the cell (Figure 2.1). From an electrochemical perspective, hydrogen is fed through the anode's gas channel. The hydrogen flows through the gas diffusion layer (a 100-300 μm thick, electrically conductive macroporous network, usually a carbon cloth) and reaches the catalyst layer. The catalyst layer has been developed over many years and is typically a 5-20 μm thick composite material of carbon black nanoparticles, smaller platinum nanoparticles and Nafion®. At the catalyst layer there is the need for a material that has many different properties—a classic materials science problem. The catalyst layer (from the anode's perspective) must provide a material permeable to the flow of hydrogen gas that must reach the platinum nanoparticles that catalyze the H_2 into protons and electrons through oxidation. The catalyst layer is directly in contact with the PEM, which must have good ionic conductivity, while being an insulator to electrons. Thus the protons go through the PEM but the electrons cannot and thus go through the electrically conductive carbon network, through the GDL and pass out through the external circuit. Meanwhile, on the cathode side, the protons emerge from the PEM into the cathode's catalyst layer and reach the catalyst, whereby the electrons from the external circuit make their way through the GDL to the catalyst, joining the protons and combining with oxygen that has flowed from the cathode gas channel;

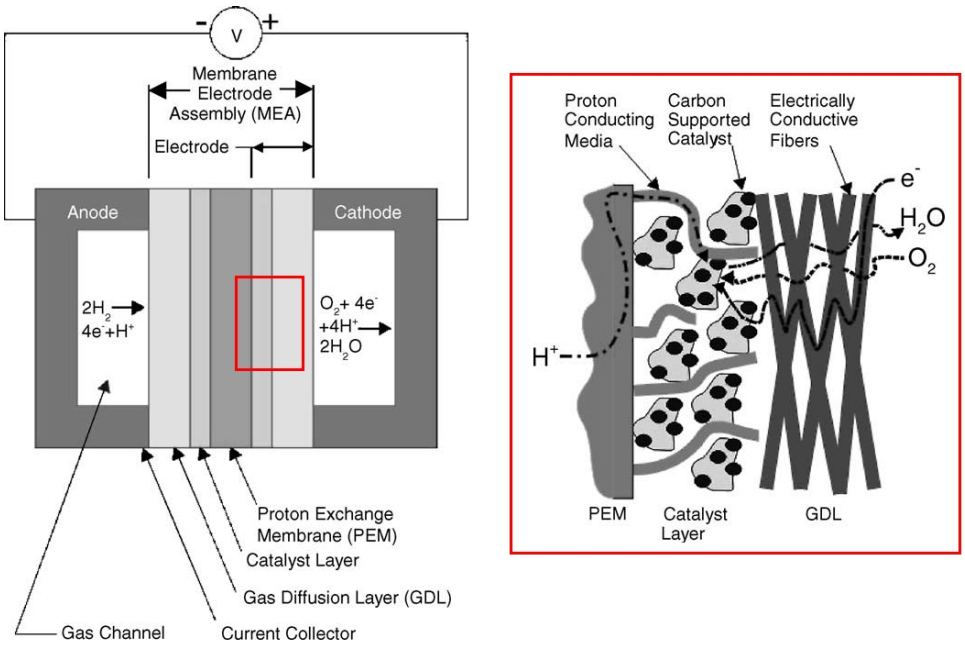

Figure 2.1: a) Schematic of a single typical proton exchange membrane fuel cell. Red boxed area is shown in: b) transport of gases, protons, and electrons in a PEM fuel cell electrode on the cathode side. Reproduced with permission from Litster et al. (2003) [92].

resulting in reduction. The half reactions are described as: $2H_2 \rightarrow 4e^- + 4H^+$ (anode) and $O_2 + 4e^- + 4H^+ \rightarrow 2H_2O$ (cathode), with the full reaction being: $2H_2 + O_2 \rightarrow 2H_2O$.

2.1.2 PEM Fuel Cell Catalyst Layer

The catalyst layer is where all the electrochemical reactions take place and thus has been the source of a large amount of the research in PEM fuel cells. In the catalyst layer there is the necessity for a material that can have many different properties all at once. The catalyst layer must be electrically conductive to allow for the quick removal/addition of electrons to the catalyst (platinum nanoparticles), while at the

same time, have high ionic conductivity to allow for the same movement of the cations (protons). While meeting these prerequisites, the material must also allow for the flow of gases, indicating that some level of porosity is needed. Finally the catalyst layer, as its name implies, must provide a scaffold to hold the catalytic nanoparticles. In a catalyst layer, it is of significant importance to give rise to an extensive amount of triple phase boundary (TPB) conditions, which are the contact points in a membrane electrode assembly between the gas reactants (flowing through the pores), the ionic conductor and the catalyst adsorbed to an electronically conductive support. Thus, as previously explained, by extending the ionomer into the catalyst layer the TPB zone becomes a *three dimensional* catalyst layer and the catalyst layer (and therefore the expensive catalyst) is utilized more efficiently. The purpose of this project was to develop a novel synthesis approach that could greatly enhance these TPB conditions within the catalyst layer (vide infra). By using a novel nano-hybrid porous system, the potential for a superior catalyst layer could be realized.

2.2 Previous Work Synthesizing a PEM Fuel Cell Catalyst Layer

Since 1993, when Wilson patented the technique [93], a significant number of catalyst layers have been fabricated using what was called a “thin-film” method. Here a slurry is made consisting of a 5 wt% solubilized ionomer (typically Nafion®) with 20 wt% platinum/carbon support, at a ratio of 1:3 of Nafion®:catalyst. Water and glycerol are added at ratios of 1:5:20 for carbon:water:glycerol. The resultant slurry is then sonicated until it is homogeneously dispersed and at the correct viscosity. The Nafion® PEM is then treated with NaOH to ion-exchange the PEM into the Na^+ form,

then rinsed and dried. The slurry is then applied directly to the PEM and dried in vacuum at 160 °C. The same process is repeated for the other side of the PEM and dried as well. Then the material is boiled in sulfuric acid (0.1 M) to put the Nafion into its acid form (protonated) and the material is rinsed with water. Finally carbon cloth is added to each side (for the GDL) and the membrane electrode assembly (MEA) is placed in between the two gas channel electrodes to complete the cell. Thus in this technique an "ink" is made that can be spread onto each side of the PEM, which becomes the catalyst layer. By using Nafion® in the ink, the catalyst layer is ensured good adhesion with the PEM and good ionic conductivity to and from the PEM. This method has been used in industry, though the ratios of each component in the slurry have typically been empirically optimized and are usually guarded trade secrets. Thus, the material that makes up the catalyst layer is not really a traditional composite material. It is better described as more of a combination of various components brought together to encourage the presence of multiple TPBs.

Previous work by Qi et al. [94] in 1998 was a novel step for the design of a MEA catalyst layer in several ways. One way, was in the synthesis of a true composite material. As Figure 2.2 shows, the researchers were correct to point out that the state of the art thin-film techniques of the time, had three different material components coming together physically to do three different tasks. In this work, two different polymers were made into a composite that had both good electronic and ionic conductivities. By using a composite of polypyrrole/polystyrenesulphonate (PPY/PPS), both electron and ion transport could occur within the same material, eliminating the need for carbon. Then it was simply a matter of depositing the Pt on

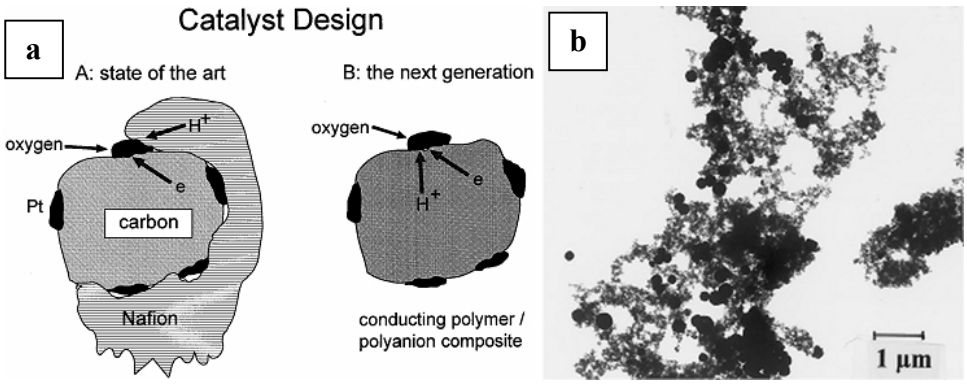

Figure 2.2: a) Schematic diagrams of the 'state of the art' PEM fuel cell catalyst layer structure and the new design used by Qi et al. b) Transmission electron micrograph of the PPY/PSS/Pt. composite. Reproduced with permission from Qi et al. (1998) [94].

the composite polymer by hydrogen reduction of K_2PtCl_4. The structure also had porosity that enabled it to be used as a catalyst layer in a PEM fuel cell, where currents of 0.1 A/cm were observed for oxygen reduction. This work was not only important in using composite materials to do the prerequisite tasks more effectively, but it was novel in that the material was predominately a polymer system. Most catalyst layers, then and currently, can be thought of as dominated by the carbon nanoparticles and thus having properties more closely resembling an inorganic material.

Another composite system that bears mentioning is also a nano-hybrid system. The work was done by Gutierrez et al. [49] and has, in part, been covered in section 1.6. By synthesizing a nano-hybrid system and using ice templating, this group was able to fabricate a good functioning anode for a direct methanol fuel cell (DMFC). This particular system added Pt decorated MWCNTs to an aqueous suspension (0.05 M acetic acid) of chitosan (CHI). The CHI acts to help disperse the MWCNTs in water, something that can be difficult to accomplish. The CHI also has ionic conductivity, of

up to 10^{-4} S/cm [95] which helps in its function as a catalyst layer. It was found that electrical conductivities could be as high as 2.5 S/cm, but only at extremely high loading of 89 wt% MWCNT (of the whole Pt/MWCNT/CHI system).

2.3 Previous Work Synthesizing Ionic/Electronic Conducting Polymers

In attempting to develop a synthesis route towards fabricating a novel catalyst layer, we were able to incorporate previous research led by Dr. Semma Ansari in our research group [100]. In this work, Nafion®/Graphite nanocomposite materials were synthesized that displayed a well dispersed graphene sheet (GS) network within the Nafion® polymer matrix. Thus we were able to synthesize a nanocomposite material that had ionic conductivity from the Nafion® matrix and electronic conductivity from the interconnected GS network, two of the prerequisites needed to have a material with TPBs.

2.3.1 GS-Nafion® 2-step Synthesis Approach for Superior Nanocomposites

As has been previously covered in section 1.3, atom thick sheets of graphene are one of the most promising materials in science today. The incredible strength and electrical conductivity (among other excellent properties) of graphene is already well documented within the literature [96]. One of the biggest challenges of graphene is that it is typically found as graphite, and is difficult to disperse in water systems. One promising route to address this issue is to oxidize the graphite, into GO and to use the GO as a precursor for synthesizing graphite nanocomposites [97]. A drawback to this

approach can be the inaccessibility of the GO to the reducing agents. Here in lies the advantage of using a polymer matrix such as Nafion® [98].

It is important to understand the properties and characteristics of Nafion® first before explaining the GS-Nafion 2-step synthesis approach. Nafion® (Figure 2.3) is a useful polymer made by the copolymerization of a perfluorinated vinyl ether comonomer with tetrafluoroethylene (Teflon®). From Figure 2.3, it can be seen that an easy way to think of Nafion® is as a Teflon® backbone that is hydrophobic, attached to sulfonate (SO_3) side chains that are hydrophilic. Thus, in a way, Nafion® is an amphiphile that can have surfactant-like properties. Though the structure of Nafion® is not yet completely understood, it is believed that almost all of its interesting properties come from its ability to be highly permeable to water [98]. Research has shown that Nafion®'s SO_3 groups organize into ionic domains. This enables nano-channels to form that allow for the easy ingress/egress of water. These nano-channels allow cations (carried by the water) to "hop" from SO_3 group to SO_3 group and give Nafion® its very high ionic conductivity [98]. Since the polymer uses water as part of its mechanism for ionic conductivity, the conductivity can vary depending on the amount of water present, ~0.1 S/cm, for a fully hydrated system [99].

2.3.2 GS-Nafion® 2-step Synthesis – Experimental Procedure and Results

Though true aqueous solutions of Nafion can be difficult to produce, water based suspension are available commercially. Thus our technique [100] involved using a

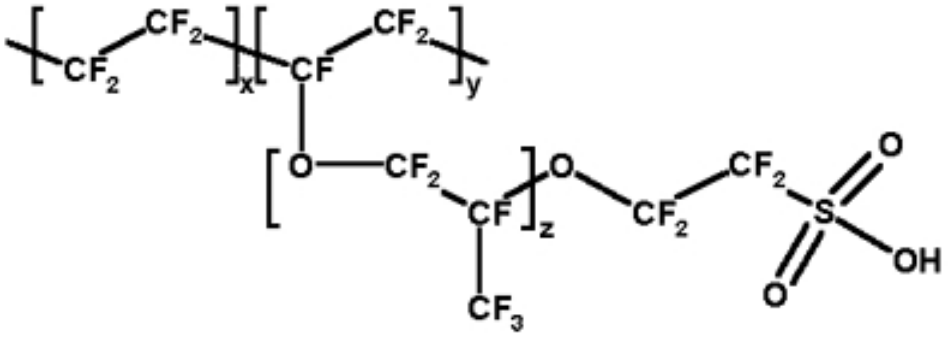

Figure 2.3: Image showing the chemical structure of Nafion. Images reproduced with permission under the Creative Commons Attribution-Share Alike 3.0 Unported license.

two-step approach to fabricate highly dispersed GS sheets within a Nafion® polymer matrix. First, a suspension of GO was combined with the Nafion® suspension. The nanocomposite was then cast, so that the well dispersed GO nanofiller was locked into place by the solid polymer matrix. The GO platelets are then chemically reduced in situ by taking advantage of the nano-channels present in the Nafion® to move hydrazine throughout the nanocomposite. This chemically reduced the well dispersed GO sheets into well dispersed graphene sheets in the nanocomposite. The technique was abbreviated to GS-Nafion 2-step. For comparison, a nanocomposite of functionalized graphene sheets directly introduced into the Nafion® suspension was cast and identified as GS-Nafion 1-step as well as fabricating GO-Nafion nanocomposites that were left unreduced and Nafion (neat) polymer materials. The GO and GS fillers were all loaded at a concentration of 5 wt%.

The TEM characterization results (Figure 2.4) indicated a clear difference in the 2-step procedure versus the 1-step. The 2-step procedure clearly resulted in much better dispersion of filler, though remarkably, the graphite showed better than expected

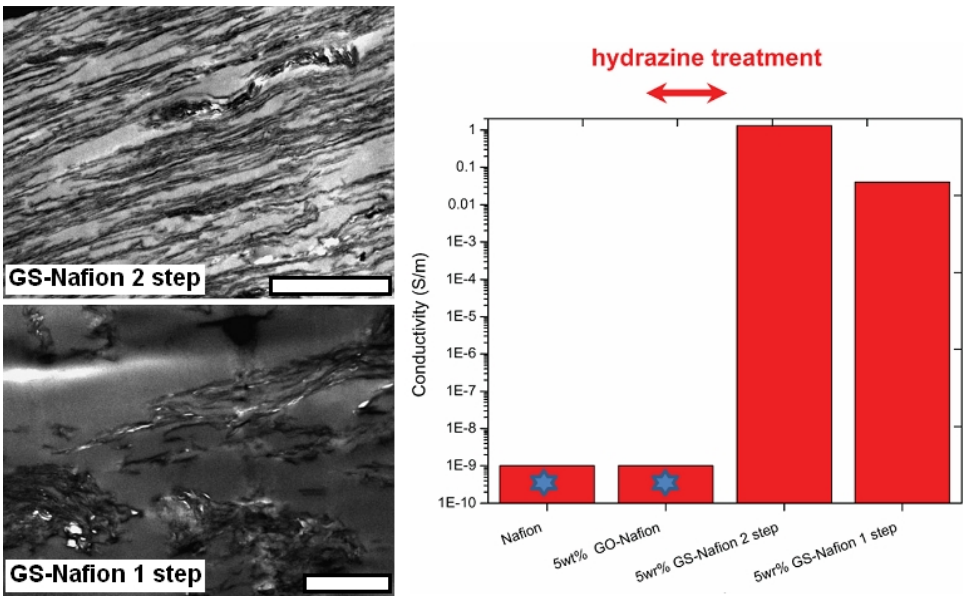

Figure 2.4: Left side is TEM images of (top) GS-Nafion nanocomposite via 2-step techniques and (bottom) GS-Nafion nanocomposite via 1-step technique. Scale bars are both 2 µm. Right side is measured electronic conductivity of Nafion (neat), GO-Nafion, GS-Nafion 2-step and GS-Nafion 1-step materials all measured at a near 0% relative humidity. Reproduced with permission from Ansari et al. (2010) [100].

dispersion within the polymer matrix. The results of the electronic conductivity were completed in a glove box after the films were dried on a hot plate for at least 3 h, ensuring that almost no water was present in the films (RH < 1 ppm), which made certain that there was an insignificant ionic conductivity from the Nafion® matrix. The results of the conductivity measurements revealed electrical conductivity for the Nafion and GO-Nafion materials to be under the limits of detection for our set up (< 1 x 10^{-9} S/m), which went up at least nine orders of magnitude for the reduced GS-Nafion 2-step material at 1.3 S/m. The GS-Nafion 1-step material had a conductivity value of 4 x 10^{-2} S/m.

2.4 Synthesis Technique for Nafion/GS/Pt Macroporous Nano-hybrid Materials

Using our previous nanocomposite synthesis techniques we would only have to include the catalytic platinum nanoparticles and introduce porosity into our nanocomposite system to have all the components for a catalyst layer material. We decided that a Polymer based nano-hybrid system would be the best course of action based on our previous work [100]. At only 5 wt% GS (2-step) we would have the necessary electronic conductivity to move electrons to and from the catalyst layer. We knew that Nafion was already the benchmark material for ionic conductivity in a PEM fuel cell, so we could expect good transport of protons by using Nafion as the polymer matrix. We decided to utilize ice templating to induce porosity, but ice templating also was able to help produce the last part of our catalyst layer—the platinum catalyst. By introducing a platinum precursor that was water soluble into the GO and Nafion aqueous suspension, we could then employ a dual in situ reduction of the GO into GS *while at the same time* reducing chloroplatinic acid to Pt NPs (Figure 2.5). Furthermore, the cryo-structuring can allow for various geometries such as cylinders if an appropriate mold is used to hold the suspension before introducing it to the temperature gradient; or even films, if freeze cast onto a thermally conductive substrate. The resultant material should allow for the facile synthesis of electrically conductive, macroporous hybrids in both films and bulk form comprised of graphene-supported platinum nanoparticles that are well-dispersed within an ionomer. We expected the microcellular scaffolds that were synthesized would combine high levels of ionic (Nafion®) and electronic (GS) conductivity along with catalytic activity (Pt) and, thus, should be ideal candidates for a catalyst layer in a PEM fuel cell. The three dimensional structure of the scaffold combined with the prevalent TPBs present

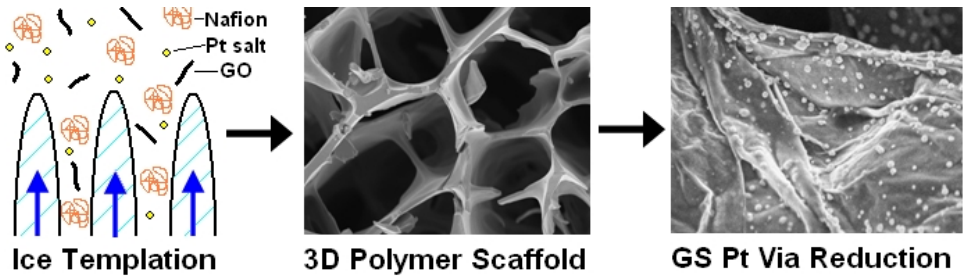

Figure 2.5: Schematic showing ice templating to synthesize a Nafion scaffold with Pt and GS precursors revealed upon reduction. Reproduced with permission from Estevez et al. (2010) [101].

should allow for the utilization of the catalyst layer, further away from the PEM. Finally, the fact that the nano-hybrid material is a Nafion® based scaffold should mitigate the various issues with non water permeable, carbon based catalyst layers [94].

2.4.1 Synthesis Methodology

For experimental rigor, it was decided to synthesize Nafion® (neat) macroporous materials as well as macroporous nano-hybrids. For the preparations of a typical Nafion® (neat) sample, 10 mL of aqueous dispersion of Nafion (10 wt%) was placed in a 20 mL glass vial, attached to a shaker table rotating at 280 rpm for 12 h (at room temperature) and then placed under vacuum to assist in the removal of air bubbles. An aluminum or copper foil was immersed into the aqueous dispersion to deposit a film. For the preparation of cylindrical and spherical bulk samples, the Nafion dispersion was loaded into copper cylindrical molds (sealed at one end with copper foil) or a drop was placed on the flat head (3.5 mm diameter) of an aluminum pin, respectively. The specimens were then plunged into a slurry of liquid and solid nitrogen (prepared by

keeping liquid nitrogen under vacuum for 15 minutes), then placed in a Styrofoam cup filled with liquid nitrogen and attached to a freeze drier (Labconco Freezone 12 plus) for two days. Finally, the samples were further dried at 80 °C for one hour.

For the preparation of hybrid samples, GO and chloroplatinic acid were introduced to 10 wt% aqueous dispersion of Nafion, sonicated for three hours and thoroughly mixed on a shaker table before being subjected to the identical freeze-casting protocol described above. After complete drying, the hybrid foams were treated with a 2 wt% aqueous solution of hydrazine at 80 °C for three hours to allow chemical reduction of GO and chloroplatinic acid hexahydrate to GS and platinum nanoparticles, respectively. Finally, the samples were dried in an oven at 80 °C for three hours. Assuming complete reduction, the final sample contained 5 wt% graphene and 10 wt% Pt. Reduction with sodium citrate was only different from the hydrazine treatment in that the solution was 5 wt%, the temperature was set at 85 °C and the time of the treatment was 15 hours.

CHAPTER 3

NAFION/GS/Pt POROUS NAN0-HYBRID SYSTEM FOR PEMFC CATALYST LAYER: CHARACTERIZATION AND RESULTS

3.1 Characterization Tools and Techniques

Scanning Electron Microscopy (SEM) and Energy Dispersive X-Ray Spectroscopy (EDS): The microstructure of the samples were investigated by a LEO 1550 FESEM operating between 2-20 keV. SEM sample preparation involved polishing the sample's surface with a cryo-microtome (Leica EM FC7). The sample was placed in the microtome's cryo-chamber which was kept at a temperature below -80 °C to ensure sufficient stiffness. Then using a diamond knife trimming tool (Diatome Cryotrim 45), progressively thinner slices of material were removed starting from a thickness of 5 microns until reaching a final polishing thickness of 30-50 nm. This approach allowed the sample to be examined at various depths. The microscope was equipped with a Bruker X-Flash 3001 SDD detector with a 10 mm^2 crystal and an energy resolution of 127 eV at Mn Kα edge to allow EDS studies.

X-Ray Diffraction (XRD): XRD spectra of the samples were recorded at room temperature using a Rigaku SmartLab X-ray Diffractometer (CuKα radiation, λ=1.54 Å).

Dynamic Mechanical Analysis (DMA): Compression measurements were carried out

using a TA Instruments DMA Q800 Dynamic Thermal Mechanical Analyzer. Sections of cylindrical samples (2-4 mm in diameter and 2-5 mm in length) were preloaded at 0.1 N. Stress-strain measurements were taken at a compression rate of 0.5 N min^{-1} until a maximum force of 5 to10 N was reached (depending on the stiffness of the sample).

Resistance measurements: Cylindrical samples (4-6 mm in length and 4 mm in diameter) were dried under vacuum at 50 °C for 24 hours before being transferred to a glove box with humidity content below 1 ppm. The samples were then placed in a device consisting of two silver plates as the electrodes, and silver paste was applied between the sample and the electrode to ensure minimal contact resistance. Resistance was measured using an Agilent HP 34401A DMM apparatus.

Cyclic voltammetry: Cylindrical samples were prepared by using ice templating techniques on previously mixed aqueous dispersions of graphite oxide (2 wt%) and chloroplatinic acid (10 wt%). Care was taken to ensure the composition of the samples were 90 dry wt% GO and 10 dry wt% Pt (post reduction). After sublimation of the samples, the samples were reduced in an aqueous solution of hydrazine and dried as described previously. Cyclic voltammetry (CV) was carried out at room temperature in a deaerated 0.1 M H2SO4 solution with/without 1 M MeOH to evaluate the catalyst activity for methanol oxidation using a Solartron electrochemistry station. Working electrodes were prepared by mixing 5 mg of catalyst with 1 mL of Nafion (0.05 wt % Nafion dissolved in ethanol) solution. The mixture was sonicated and 10.0 μL were applied onto a glassy carbon disk (ϕ=5 mm). After solvent evaporation, a thin layer of

Nafion-catalyst-Vulcan ink remained on the GC surface to serve as the working electrode. A Pt wire was used as the counter electrode and a reversible hydrogen electrode (RHE) in the same electrolyte as the electrochemical cell was used as the reference electrode. All potentials are referred to RHE.

3.2 Characterization Results – Structure and Electrochemistry

Nafion® and (Nafion)-(GO)-(Chloroplatinic acid) suspensions were prepared as denoted previously in 2.4.1. Nafion® (neat) macroporous scaffold were first investigated (Figure 3.1) and all three geometries were fabricated (Figure 3.1α). Nafion® suspensions in water considerably thicken when subjected to prolonged and vigorous mechanical stirring that is required in order to ensure a homogenous dispersion (especially in the presence of nano-fillers). Although investigation of this rheopectic behavior [102, 103] falls beyond the scope of the present study, we note that it has a significant impact on the morphology of the resultant cryo-structured scaffolds. In particular, the scaffolds derived from the unsheared Nafion® dispersions are composed of well-defined ribbons periodically interconnected with transverse pillars (Figure 3.1a). In contrast, the scaffolds prepared from the sheared, more viscous Nafion dispersion show instead an interconnected porous 3D geometry (Figure 3.1b). Evidently, the more viscous sheared sample seems to favor the formation of larger ice crystals that enhance the branching of the structure. In addition to viscosity, the structure/morphology of the sample is determined by the speed of the ice front, the particle size of the species in dispersion, the osmotic pressure and the surface tension of the suspension [65, 104].

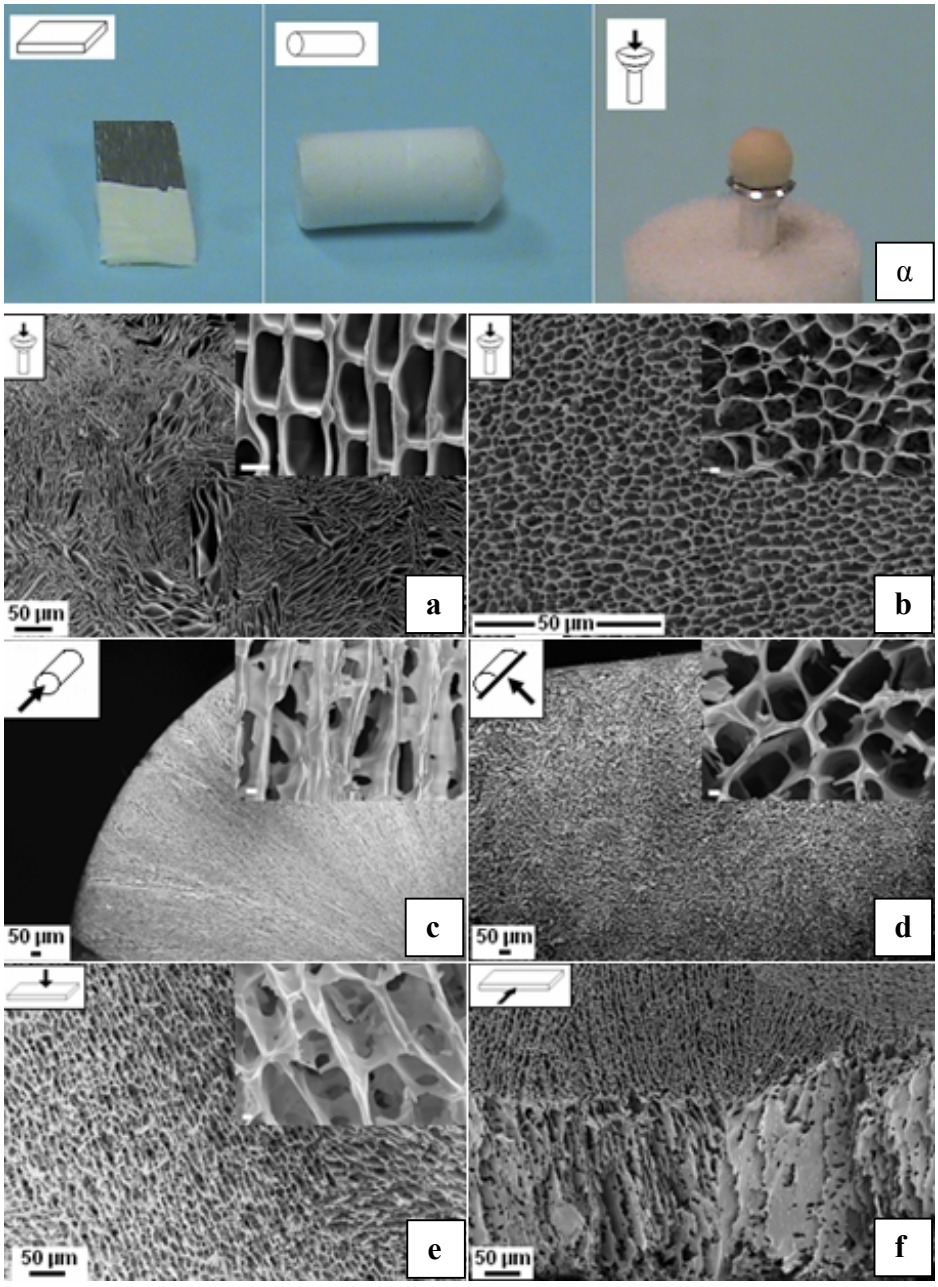

Figure 3.1:(α) Pictures and schematic drawings of cryo-structured Nafion scaffolds prepared by; (left) film deposition to an aluminum substrate, (mid) using a cylindrical mold and (right) processing a spherical drop. SEM images of Nafion (neat) foams: from (a) unsheared and (b) sheared aqueous suspensions, (c) cylindrical samples viewed along the axis or (d) across the thickness and deposited films viewed (e) across the thickness or (f) the edge plane. Insets at the top right of each image show a high resolution SEM image with each scale bar representing one micrometer. Reproduced with permission from Estevez et al. (2010) [101].

In addition to single component cellular solids, hybrid samples containing well-dispersed GS and platinum nanoparticles were prepared following a similar approach. A substrate was immersed in a homogenous aqueous dispersion consisting of Nafion®, graphite oxide (GO) and chloroplatinic acid (alternatively, for bulk samples the dispersion was carefully loaded into the mold) and was subject to freeze-casting. The resulting macroporous film was treated with a reducing agent (hydrazine or monosodium citrate) to allow chemical reduction of GO and chloroplatinic acid to GS and Pt nanoparticles, respectively (Figure 3.2). We have recently demonstrated that even in solid Nafion® samples, the nanoporosity due to the presence of ionic domains allows sufficient access of the reducing agent into the sample despite the lack of macroporosity [100]. In this work the macroporous nature of the samples further facilitates the diffusion of the reducing agent throughout the polymeric skeleton, so that the nanoparticle precursors, even those that reside in the vicinity of the substrate, can be readily accessed (vide infra). Thus far, the use of precursors to ice-templated structures has been limited to using preceramic polycarbosilane for the preparation of ceramic scaffolds with desired morphology [105, 106] and polycondensation of tetramethoxysilane within PVA cryogels [107] Additionally, in situ polymerization of N-isopropylacrylamide within cryostructured clay foams has been described [108]. In a distinctly different approach, preformed cellulose aerogels were used as templates for the deposition of magnetic precursors and the subsequent evolution of magnetic nanoparticles along the surface of the nanofibris [109]. To our knowledge, this is the first time that a one-step, redox reaction has been used to transform two precursors to the corresponding nanoparticles.

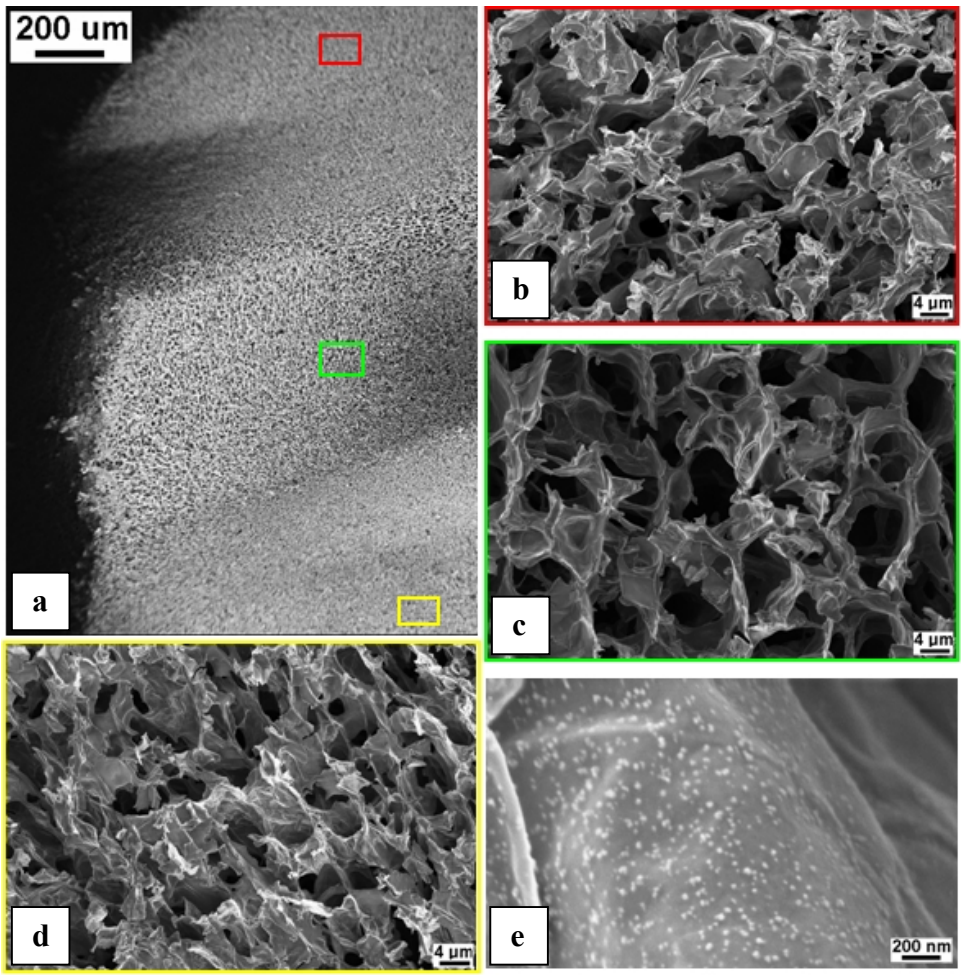

Figure 3.2: SEM images showing a) a monolithic Nafion/GS/Pt nano-hybrid that has been cut/polished into three distinct regions that upon closer inspection reveal that the b) bottom c) top and d) middle of the monolith has a similar macroporous structure. A HR SEM image reveals e) the Pt nanoparticles on the surface of the Nafion/GS/Pt scaffold. Reproduced with permission from Estevez et al. (2010) [101].

A Nafion/GS/Pt film thus prepared was carefully sectioned at three different thicknesses (figure 3.2, vide supra) to allow SEM imaging of its outer surface, the middle, and near the substrate. The SEM images suggest a homogenous distribution of the inorganic nanosheets and the platinum nanoparticles within the macroporous scaffold, even in the section closest to the substrate. Individual graphene nanosheets

on the surface of the Nafion® can be clearly identified by virtue of their characteristic crumpled texture (Figure 3.3a). After hydrazine treatment, it can be seen that the majority of platinum nanoparticles are attached to the surface of graphene sheets (Figure 3.3b). This observation points to the ability of the (initially present) oxygen atoms to act as anchoring points for the absorption of chloroplatinic acid [110] and/or the efficacy of the defect sites of GS to nucleate Pt nanoparticles [111]. The XRD pattern shown in Figure 3.3d exhibits diffraction peaks at $2\theta = 39.7^{o}$, 46.3^{o}, 67.4^{o} and 81.3^{o} that can be identified as the Pt (111), Pt (200), Pt (220) and Pt (311) reflections of the platinum fcc crystals [112]. The elemental spectra obtained by Energy Dispersive X-Ray Spectroscopy (EDS), shown in Figure 3.4 (vide post), confirm the coexistence of Cl and Pt before reduction and the complete removal of Cl after chemical treatment. Taken all together, experimental evidence supports the presence of platinum nanoparticles after chemical reduction of the chloroplatinic acid. Previous reports suggest that GS can function as an excellent supporting platform for Pt nanoparticles, inhibiting their agglomeration and stabilizing their catalytic performance [113-116] due to its much higher surface to mass ratio compared to all other carbon supports (e.g. carbon black, carbon nanotubes and carbon nanofibers). Cyclic voltammetry tests (Figure 3.5, vide post) confirm that the platinum nanoparticles exhibit a certain level of catalytic activity, in line with the average size of 50-100 nm of the nanoparticles. Substituting hydrazine by monosodium citrate as the reducing agent (but otherwise following an identical protocol) gives rise to much smaller platinum nanoparticles having an average diameter close to 10 nm (Figures 3.3d-e).

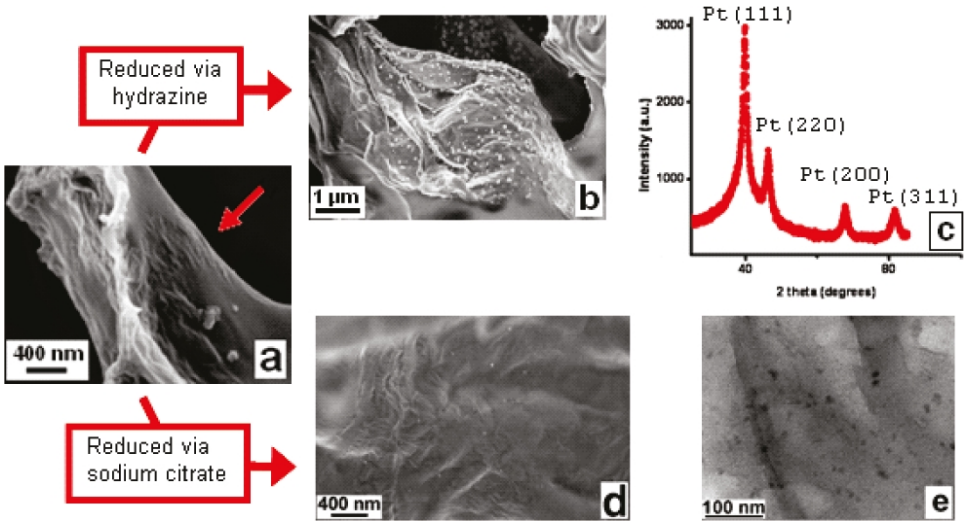

Figure 3.3: (a) SEM image of a freeze-cast Nafion/ GS/ Pt film showing the presence of graphite oxide nanosheets (red arrow) on the surface of the macropores. (b) Platinum nanoparticles deposited on the surface of graphene, after hydrazine treatment and (c) their XRD spectra. (d) and (e) SEM amd TEM images respectively of platinum nanoparticles deposited on the surface of graphene, after treatment with monosodium citrate. Reproduced with permission from Estevez et al. (2010) [101].

Under anhydrous conditions the ionic conductivity of Nafion® is low enough to be considered insignificant and thus, a meaningful comparison between the electronic conductivities of the various samples can be made, provided that they have similar geometry and porosity. For convenience, we have tested the resistivity of cylindrical samples composed of Nafion/GO prior to and after hydrazine treatment at low relative humidity (<1ppm). The resistance of the non-reduced Nafion/GO exceeds the upper detection limit of our device (~ 200 MΩ). After hydrazine treatment the resistance falls in the range of few kΩ (10-20 kΩ). Thus, hydrazine treatment results in at least 4 orders of magnitude decrease in resistance, consistent with extensive chemical reduction of the insulating GO to more conducting graphene. Taking into account the high pore volume of the sample (c.a. 92%) and applying the additivity rule, we

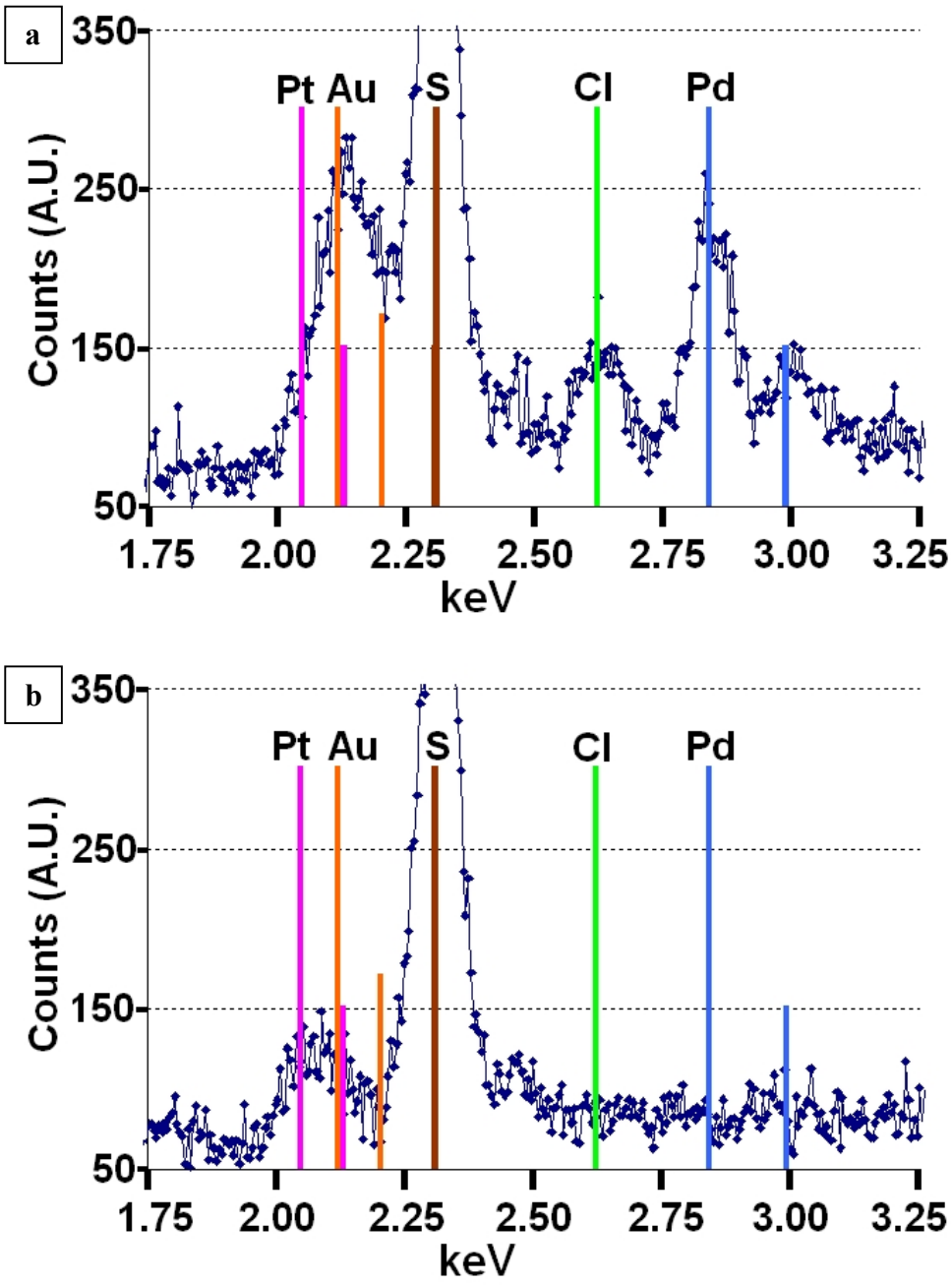

Figure 3.4: EDS spectra of the cryo-structured Nafion/GO/chloroplatinic acid hybrids (a) before and (b) after hydrazine treatment. The Cl peak (2.62 keV) is clearly diminished after reduction. The Au (2.12 and 2.20 keV) and Pd (2.84 and 2.99 keV) peaks seen before reduction are from sputtering the sample with Au/Pd in order to minimize SEM charging. Reproduced with permission from Estevez et al. (2010) [101].

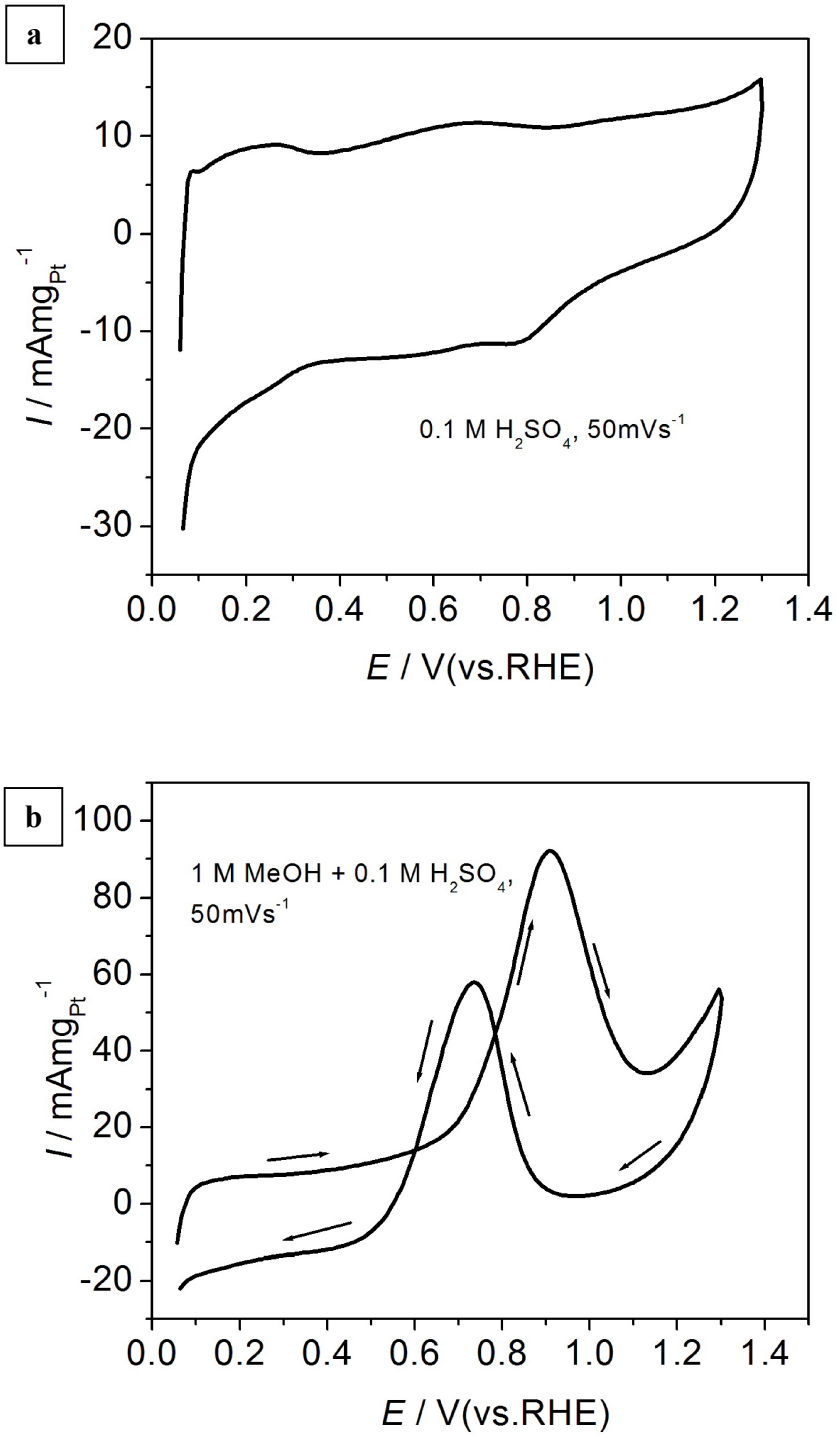

Figure 3.5: Cyclic voltammogram of (a) GS-Pt sample in 0.1M H_2SO_4 and (b) the same sample under methanol oxidation. Reproduced with permission from Estevez et al. (2010) [101].

estimate the electronic conductivity of the solid hybrid to be in the order of 1 S/m, in good agreement with values reported previously for our Nafion/GS nanocomposites [100]. We note that the high electronic conductivity of the cellular Nafion/GS hybrid effectively prevents the accumulation of electronic charges at its surface during SEM imaging, as opposed to the (non reduced) Nafion/GO sample that requires sputtering with an electronically conductive material to minimize charging effects during imaging (see Figure 3.4, vide ante). Electronic conductivity induced by carbon nanotubes [49, 117-118] or carbon black [50], has been reported in various cryo-structured scaffolds.

3.2.1 Characterization Results – Mechanical Properties

The mechanical properties of the materials were evaluated using compression testing**.** Figure 3.6a-b shows typical compressive stress-strain plots for our samples. In general, the stress-strain curves exhibit a behavior typical of cellular solids. At small strains the material behaves elastically and the slope of the curve equals the compressive modulus of the material. At higher strains the material compacts gradually until it starts collapsing and the stress starts to increase sharply. The morphology, and thus, the mechanical response of the samples can be fine-tuned by thermal annealing. The modulus of the sample annealed at 80 ^{o}C (e.g. following our standard preparation protocol) is 60 kPa despite its high pore volume (> 90%). The sample shows no structural changes after annealing at T_a=95 ^{o}C for a period of several days (see Figure 3.6c). However, upon annealing at temperatures close to or above the glass transition, T_g, of Nafion® (T_g ~ 120 $^{\circ}$C) [98] for one hour, the density and

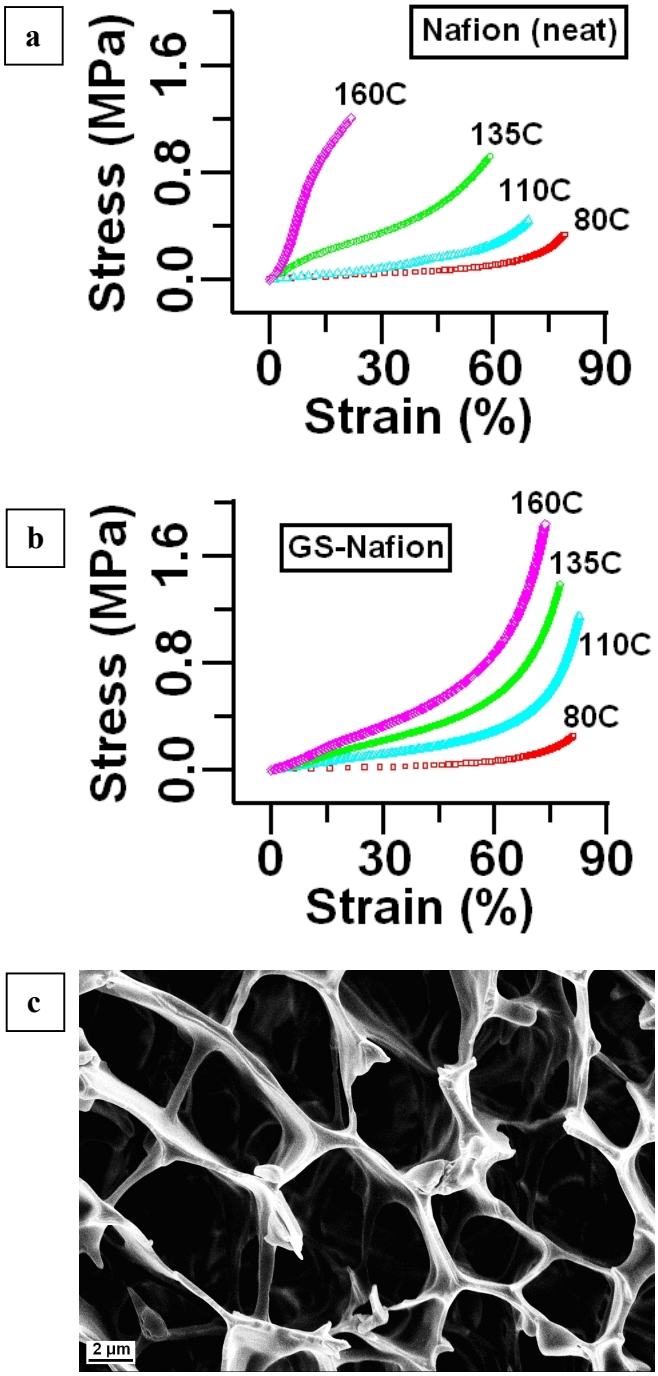

Figure 3.6: Compressive stress- strain curves for cryostructured cylindrical scaffolds of: (a) Nafion and (b) Nafion/GS that have been subject to thermal annealing (for 1h) at the temperatures indicated and (c) SEM imaging of a neat Nafion cryostructured scaffold annealed at 95 ^{o}C for 4 days. Reproduced with permission from Estevez et al. (2010) [101].

cell thickness monotonously increase with annealing temperature, resulting in significant mechanical reinforcement (Figure 3.7). The compressive modulus and the pore volume of the sample annealed at 160 ^{o}C are 7.6 MPa and 49.2 vol%, respectively. The corresponding compressive moduli of the Nafion/GS hybrids are somewhat higher than those for neat Nafion® suggesting that incorporation of GS provides some degree of reinforcement. Interestingly, the thermally induced structural rearrangements observed in neat Nafion® are greatly suppressed in the Nafion/GS hybrids (Figure 3.7, vide post). This behavior can be attributed to the large increase in T_g of Nafion® in the presence of inorganic nanoplatelets (by as much as 50 ^{o}C) [102] and the formation of a percolated network of nanofillers that enhances the thermomechanical stability of the scaffold.

3.3 Conclusions

In summary, we report a novel approach to prepare electrically conductive, macroporous hybrids in both films and bulk form comprised of graphene-supported platinum nanoparticles which are well-dispersed within an ionomer. The films can be deposited directly to the surface of any substrate, simply by dip coating followed by freeze-casting. The method is simple, scalable and applicable to a variety of systems. The microcellular scaffolds combine high levels of ionic (Nafion®) and electronic (GS) conductivity along with catalytic activity (Pt) and, thus, are ideal candidates for a catalyst layer in a PEM fuel cell.

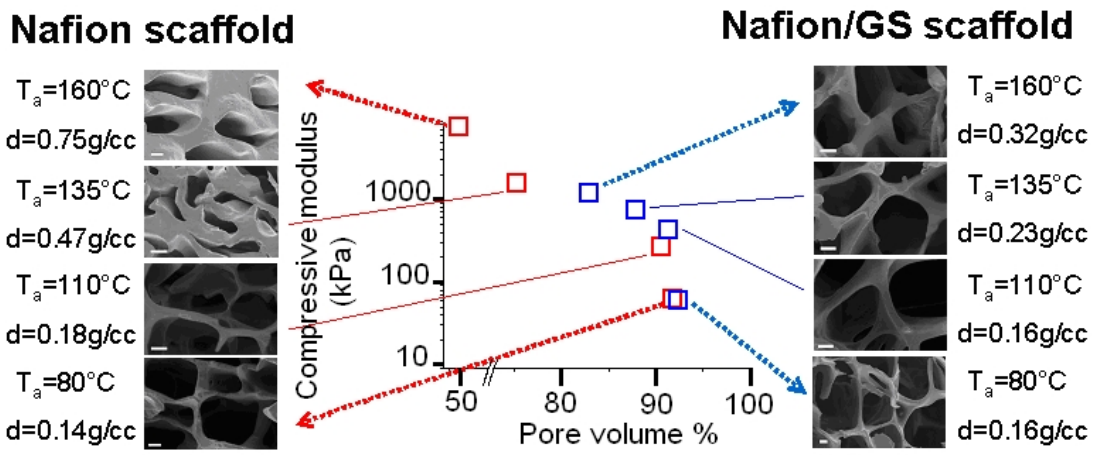

Figure 3.7: Compressive modulus as a function of the pore volume of cylindrical neat Nafion and Nafion/GS scaffolds that have been subject to thermal annealing (for 1h) at the indicated temperatures (T_a). The data points are also correlated with the SEM pictures of the corresponding annealed scaffolds where the scale bar represents one micrometer. The densities of the scaffolds are also indicated. Reproduced with permission from Estevez et al. (2010) [101].

This work herein represents a novel *polymer* based nano-hybrid system greatly differing from other catalyst layers. Furthermore, the fact that Nafion® was chosen as the organic material is important for the catalyst layer, not only because of Nafion®'s superior ionic conductivity, but due to water management at the cathode always being an important issue to keep in mind. This is due to the half reaction that occurs at the cathode, where one of the end products is water. Since most of the current catalyst layer designs are carbon based (hydrophobic) materials and composites, water buildup can occur at the cathode. The water can clog the pores and leave portions of the cathode inaccessible to the oxygen gas, greatly reducing the three dimensional aspect of the electrode and the amount of TPBs available [94]. Since Nafion® is so permeable to water (in fact absorbing it increases the ionic conductivity), the water can be pulled away from the cathode, potentially mitigating this issue. Also the fact

that the GS within the hybrid material greatly increases the T_g of the material means that the material can withstand higher temperatures. This is not only important for the thermal stability at higher temperatures, but it allows the material to be annealed, increasing the mechanical properties that the GS filler already imbues onto the hybrid system.

CHAPTER 4

HIERARCHICAL POROUS CARBON MATERIALS: SYNTHESIS

4.1 Introduction

Recently, hierarchical porous carbons (HPCs) possessing well-defined macropores and interconnected meso- and micropores, have attracted a lot of attention [74, 119-126]. HPCs can combine in one system: improved mass transport facilitated by the macropores and high surface area and pore volume from micro-/mesopores [119, 127-129]. Such hierarchically porous carbons provide better accessibility and active sites for several energy and environmental applications including electrode materials for batteries [128, 130], supercapacitors [119, 127, 131-133], fuel cells [134-135], and capacitive deionization [136-137], as well as sorbents for CO_2 capture [138].

A large number of techniques have been explored for the synthesis of HPCs [139, 140]. In general most of the techniques for producing carbons combining macro- and mesoporosity are based on a dual templating strategy, where two templates with dimensions at different length scales are combined to generate the multimodal pores. These techniques either involve two hard templates [141, 142], or a combination of hard and soft templates [143, 144]. Removal of the templates, either through decomposition or etching leaves behind a porous scaffold. Other techniques involve template replication of hierarchical inorganic materials [145, 146], with hierarchical silica being the most commonly used template. The sol-gel method is another widely

used technique for the production of hierarchical carbon, commonly termed as either carbon aerogels [139, 147-148] or carbon cryogels [149, 150]. Ice templating has also been explored for assembling micropore-mesopore dominated carbon materials, such as CNTs, into 3D interconnected hierarchical carbon materials [135, 151].

A major challenge to date has been the development of HPCs, which can exhibit high surface areas, pore volumes and porosities at all three different length scales: macro-, meso-, and micro, in a simple material platform. Additional challenges with the synthesis techniques include the requirement to synthesize porous inorganic materials or special nanoparticles as hard templates, which involve multiple steps and are thus time consuming and costly. Furthermore, most of the soft templates used are based on surfactants and block-copolymers, which are rather expensive and non renewable [140]. Moreover, the size of the mesopores can also be difficult to tune because of aggregation of the nanoparticles in the polymerizing carbon precursor matrix [83], as explained previously in section 1.8. In addition, techniques like sol-gel suffer from the critical drawback associated with the long synthesis period required for gelation, solvent exchange and supercritical drying in the case of aerogels [139].

4.2 Synthesis of the HPC Materials

The end goal of this synthesis approach was to design a procedure for an open, vascular-like network of porosity. The idea was to have large macropores, whose pore walls were made up of smaller mesopores and micropores. Figure 4.1 shows a representative monolith of this vascular-like network concept. By having such an open

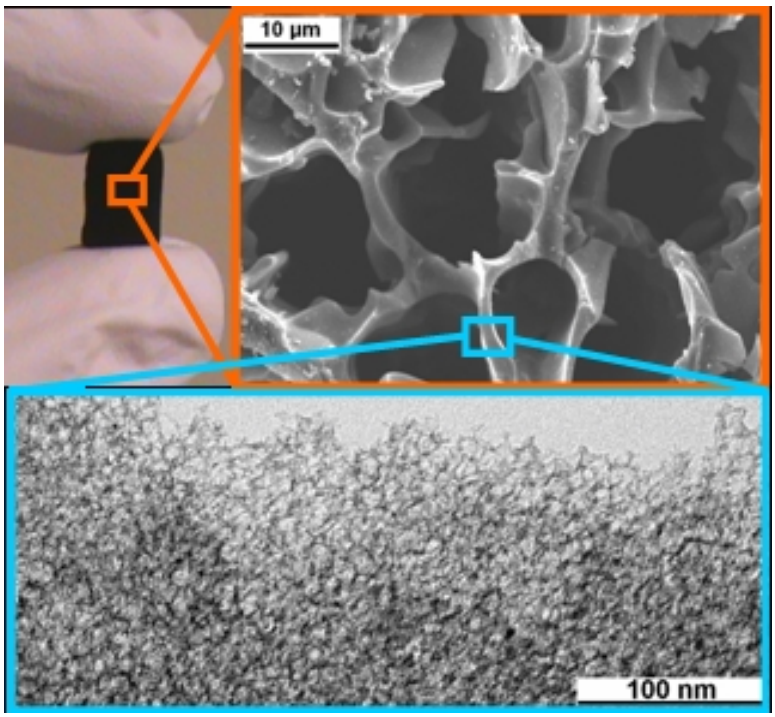

Figure 4.1: Concept of a HPC material with a hierarchy of pore sizes spanning several orders of magnitude. The larger macropores have walls that are made up of smaller meso/micropores. The macropores have sizes in the 1-10 µm range, while the smaller pores are at least an order of magnitude away (< 100 nm) in length. Reproduced with permission from Estevez et al. (2013) [152].

structure, we believed easy access to the high surface area active sites would enable a mitigation of kinetic barriers as described in section 4.1 (vide ante). We also wanted a synthesis route that could be tunable, facile and scaleable by using commonly available, inexpensive components and techniques. Furthermore, with many previous techniques employing toxic and nonrenewable chemicals, we wanted the synthesis to avoid these and be more of a green chemicals based procedure.

To synthesize our HPC materials, we decided to employ three different techniques to induce three different levels of porosity. This would enable us to differentiate the three

different levels of porosity by merely modifying the corresponding synthesis method. Approaching the synthesis in such a fashion would enable us to have a level of tunability which we wanted in our HPC system.

4.2.1 Synthesis of the HPC Materials – Macroporosity and Mesoporosity

In order to synthesize the macropores in our HPC system we decided to use an ice templating route (see section 1.6 for a more in depth treatment of ice templating). The synthesis procedure proposed (Figure 4.2) was to use ice templating with a suspension of carbon precursor together with a template material that would be used to form the mesopores. This was accomplished by producing a well dispersed aqueous suspension of colloidal silica and glucose. The suspension was then plunged into liquid nitrogen (Figure 4.2a) solidifying the water and structuring the glucose and silica as it was expelled from the growing ice crystals. The resultant ice-silica-glucose system was then placed in a freeze dryer to promote sublimation of the ice, removing it from the material leaving behind macropores. The sublimation removes the water while circumventing water's liquid phase, which keeps the macropores from collapsing. The freeze drying process also dries the remaining porous silica-glucose nano-hybrid material into a solid material (Figure 4.2b). Next, the macroporous silica-glucose hybrid is heated in a furnace in a nitrogen environment to carbonize the glucose. After carbonization, the mesoscale colloidal silica (2-50 nm) is etched out of the macroporous silica-carbon system which results in a HPC with large macropores (> 1 µm) whose pore walls are made up of mesopores (figure 4.2c). The two templating techniques can be tuned independently of each other and thus provide a facile way to

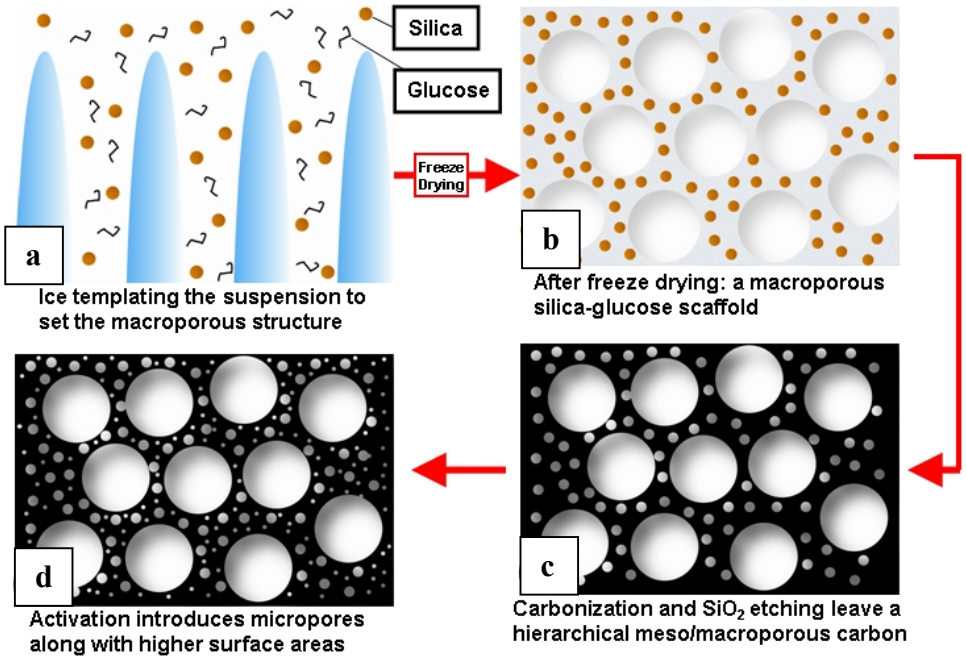

Figure 4.2: Schematic showing the basic steps and the material thus produced after each step. The four steps shown clockwise from top left are: a) (side view) Ice templating - ice front movement through the glucose and colloidal silica aqueous suspension forming ice crystals, b) (top view) Freeze drying - the glucose-silica composite material with macropores after removal of ice, c) (top view) Carbonization and silica etching - Macro-mesopore dominated carbon and finally, d) (top view) Physical activation - Hierarchical carbon. Reproduced with permission from Estevez et al. (2013) [152].

control macro- and mesoporosity. Though ice templating is a recently explored templating technique, there has been considerable progress in tuning both the size and structure of the macropores produced [64, 153]. For the mesoporous control via colloidal silica, tuning the size can merely be as simple as exchanging one mesoporous sized silica for another. Though previous work [83] has shown the difficulties of keeping a tight mesopore size control due to phase induced aggregation when using colloidal silica as a template, the ice templating works to mitigate this without the use of surfactants. This is due to the fact that once the silica-glucose structure is “locked

in" to the solid hybrid material (shown in Figure 4.2b, vide ante) there is no capability for the two components to move away from each other and aggregate. It is important to note that microporosity is present as a function of the carbonization of the glucose, but until the final activation step (section 4.4.1) the porosity is dominated by meso- and macropores. An additional mesoporous tuning method that can be employed is multiple mesopore sizes. By using different sized colloidal silica nanoparticles, differently sized mesopores are potentially possible.

4.2.2 Synthesis of the HPC Materials – Microporosity through Activation

Before the final step, the material is an interconnected HPC dominated with meso- and macropores (Figure 4.2c, vide ante). In order to enhance the microporosity, a final activation step is undertaken (Figure 4.2d, vide ante). The activation process adds microporosity to the HPC which now has macropores from the ice templating, mesopores from the silica template and micropores from the activation of the carbon. The three different pore forming strategies ensure that a level of tunability is available at all three different pore size regimes (micro-, meso- and macro-).

Activated carbon materials have been used commercially for quite some time now. Papers can be found from roughly a century ago exploring their use as absorbents in gas masks during World War I [155]. Of the various types of activation techniques available, we chose to concentrate on physical activation, specifically CO_2 activation (henceforth referred to as "activation").

For a carbon material undergoing activation by CO_2, a flow of CO_2 gas over the carbon material at 950 °C is maintained for a set period of time (typically measured in hours). The resultant reaction that occurs:

$$C + CO_2 \rightarrow 2CO \qquad \Delta H = +159 \text{ kJ/mol} \qquad (1.1)$$

is one where the carbon atoms are "plucked" from the surface of the carbon material. As Eq. 1.1 indicates, the reaction is endothermic thus heat must be applied for the reaction to take place (temperature used is typically 800-1000 °C) [76]. Because of this, the process can be thought of as a *controlled* oxidation of the carbon. The difference of course being that oxidation of carbon is highly exothermic and thus, not as easily controlled. Therefore it is important to *not* think of the activation process as one where the CO_2 gasifies the first carbon atom it encounters; rather, there may be as many as 10^{17} carbon atoms encountered before one is gasified, indicating that a selection process of some sort occurs [76]. The exact mechanism of the activation process is beyond the scope of this work, but it needs to be mentioned that the whole process is not as simple as Eq. 1.1 may seem to indicate. For the purposes of this work, we followed a standard activation technique (with minor variations) that can be found in the literature [154].

4.3 Synthesis Methodology

In a typical synthesis, 10 g of a 15 wt% suspension of 4 nm colloidal silica and 1.5 g of glucose D are added to a 50 mL centrifuge tube and mixed well. Next the centrifuge tube (uncapped) is plunged into liquid nitrogen. Once the ice front (traveling radially from outside in) meets at the center of the suspension, the whole tube is submerged in

the liquid nitrogen bath. The frozen sample is then subjected to freeze drying until the sample is completely dry. The freeze-dried glucose-silica composite is then pyrolyzed at 1000 ºC at a ramp rate of 3 ºC/min for a dwell time of 3 h under a nitrogen or argon environment, resulting in a carbon-silica composite. This carbon-silica composite is then placed in a 3M NaOH solution at 80 ºC overnight under medium stirring to etch out the silica. The sample is finally washed with deionized water until a neutral pH is reached and dried at 80 ºC for at least 12 hours before use. The sample can then be broken up with a spatula to form a powder. Where a macroporous monolith is needed, the samples are synthesized in a brass mold (see section 5.2.1 for more details on monolithic samples) depending on the geometry desired. Typical monoliths are cylinders of roughly 5-10 mm in diameter and 5-10 mm in length. For convenience the samples are denoted by KCU-C *x*-*y*, where *x* represents the average colloidal silica size (nm) and *y* represents the ratio of silica to glucose (by weight) in the original suspension. KCU-C stands for (K)AUST(C)ornell(U)niversity-(C)arbon. To introduce significant microporosity, CO_2 activation is used. Specifically for CO_2 activation, the sample (after silica etching) is heated first under an inert atmosphere up to a temperature of 950 ºC, whereupon the inert gas is replaced by CO_2 at a flow rate of 50 cc/min. The time for activation varies from 1 – 4 h. CO_2 activated samples are denoted by KCU-C *x*-*y*-*z*, where *z* represents the duration (h) of CO_2 activation.

CHAPTER 5

HIERARCHICAL POROUS CARBON MATERIALS: CHARACTERIZATION

5.1 Characterization Tools and Techniques

Scanning Electron Microscopy (SEM) and Energy Dispersive X-Ray Spectroscopy (EDS): The microstructure of the samples was investigated by using a LEO 1550 FESEM operating between 2-20 keV. SEM sample preparation involved polishing the samples' surface via a cryo-microtome (Leica EM FC7). Each sample was placed in the microtome's cryo-chamber, which was kept at a temperature below -80 °C to ensure sufficient stiffness of the sample. Then using a diamond knife trimming tool (Diatome Cryotrim 45), progressively thinner slices of material were removed starting from a thickness of 5 microns until reaching a final polishing thickness of 30-50 nm. This approach allowed the sample to be examined at various depths. The microscope was equipped with a Bruker X-Flash 3001 SDD detector with a 10 mm^2 crystal and an energy resolution of 127 eV at Mn Kα edge to allow EDS studies.

Transmission Electron Microscopy (TEM): TEM images were obtained using an FEI T12 Spirit TEM/STEM. The T12 is a 120 kV field emission TEM, equipped with a LaB_6 filament and an SIS Megaview II CCD camera. The sample was ground and then added to a vial with ethanol. The sample was then sonicated and physically mixed by shaking the vial. After roughly 45 s, with the larger particles settling to the bottom of

the vial, the top of the vial was pipetted out and placed on a carbon coated copper TEM grid.

Dynamic Mechanical Analysis (DMA): Compression measurements were carried out using a TA Instruments DMA Q800 Dynamic Thermal Mechanical Analyzer. Cylindrical samples (all approximately 8 mm in diameter and 10 mm in length) were preloaded at 0.001 N. Stress-strain measurements were taken at a compression rate of 0.5 N/min until a maximum force of 18 N was reached. Measurements were taken at ambient temperature and pressure.

Electrical Conductivity Measurements: Electrical conductivity measurements were obtained by a four point probe setup. The probe was set up so that the sample (in powder form) was in an insulating cylinder with two conductive pistons on either end which are able to squeeze the powder together. By using a spring the amount of force applied to the pistons and thus, the pressure on the powder could be measured. Two small pinholes in the side of the cylinder allowed for two narrow conductive pins to contact the KCU-C powder. The pins allowed the voltage drop to be measured in the compacted powder as a current was applied through the conductive pistons. The pressure applied to the KCU-C powder was above 8000 psi, to minimize the void space of the material measured.

Mercury Porosimetry: Monolithic samples were analyzed using mercury intrusion via a Micromeritics AutoPore IV (9500 Series) porosimeter. The cylindrical monolith

samples were cut in half (axially) to fit into the penetrometer sample holder. Care was taken to analyze the data up to a pressure of 3617.27 psia, ensuring that pores sized below 50 nm were not analyzed. The apparent density was calculated by the AutoPore IV by measuring the volume of the sample at 0.60 psia and using the weight measured by the operator.

Nitrogen Porosimetry: Nitrogen adsorption-desorption tests were carried out at 77K using a Micromeritics ASAP 2020 analyzer. Prior to gas adsorption measurement, the samples were degassed at 150 ºC under vacuum for at least 12 hours. The specific surface area was calculated using the Brumauer-Emmett-Teller (BET) method. The pore volume was estimated from single point adsorption at a relative pressure of 0.994. The pore diameter was determined from the adsorption branch, according to the Barrett-Joyner-Halanda (BJH) method.

Microporosity characterization via CO_2 adsorption: CO_2 adsorption-desorption tests were carried out at 273K using a Micromeritics ASAP 2050 Xtended Pressure Sorption Analyzer. Prior to gas adsorption, the samples were degassed at 180 ºC for 16 hours, under vacuum. The absolute pressure range used was roughly 0.03 bar to 10 bar. The pore size distribution was calculated using density functional theory, using CO_2 at 273K on carbon with the pores represented as slits for modeling purposes.

Reflection Raman Microscopy: Samples were used in powder form and Raman characterization was accomplished via a Renishaw InVia Confocal Raman microscope. The excitation frequency of the laser was at a wavelength of 488 nm.

X-ray Diffraction (XRD): XRD characterization was accomplished with a Scintag Theta-Theta X-ray Diffractometer. Samples were loaded into the diffractometer as a powder.

5.2 Characterization Results

5.2.1 Characterization Results – Macroporosity

Samples of KCU-C x-y HPCs were synthesized as indicated in section 4.3. For the purposes of this work, the macropore forming technique of ice templating was not modified beyond the standard protocol outlined in section 4.3. For the electrochemical device applications we had in mind, the mesoporosity and microporosity were deemed to be of greater importance and thus, prioritized. An interconnected macroporous network that would allow easy access to the higher surface area meso- and micropores was of paramount importance. In order to determine the nature and size of the ice templated macroporous structure, SEM imaging and mercury porosimetry were used. By obtaining SEM images of the freeze dried macroporous silica-glucose scaffold before carbonization (and subsequent etching of the silica) we were able to confirm the well dispersed silica colloids within the glucose matrix. Figure 5.1 shows the general fishbone-like structure which is prevalent before and after carbonization (Figures 5.1a and 5.1b respectively), as well as the silica-glucose nano-hybrid (Figure 5c, d). We also used Energy-dispersive X-ray spectroscopy (EDS) while imaging the

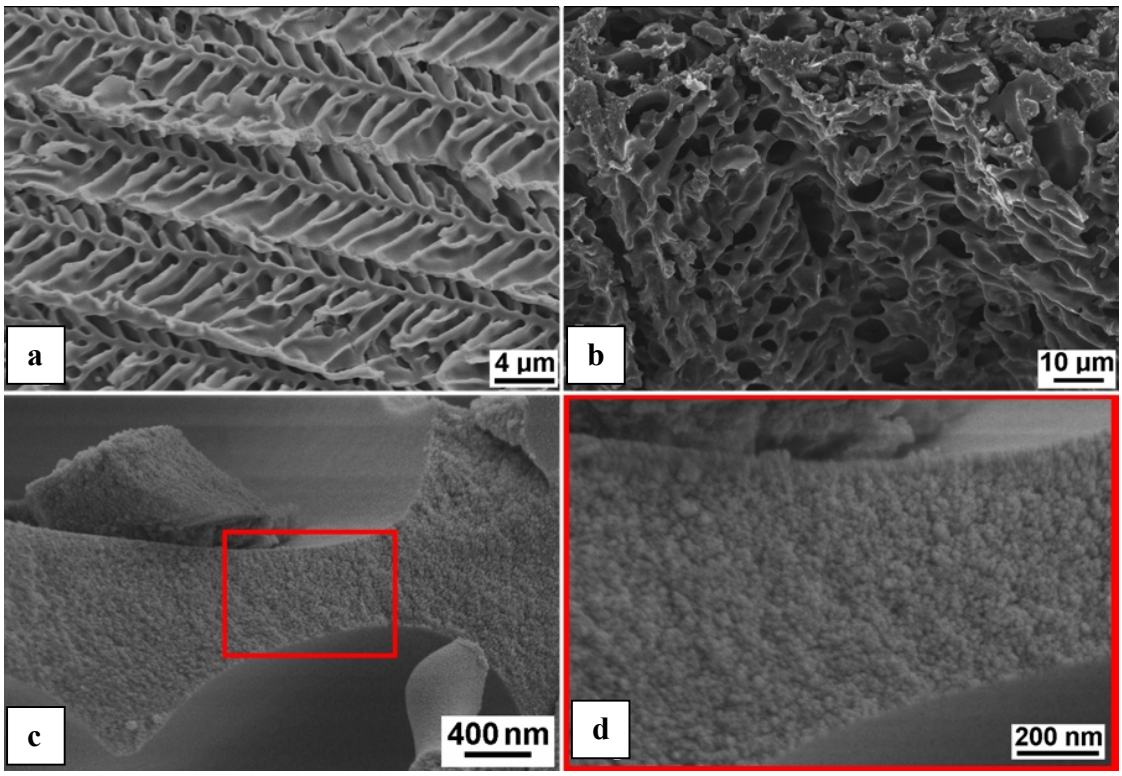

Figure 5.1: SEM images where the sample was cut and polished via microtome as described previously. The SEM images reveal (a) a fishbone like structure in the glucose-silica composite that is also seen in the (b) carbonized HPC material. HR-SEM images show (c) the macroporous walls of the glucose-silica hybrid material, in which the (d) colloidal silica can clearly be seen. Reproduced with permission from Estevez et al. (2013) [152].

samples before and after etching of the silica. The EDS data (Figure 5.2) confirmed that the silica was predominately removed after the etching procedure as the ratio of the silica to carbon peaks in the EDS data clearly shows a dramatic loss after the etching procedure. A representative KCU-C 4-1 (sample synthesized with 4 nm colloidal silica at a weight ratio of silica:glucose of 1:1) sample was used for all of the macroporous characterization unless otherwise noted. The mesoporous parameter space is explored in detail in section 5.2.2.

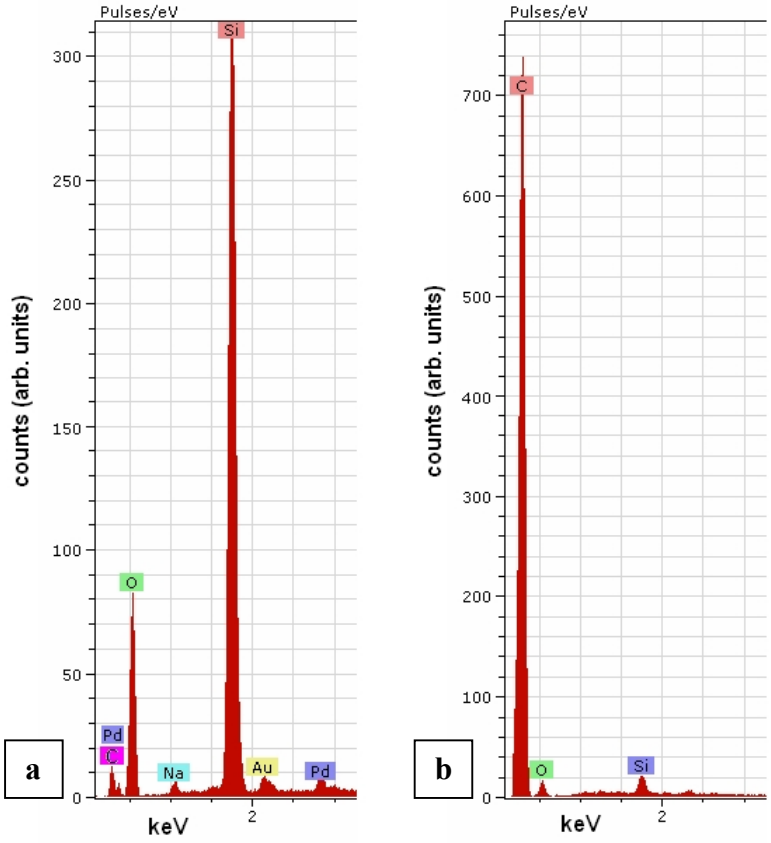

Figure 5.2: EDS data for macroporous silica-glucose sample (a) before carbonization and etching and (b) after etching. The Si:C ratio drops dramatically after etching indicating the removal of silica. Samples were measured while imaging under SEM by bombarding the sample at 20 keV for 60 s.

Mercury porosimetry is a technique that can best be used to characterize the macroporosity of a sample. The results of the macroporous pore size distribution measured by the Hg porosimeter are shown in Figure 5.3. As the mercury intrudes into a known volume, the pressure required to enter the various pores in the sample can be measured and through the use of models, the pore size can be estimated by how much Hg intrusion for a given pressure is obtained. The lower limits of porosity obtainable by Hg porosimetry is well within the mesoporous range for very high pressures

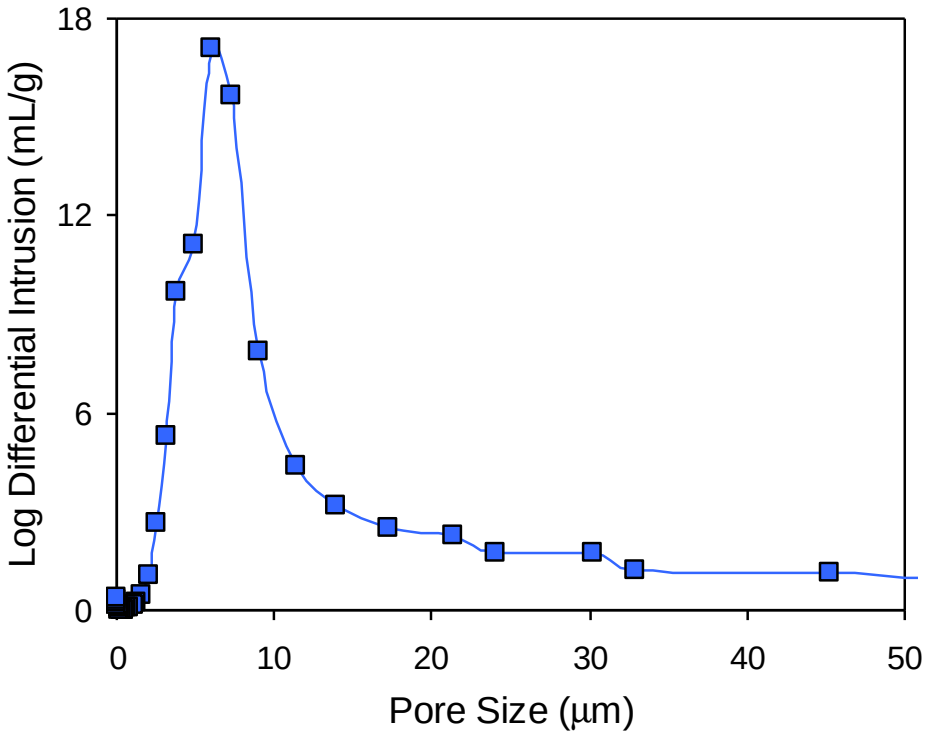

Figure 5.3: Pore size distribution via mercury porosimetry for the KCU-C 4-1 monolith sample. The pore size distribution shows macropores present mostly in the range from 3-12 microns. Some larger (above 15 µm) macropores are present, but to a relatively small degree. Reproduced with permission from Estevez et al. (2013) [152].

intruded and thus to measure only the macropores, care was taken to keep the pressure to a maximum value of 3617.27 psia. The KCU-C 4-1 sample was again used as the representative sample, but other KCU-C x-y samples had similar pore size distributions, surface areas and pore volumes (for only the macropores). The KCU-C sample was a cylindrical monolith (see section 5.2.2 for more details on monoliths) that was cut axially in half to fit into the Hg penetrometer bulb. The samples' macropores had a SSA of 11 m^2/g and a pore volume of 9.1 cm^3/g. The porosity present in the sample was measured to be 83%. The porosity % was measured by

holding the pressure at a very low value of 0.60 psia and by measuring the volume of the sample at that pressure. This information, combined with the mass of the sample and assuming a carbon density of 2.0 g/cm^3 revealed all the information to calculate the porosity %. The bulk density was also measured in such a fashion and was calculated to be 0.09 g/mL. The way the sample was loaded should not have allowed for any interparticle spacing and thus the bulk density was also probably the apparent density. This was confirmed by measuring representative cylindrical samples by their apparent volume and mass and getting similar results.

The Hg porosimetry pore size distribution reveals some porosity between 10-30 µm, but the vast majority of the macropores reside in the 3-12 µm range. Examining the broad peak between 3-12 µm, one can almost see two peaks deconvoluted into two distinct peaks between that range. Looking at the SEM images of the sample (Figure 5.4), one can see that the SEM images match up well with the porosimetry data and two different macroporous peaks appear to be present (Figure 5.4c). Further exploring the SEM images, one can see the large consistent macroporosity as demonstrated by Figure 5.4a. Figure 5.4a shows just over 1 mm^2 of the HPC monolith. The SEM images in Figure 5.4d reveal that the macropores of the sample have walls roughly 1 µm thick. This means that for a fluid that is flowing through the interconnected macroporous structure with minimal kinetic barriers, there is an average distance of roughly 500 nm of travel that must be passed through to reach the high surface area meso/micropores in the HPC material. This is important for applications such as electrochemical devices, where the electrolyte's ions must have easy access to the active sites, usually maintained within the high surface areas of the material.

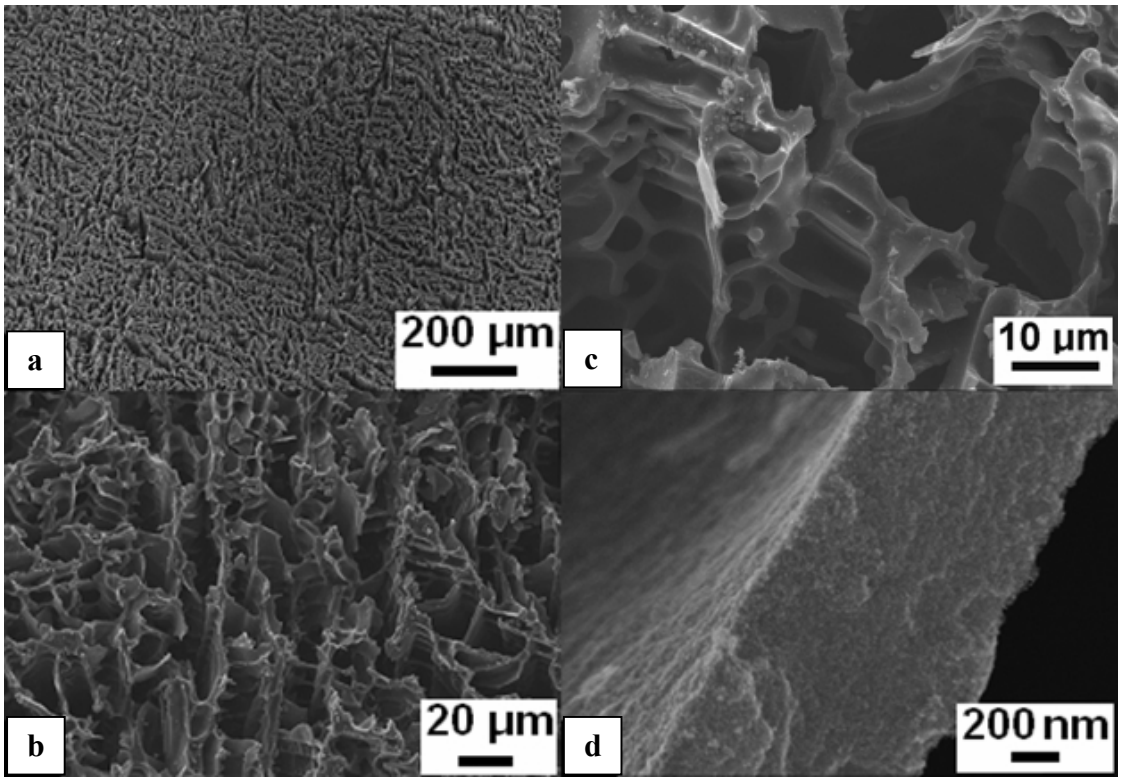

Figure 5.4: SEM images of KCU-C 4-1 monolithic cylindrical sample that was cut and polished via microtome. Images reveal (a) large scale macroporous consistency that upon higher resolution (b) reveals an interconnected macroporous network present. Higher resolution shows pores in the 3-12 µm range with anisotropic structure that has smaller pores along the sides of larger tubular pores. HR SEM exposes a roughened surface on the macroporous walls consistent with mesopores and a wall thickness of about 1 µm. Reproduced with permission from Estevez et al. (2013) [152].

5.2.2 Characterization Results – Monoliths

Monolithic porous carbon materials have come under recent interest due to their binderless ability to form electrodes, particularly for supercapacitor applications [156,

157]. The ability to use various molds allows a great many geometries and sizes to be at our disposal. An important note to consider is the length the ice front must travel before the sample is completely frozen. Since the sample is plunged into liquid nitrogen the ice front travels at a fast speed through the suspension. At a certain distance away from the mold/liquid nitrogen interface the ice front would invariably slow down. At this point, the structure and/or pore size can start to differ from the macropores near the mold's exterior. For our purposes, we never encountered this problem and this potential issue was beyond the scope of the work. In order to make monolithic cylindrical samples, a brass mold was fabricated as shown in Figure 5.5. The cylindrical monoliths were approximately 8 mm in diameter and the length varied from 5-10 mm. The cylindrical monoliths were synthesized as were the samples made in a centrifuge tube, except that extra care had to be administered during the etching process. Typically the sample is placed into a plastic bottle with 3M NaOH under medium stirring overnight. As the HPC settles to the bottom of the bottle, the stir bar impacts it breaking it apart into smaller pieces. In order to prevent this and for the monolith to maintain its geometry, a porous Teflon separator was placed between the HPC monolith and the stir bar, while still maintaining the level of the NaOH solution above the HPC to facilitate the etching of the silica. The samples thus prepared were measured under nitrogen porosimetry (Figure 5.5e) and were found to have identical mesoporous properties when compared to the powder samples.

Monolithic materials with known geometries allowed for testing of the mechanical properties of the KCU-C 4-1 sample. Uniaxial stress-strain measurements were taken (Figure 5.6, vide post) at a compression rate of 0.5 N/min until a maximum force of 18

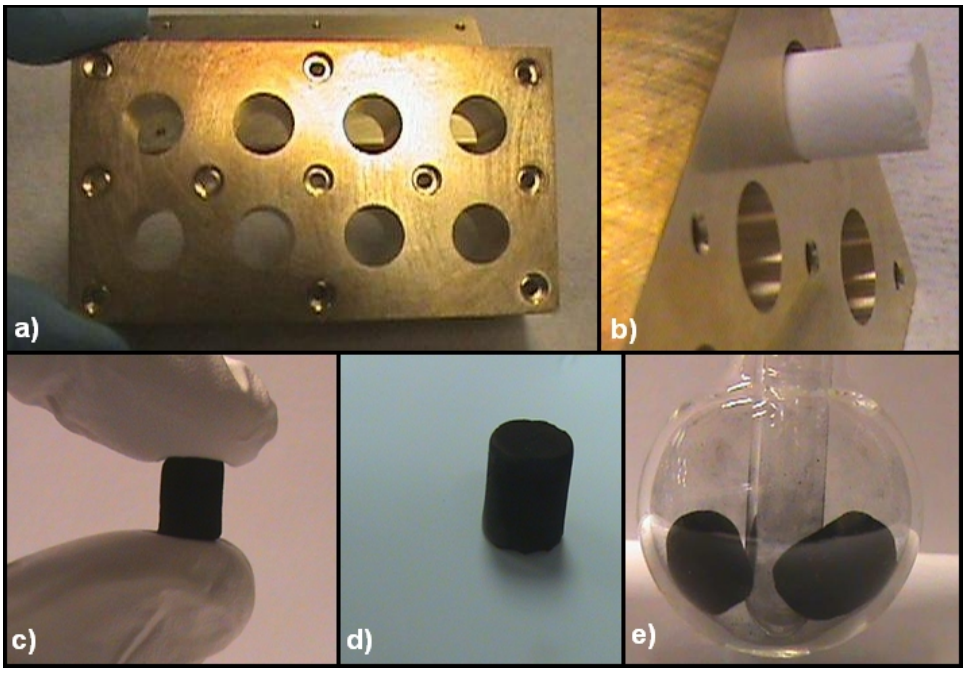

Figure 5.5: Photographic images of: (a) the brass mold employed to fabricate monolithic cylindrical samples with (b) a KCU-C 4-1 monolith shown in the mold before carbonization. The finished cylindrical monoliths (c, d) were approximately 8 mm in diameter and 10 mm in length after being pyrolyzed. The monoliths (e) are shown as they were measured under nitrogen sorption. Reproduced with permission from Estevez et al. (2013) [152].

N was reached. The modulus of the monoliths were in line for what was expected from literature values of porous carbon monoliths [180] for a given apparent density value. For our monoliths, we measured a modulus of 1 MPa, with an apparent density value of 0.09 g/mL.

5.2.3 Characterization Results – Mesoporosity

For characterization of the mesoporosity, nitrogen adsorption-desorption tests are the standard tools to obtain SSA, pore volume and mesoporous size distribution. The total

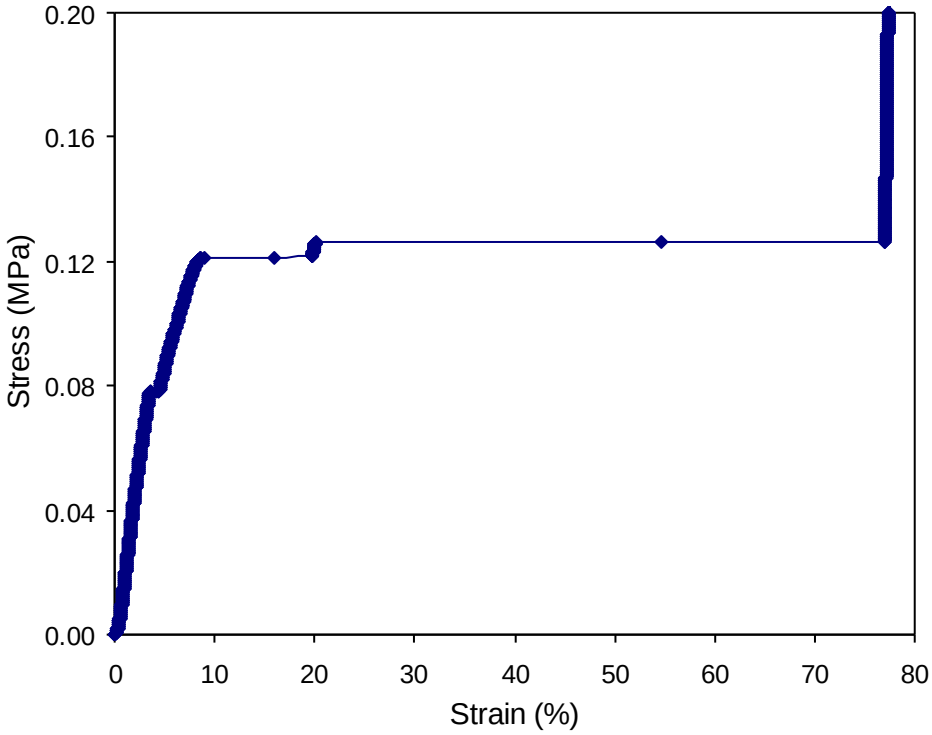

Figure 5.6: A typical compressive stress/strain plot for the HPC monoliths. In general, the stress/strain curves exhibit a behavior typical of porous cellular solids. At small strains the material behaves elastically and the slope of the curve equals the compressive modulus of the porous material. At higher strains the material collapses in brittle failure until it starts to reach a maximum compacted state, whereupon the stress starts to increase sharply. Reproduced with permission from Estevez et al. (2013) [152].

BET surface area and pore volume (excluding macropores) for a series of samples is summarized in Table 1. It is important to note that these pore volumes, calculated from N_2 sorption, for the KCU-C x-2 samples (from 3.0 - 4.1 cm^3/g) are among the highest values measured for mesoporous carbon materials [74, 159]. In contrast to macroporosity, the silica to glucose ratio and the size of silica affects the mesoporosity. For HPCs synthesized using a silica to glucose ratio of 1, the surface area and pore volume decrease as the silica particle size increases. No such dependence is seen for the silica to glucose ratio of 2, where the surface area is

Table 1. Textural characteristics of the synthesized carbons

Sample name	BET surface area (m^2/g)	N_2 adsorption pore volume (cm^3/g)
KCU-C 4-1	1316	2.3
KCU-C 4-2	1327	4.1
KCU-C 8-1	1129	2.0
KCU-C 8-2	1265	3.6
KCU-C 12-1	893	1.9
KCU-C 12-2	1216	3.0
KCU-C 20-1	841	1.9
KCU-C 20-2	1289	3.7

generally the same regardless of silica size. For a given silica particle size, the surface area and the pore volume increase as the silica to glucose ratio increases from 1 to 2. The percent increase in surface area is much more pronounced for the 12 and 20 nm silica particles (the increase for all particle sizes are 1, 11, 36 and 53% for the 4, 8, 12 and 20 nm silica, respectively).

A distinct advantage of our approach is the ability to easily control the pore sizes. For example, the size of the mesopores can be easily tuned by using different sized silica particles. Figure 5.7 shows the pore size distribution calculated using the BJH model for a series of HPCs, synthesized using different sized silica nanoparticles (4, 8, 12 and 20 nm). Note the high fidelity of the process in generating mesopores, especially for the 1:1 ratio of silica to glucose; the size of the resulting mesopores corresponds well with the size of the silica nanoparticles used in the process (Figure 5.7). This fidelity holds true for the 20 nm silica particles even for SiO_2/glucose ratio of 2. However at this higher silica/glucose ratio of 2, as the particle size decreases, aggregation of the particles during freezing leads to larger pore sizes and this is especially true for the 4 nm silica particles. Note that as the number of silica

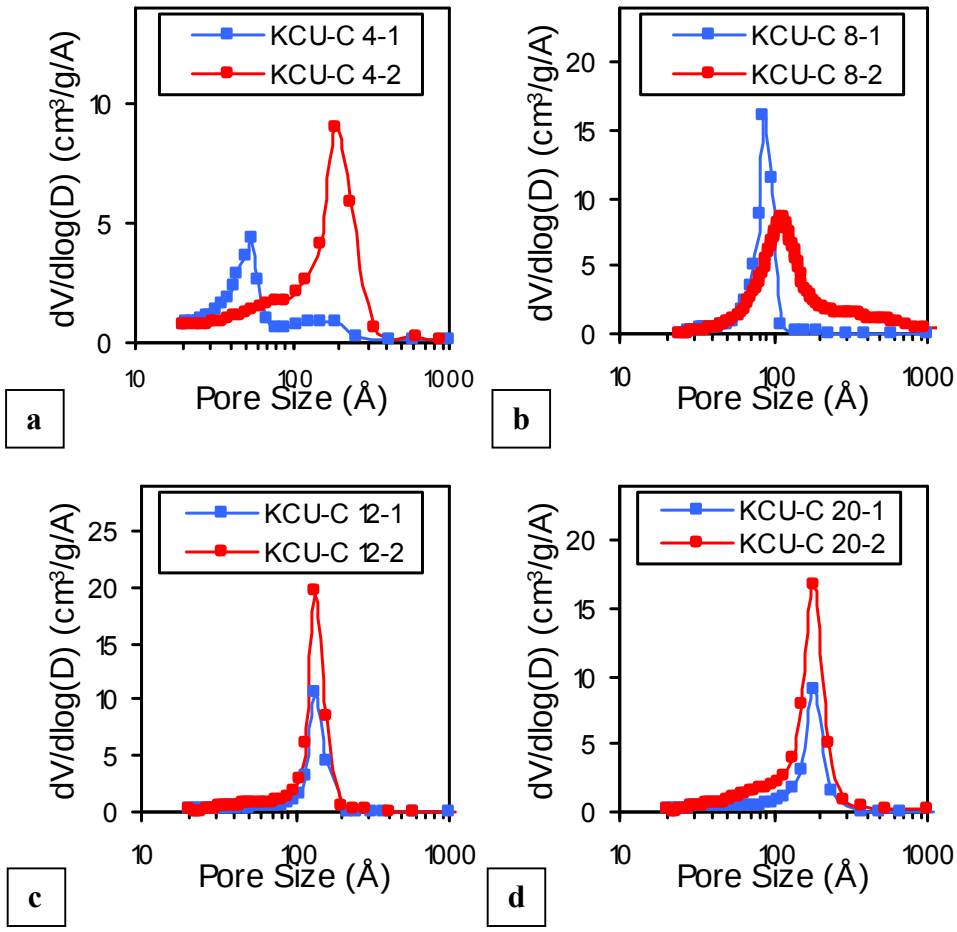

Figure 5.7: BJH pore size distributions for the KCU-C x-y samples with a colloidal template size of (a) 4 nm (b) 8 nm (c) 12 nm and (d) 20 nm. Reproduced with permission from Estevez et al. (2013) [152].

nanoparticles (relative to the glucose) increases, the amount of glucose present between the nanoparticles decreases, resulting in aggregation at higher ratios.

Our approach also offers the possibility to easily make HPCs with bimodal mesoporosity distribution, by merely starting with two different sized silica nanoparticles. By starting with a synthesis identical to that of which is described in section 4.3, the colloidal silica used was replaced by equal parts (by weight) of 4 and

20 nm colloidal silica. The *total* silica weight of both colloidal sizes was then measured and an equal part (by weight) of glucose was added to the suspension. The rest of the synthesis proceeded identically to the previous methodology employed. After the samples were thus prepared, they were characterized via nitrogen adsorption and were found to have a BET SSA of 1025 m^2/g and a mesopore volume of 2.4 cm^3/g. Figure 5.8b shows the BJH mesopore size distribution of the bimodal sample where a bimodal mesopore size distribution can clearly be seen. The smaller peak resembles the peak found for the KCU-C 4-1 sample, while the larger peak is similar to the distribution curve for KCU-C 20-1. The bimodal mesoporosity can be seen further via TEM characterization. Figure 5.8a shows a large overview area with a bimodal porosity clearly present. A higher resolution TEM image (Figure 5.8c) gives a clearer view of the individual bimodal pores and shows good agreement with the BJH distribution in 5.8b.

TEM images (Figure 5.9, vide post) were also obtained to compare against the BJH pore size distributions for all of the samples. The TEM images show good agreement with the BJH mesopore size distribution and reveal how uniform the mesopores are over the large areas imaged (for the bigger overview TEM images). The higher resolution inset images that show the best monodispersity, also match well with the narrow pore size distribution peaks on the BJH data.

The characterization of the various changes in colloidal silica and silica to glucose weight ratios, show how tunable this HPC system is. By just varying some very simple parameters, we were able to show differences in the textural characteristics of the

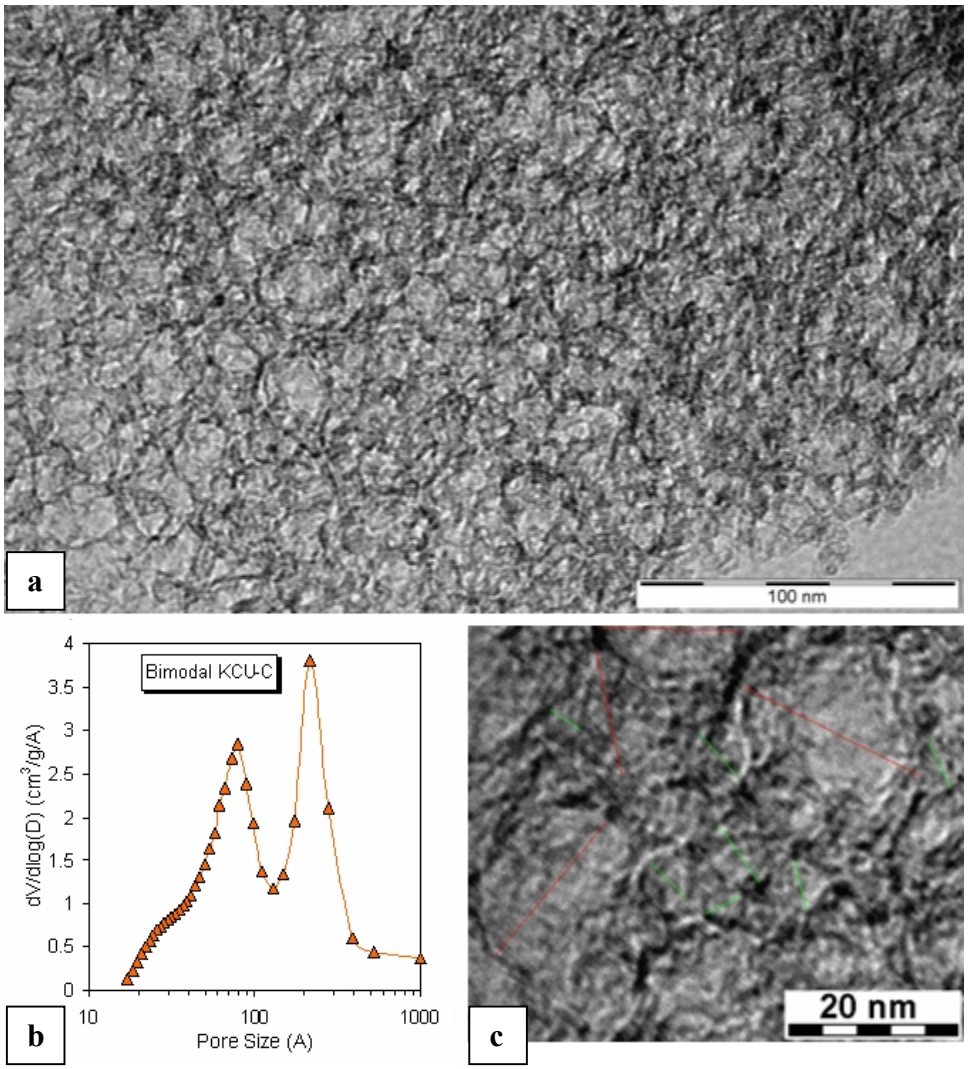

Figure 5.8: (a) TEM image of a bimodal mesoporous sample covering a broad overview. (b) BJH pore size distributions for the bimodal KCU-C sample with a colloidal template size of 4 and 20 nm that matches well with the (c) HR TEM image showing the same bimodal peaks with the 2 pore sizes' diameters denoted with a red line for the larger pores and a green line for the smaller pores to aid the viewer. Reproduced with permission from Estevez et al. (2013) [152].

synthesized carbons as well as a good range in mesopore size (6-20 nm).

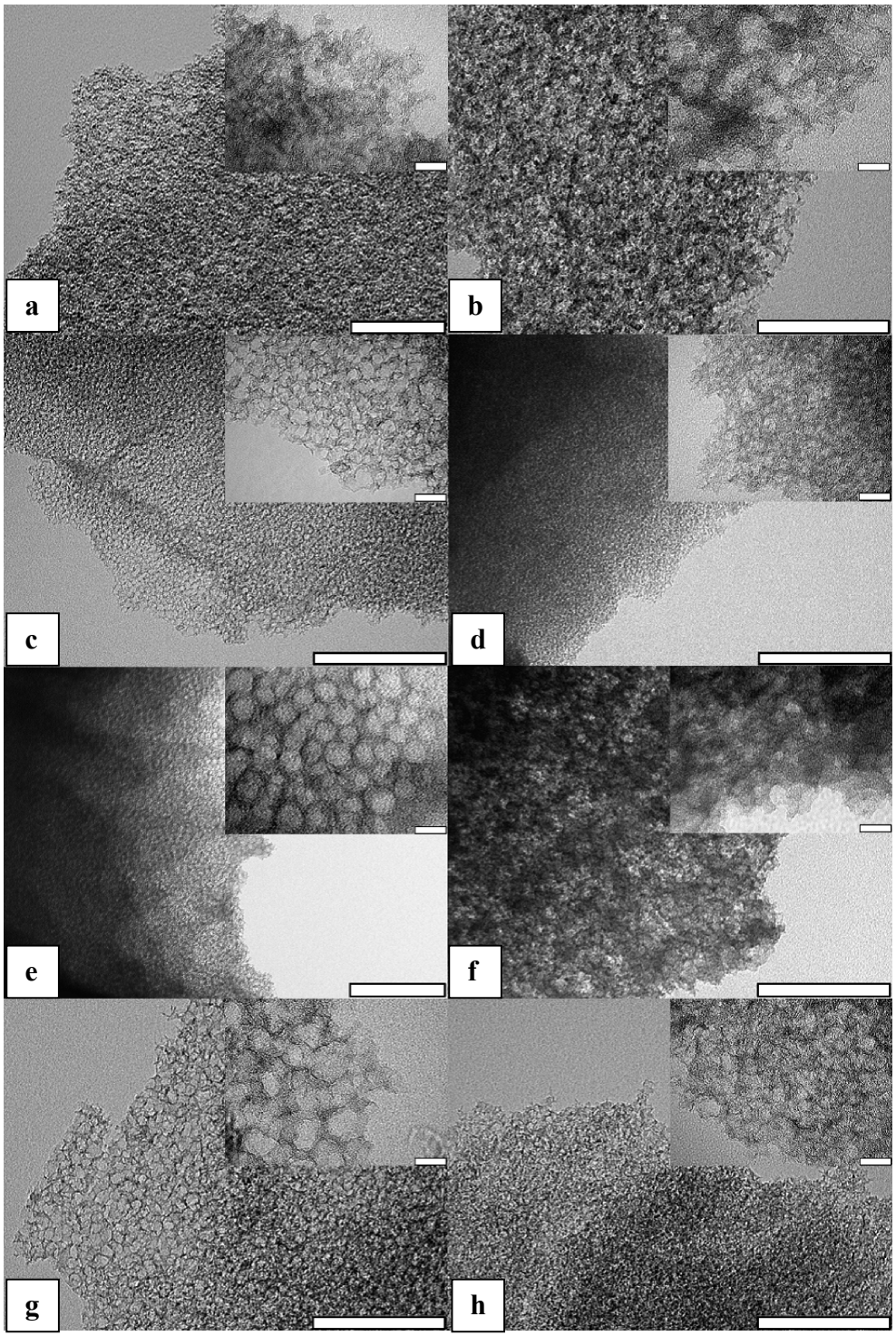

Figure 5.9: TEM images of KCU-C x-y samples. Scale bars for all images are 200 nm for the larger images and 20 nm for the inset images. (a) KCU-C 4-1 (b) KCU-C 4-2 (c) KCU-C 8-1 (d) KCU-C 8-2 (e) KCU-C 12-1 (f) KCU-C 12-2 (g) KCU-C 20-1 (h) KCU-C 20-2. Reproduced with permission from Estevez et al. (2013) [152].

5.2.4 Characterization Results – Microporosity

The specific surface area and extent of microporosity can be further increased by CO_2 activation. Under CO_2 activation, the duration and flow rate of CO_2 are important factors in determining the increase in microporosity and surface area. CO_2 activation was performed on the KCU-C 4-1 sample, for different time holds at 950 ºC, at a constant CO_2 flow rate of 50 cm^3/min. 3-4 hours of activation time was found to be optimal. The thus synthesized KCU-C 4-1-4 sample had a BET surface area of 2096 m^2/g and pore volume of 3.0 cm^3/g (Table 2), comprising of increased microporous content and broadened mesoporosity.

Exploring the data in more detail, one can see from Table 2 that the SSA goes up substantially as the activation time increases. Plainly, the CO_2 is slowly gasifying carbon atoms as has been explained previously in section 4.2.2. This is clear from not only the increasing SSA with time, but the increasing mesopore volume as well, since the gasifying of carbon atoms at the surface of the HPC scaffold should slowly broaden the mesopores as well. Further demonstrating the increasing microporosity is the nitrogen adsorption-desorption curves and the BJH mesopore size distribution (Figure 5.10,). Though the BJH model is based in the mesoporous regime the mesopore distribution curves differ as the activation times go from 0 h to 4 h. As can be seen from the edge of the limits of the BJH distribution curves (Figure 5.10a), there is a shoulder from (roughly) 2-4 nm that increases with increasing times).

Table 2. BET surface area and mesopore volume of KCU-C 4-1 samples under various physical activation times.

Sample name	CO_2 activation time (h)	BET surface area (m^2/g)	N_2 adsorption pore volume (cm^3/g)
KCU-C 4-1	0	1316	2.3
KCU-C 4-1-1	1	1703	2.6
KCU-C 4-1-3	3	1935	2.9
KCU-C 4-1-4	4	2096	3.0

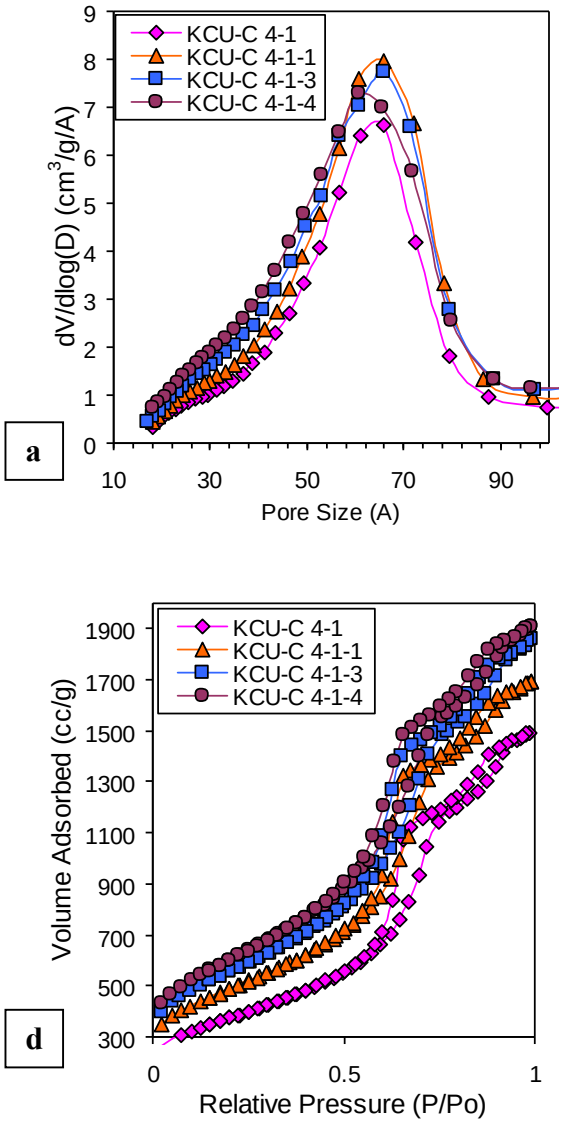

Figure 5.10: (a) BJH pore size distributions and (b) N2 sorption isotherms, for KCU-C 4-1 samples that underwent physical activation for 0, 1, 3 and 4 hours at a CO_2 flow rate of 50 cc/min. Reproduced with permission from Estevez et al. (2013) [152].

In order to measure small micropores, CO_2 adsorption-desorption curves were performed. These tests are performed at room temperature (273 K) and thus, the CO_2 gas has more energy to enter very small micropores. The pores are modeled as slits which is common practice for activated carbons and density functional theory (DFT) is used to model the micropore size distribution. Figure 5.11a shows the results of the CO_2 sorption isotherms for both activated and non activated KCU-C 4-1 samples. The activated sample KCU-C 4-1-4 was chosen as this was the optimized activated sample. As can be seen from the adsorption-desorption curves for the two samples, the sample that underwent 4 h of activation clearly shows a greater uptake of CO_2 gas immediately at low partial pressures. This is indicative of the increased microporosity of the activated sample and coincides well with the data in Table 2. Figure 5.11b shows the DFT based micropore size distribution for KCU-C 4-1-4 and KCU-C 4-1 samples. As can be observed, the KCU-C 4-1 sample already has inherent microporosity that is obtained via the carbonization process. As can be expected, when the data of the DFT distribution for the KCU-C 4-1-4 is placed on the same plot, the KCU-C 4-1-4 sample clearly shows an increased microporosity. The micropore distribution peaks also get broader and shift a bit to the right indicating an enlargement of the micropores, consistent with the activation mechanism. The last peak (centered at roughly 8.25 Å), is cut off before the right side of the curve can be revealed, which is a limitation of the testing apparatus.

5.2.5 Characterization Results – Electrical Conductivity and Atomic Structure

In order to capitalize on the potential applications HPCs have generated in the

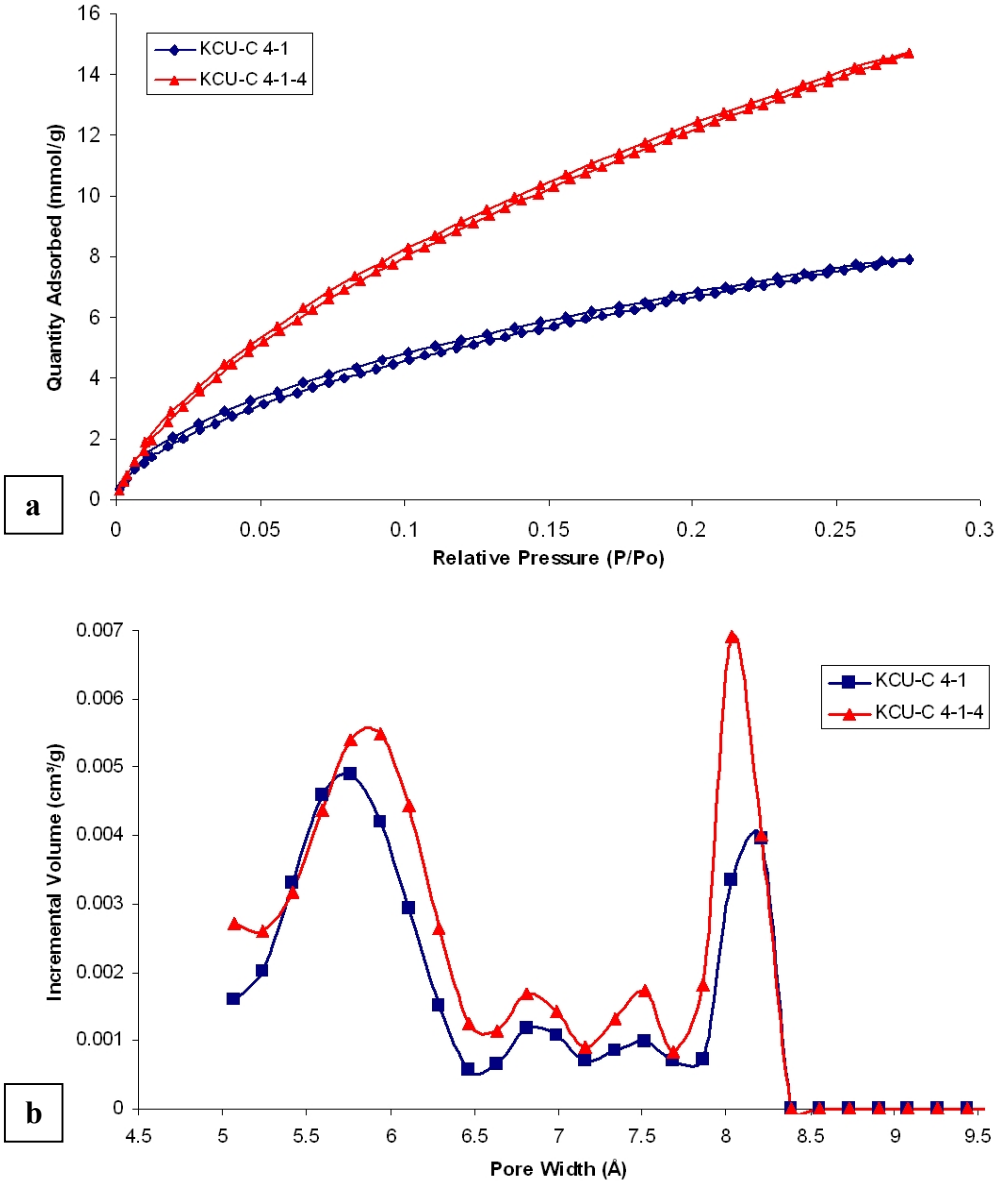

Figure 5.11: (a) CO_2 sorption isotherms for both activated (KCU-C 4-1-4) and non activated (KCU-C 4-1) samples; and (b) the resultant micropore size distribution via density functional theory (slit pores) model. Reproduced with permission from Estevez et al. (2013) [152].

literature for electrochemical converters [128, 130-135], the materials must be electrically conductive. By using a four point probe that allowed for a HPC powder to

be compacted at a certain pressure, the electrical conductivity was measured. The pressure adjustment on the powder had the effect of measuring the conductivity while in conditions that could simulate a potential application. By measuring electrical conductivity at a compressive pressure of 8000 psi on Super P® conductive carbon black (a known electrically conducting carbon nanoparticle used commercially and in research, manufactured by TIMCAL Graphite & Carbon) and repeating the same test on our HPC materials, we were able to compare our materials to a known material. At 8000 psi, the Super P® carbon black had an electrical conductivity measured to be ~38 S/cm, while our HPC materials all showed an electrical conductivity of ~7 S/cm. The four point probe set up was accurate to an order of magnitude, but much more precise as the same samples were generally within 1 S/cm of measured values. Thus, our KCU-C samples were within an order of magnitude of the high conducting carbon black nanoparticles (roughly half an order of magnitude away). These conductivity values should make our family of HPC materials good candidates for various electrochemical applications.

X-ray diffraction (XRD) and Raman spectroscopy (Raman) were utilized to elucidate the structure of the KCU-C materials. The XRD data (Figure 5.12) shows there are no peaks present that are often associated with structured graphitic carbon. Rather, the XRD spectrum reveals a HPC that is quite amorphous. This also applies to the smaller pores in our HPC materials as well, which are clearly an amorphous, non oriented nanostructure; not unlike a carbon foam. While our materials have no graphitic peak structurally, Raman (Figure 5.13) confirms the existence of both a G-band and a

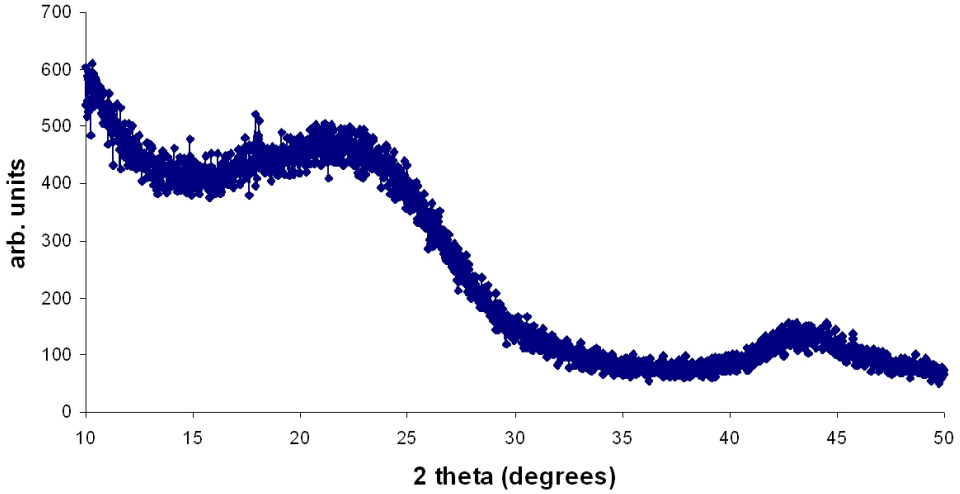

Figure 5.12: XRD spectrum of a representative KCU-C sample showing an amorphous structure.

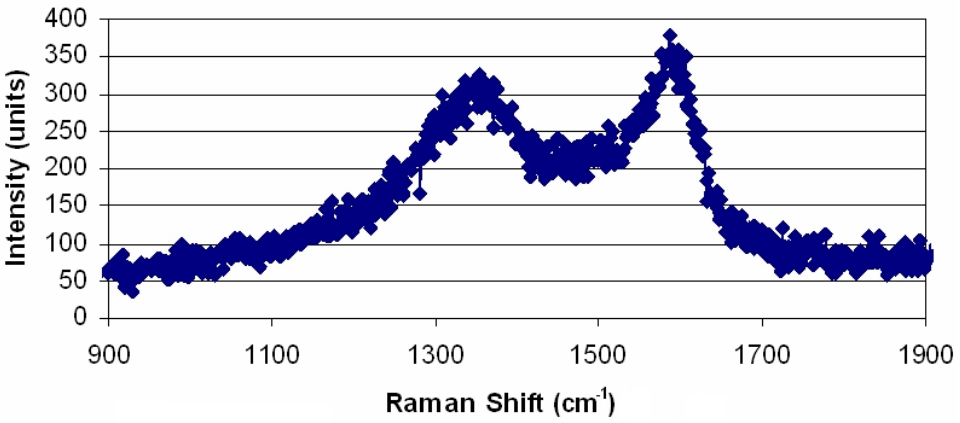

Figure 5.13: Raman spectroscopy showing both a well defined: G-band at 1582 cm^{-1} and D-band at 1332 cm^{-1}.

D-band in the resultant data.

The conductivity, XRD and Raman data all combine to suggest an amorphous HPC material that has no oriented structure, but has good electrical conductivity due to a conjugated sp^2 carbon network being present in the materials.

5.3 Conclusions

In summary, we present a novel strategy for a new family of hierarchical porous carbons (HPCs). The technique involves ice templating coupled with hard templating and physical activation, to synthesize HPCs with porosity at all different length scales (macro- meso- and micro). The technique uses green chemistry, is sustainable and scalable, and even allows for the fabrication of monolithic structures. The method results in materials with high surface area, pore volume and pore size tunability at all three length scales. The characterization of these materials as good electron conductors opens up potential electrochemical applications that can take advantage of the materials' open, vascular network of pores.

CHAPTER 6

HIERARCHICAL POROUS CARBON MATERIALS: INITIAL RESULTS AS ELECTROCHEMICAL CAPACITORS, BATTERY ELECTRODES, AND SCAFFOLDS FOR CO_2 CAPTURE

6.1 Introduction

The use of HPC materials as C-S cathodes for batteries [161], supercapacitors [119, 127, 131-133], and sorbents for CO_2 capture [138] has been explored in the literature. These various applications have typically employed different HPC systems as the prerequisites for the material's properties can vary based on the application. By employing a tunable KCU-C family of HPC materials (see chapters 4 and 5 for details) as a platform for the three applications described, a single type of porous carbon need only be employed.

6.2 KCU-C Materials used in a Carbon-Sulfur Cathode for a Li-S Battery

6.2.1 Introduction to Li-S Batteries

Li-S batteries have come under much intensive research since seminal work from the Nazar group was presented in 2009 [160]. The basic mechanism of the Li-S battery is to use sulfur as the cathode material in a lithium ion battery (LIB). With traditional lithium ion batteries, a lithium transition-metal oxide ($LiCoO_2$ being a common

example) is used as the cathode, allowing the de/re-intercalation of lithium ions at a high potential with respect to the anode (typically graphite). This intercalation reaction results in a storage capacity limited to roughly 300 mAh/g, though the highest capacity values are typically 180 mAh/g [160]. For a Li-S battery, the redox couple: $S_8 + 16Li \leftrightarrow 8Li_2S$ responsible for the charge/discharge reaction enables a theoretical capacity of 1675 mAh/g (it should be noted that whenever a specific value such as mAh/g is used in this work, the mass refers to the amount of sulfur). This high capacity, more than makes up for the smaller voltage in Li-S batteries (roughly 2/3 when compared to cathodes in traditional LIBs); this enables Li-S batteries to achieve a theoretical energy density of about 2500 Wh/Kg.

This high capacity cannot be realized by using only sulfur as the cathode, since sulfur's low electrical conductivity does not allow electrons to easily move to and from the external circuit. Nazar et al. were one of the pioneering groups to take advantage of recent developments in high surface area mesoporous carbon materials, notably CMK-3, to circumvent sulfur's poor electrical conductivity. By loading the sulfur onto the CMK-3 scaffold (via melt impregnation), the sulfur can interact with the Li ions, while the carbon scaffold allows the easy transport of electrons to facilitate the redox reaction [160-162].

6.2.2 Li-S Batteries from KCU-C Carbons

By using similar fabrication techniques as Nazar et al., we have taken our KCU-C 4-1 HPC material (described in chapters 4-5) and loaded it with sulfur (Figure 6.1). This

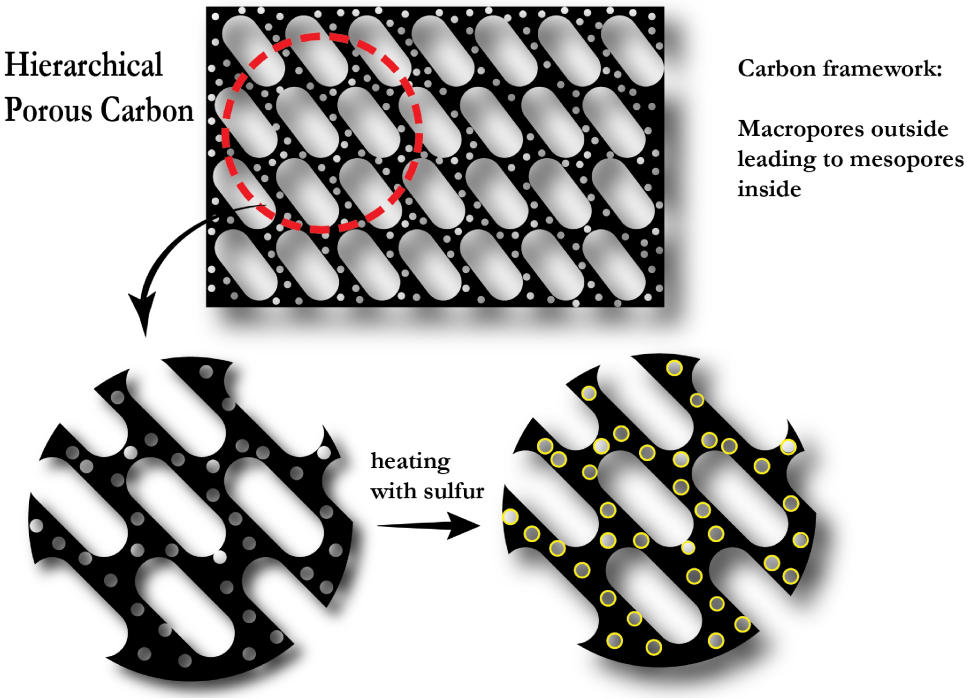

Figure 6.1: Schematic showing the fabrication of a C@S cathode via melt impregnation of sulfur onto a high surface area porous carbon material. Image created by and courtesy of Ritu Sahore.

was accomplished by combining the HPC and sulfur via mortar and pestle and then heating the mixture at 159 °C overnight. At 159 °C, the sulfur melts into a liquid phase with low viscosity, allowing the capillary forces of the mesopores to pull the sulfur into the HPC material. The eventual C@S composite was made up of 7.5 wt% of an organic binder (typically PVDF) and the remainder was equal parts sulfur and HPC carbon (~ 46% of each). The composite material was dried onto a metal substrate and stamped into discs roughly 5/8 inches in diameter and with a thickness of roughly 100 µm. This resultant cathode was assembled into a coin cell with lithium metal as the anode and 1M LiTFSi in tetraglyme (TEGDME) as the electrolyte.

The as made Li-S coin cell was charged/discharged at various C rates (0.1, 0.5 and 1

C), where the C rate is defined as: 1C being the discharge current needed to discharge the whole battery in 1 hour. For our Li-S system, the theoretical specific capacity of a Li-S system results in 1C being equal to 1675 mA per gram of sulfur employed. A higher C rate refers to a faster process where 10C is equal to a current of 16750 mA/g and conversely, a lower C rate such as 0.1C is a slower process where the current used is equal to 167.5 mA/g. Figure 6.2 shows the results of the as prepared Li-S coin cell where discharge capacity and coulombic efficiency were plotted as a function of cycle number for various C rates (0.1, 0.5 and 1 C).

6.2.3 Li-S Batteries from KCU-C Carbons – Discussion of Results

The initial data from the testing of the KCU-C 4-1 material as a C@S cathode reveal interesting results. The C rate certainly seems to have an affect on both the discharge capacity and the cell's cyclic performance. At a higher C rate, the cell appears to have a lower discharge capacity, but better cyclic performance and coulombic efficiency. The fading cyclic performance of Li-S batteries is a common issue with these systems and has to do with the polysulphide anions that are formed as intermediates of the redox reaction being soluble in the electrolyte. This results in the loss of the cathode material as the polysulphides can travel through the separator and can be reduced into solid precipitates (Li_2S_2 and Li_2S) on the lithium metal anode. This "shuttling mechanism" is beyond the scope of this work, but aids in the elucidation of the data. Thus, for our C@S cathode, it appears the lower C rate allows the Li ions to more effectively *reach* more of the sulfur material, but also allows more of the polysulphides created to more effectively dissolve into the electrolyte. At the higher C

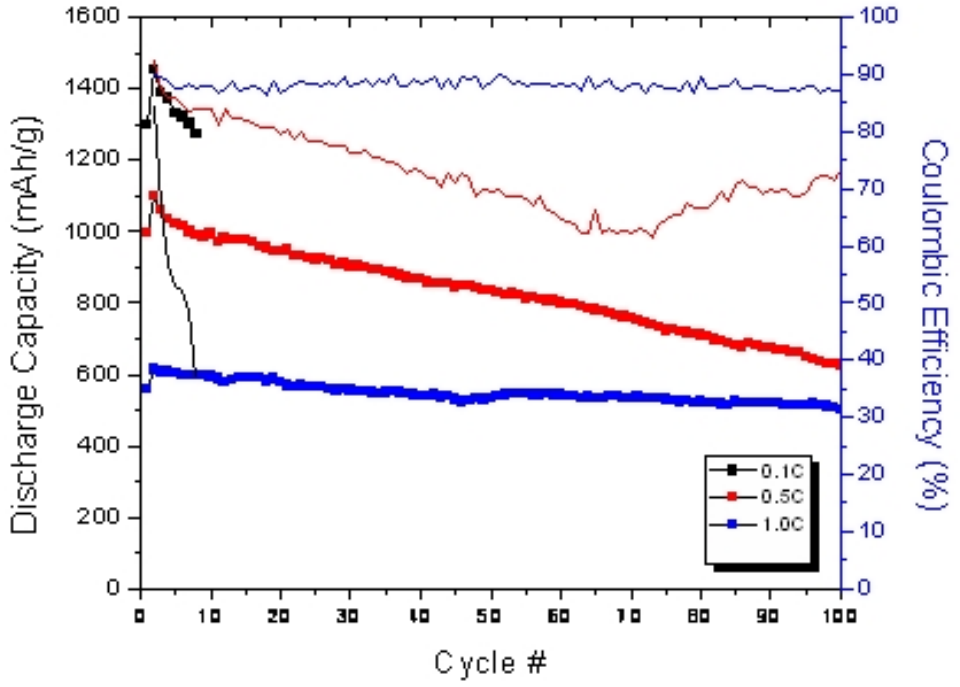

Figure 6.2: Discharge capacity and coulombic efficiency plotted as a function of cycle number for various C rates (0.1, 0.5 and 1 C).

rate of 1C, the quicker charge/discharge process allows less of the Li ions to reach the sulfur, but conversely circumvents the shuttling mechanism to some degree by speeding up the redox reactions. The coulombic efficiency (the ratio of the charge produced to the amount of charge put into the cell) supports this analysis, as an increased shuttling mechanism will negatively affect the coulombic efficiency.

Overall, these preliminary results show a great deal of promise. Though the 0.1C cells quickly lose their discharge capacity, the initial capacity is very close to the theoretical capacity. This means that if a way to mitigate the shuttling mechanism can be developed, our materials would be able to perform very close to the extremely high theoretical capacity of Li-S batteries. Even more impressive is the stable cyclic performance at 1C. Our materials' initial electrochemical performance compare well

to the better results reported in current literature [161] at this high C rate.

6.3 KCU-C Materials used in a Supercapacitor Electrode

6.3.1 Introduction to Supercapacitors

Supercapacitors (also called electrochemical capacitors or ECs) fill a niche role in the area between high power/low energy storage of traditional capacitors and low power/high energy storage of batteries (Figure 6.3) [163]. ECs have many applications including digital communication devices, digital cameras, mobile phones, electric tools, electric vehicles and storage of energy generated by solar cells [164-168]. With the recent interest in developing high surface area porous carbon materials (see section 4.1 for further details) a specific type of EC, the electrical double-layer capacitor (EDLC), has garnered interest. Here, by applying an electrical potential, the high surface areas (> 1500 m^2/g) in the carbon act as attachment points for ions of an opposite charge, storing the charge (Figure 6.4). Typically high surface area activated carbons have been the electrode of choice for commercial applications, but the ramified structure present in these carbons provides a kinetic barrier to the full use of all the potential ion attachment sites, particularly at fast charge/discharge rates (high power).

6.3.2 EDLC Electrodes from KCU-C Carbons

Our activated HPC materials with easy ingress/egress through the carbon's vascular-

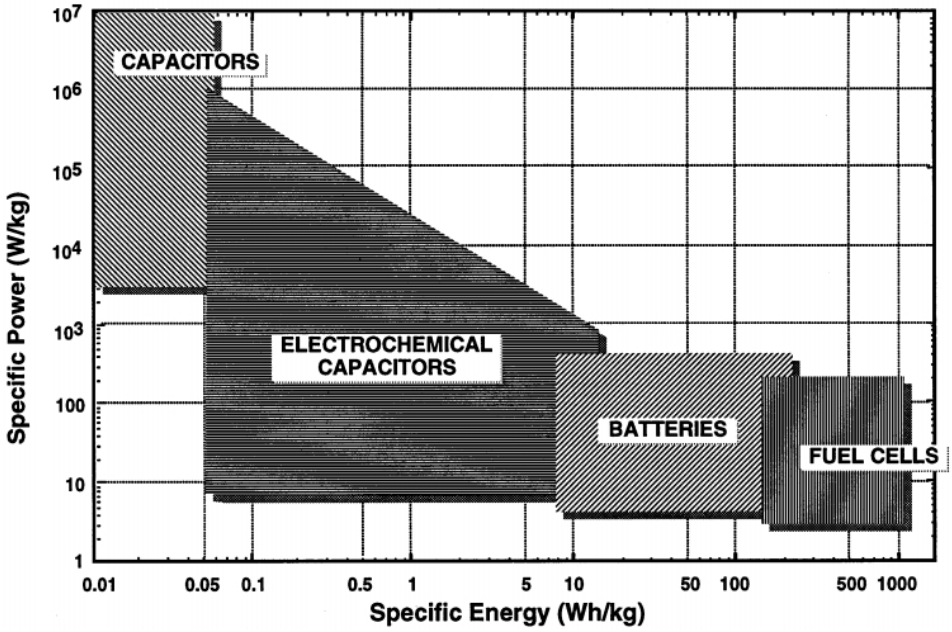

Figure 6.3: Sketch of Ragone plot for various energy storage and conversion devices. The indicated areas are rough guide lines. Reproduced with permission from Kötz et al. (2013) [163].

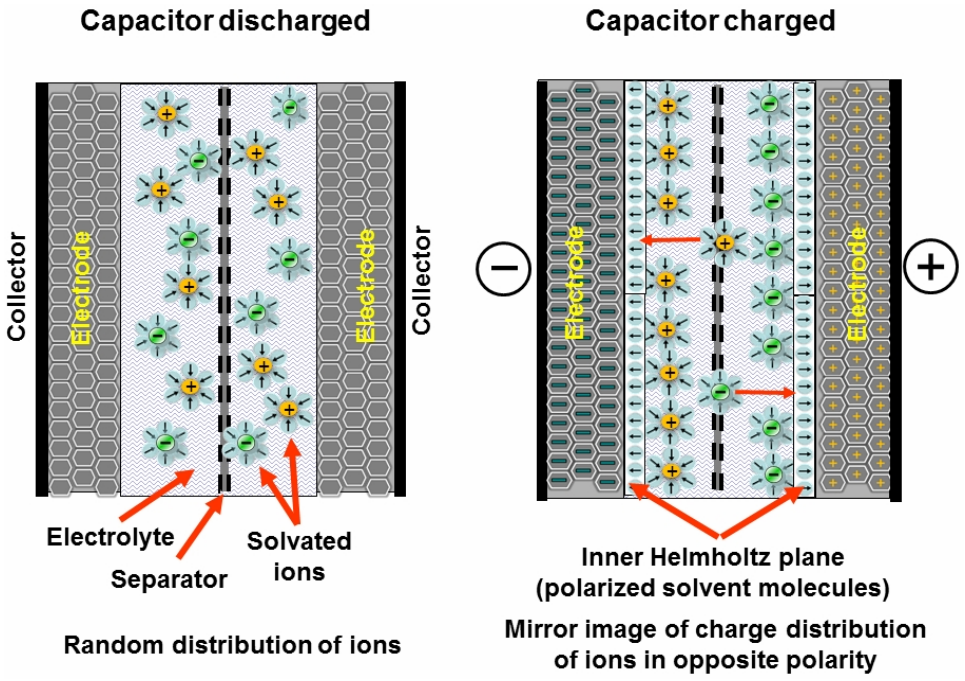

Figure 6.4: Schematic demonstrating the principle of a single-cell double-layer capacitor. Reproduced with permission under the Creative Commons Attribution-Share Alike 3.0 Unported license.

like network of hierarchical pores should minimize the kinetic barrier present in typical activated carbon materials. Thus at high power rates, our materials should still retain high specific capacitance values. The KCU-C 4-1-4 material was chosen as an initial test platform, to be used for an EDLC electrode due to its high specific surface area (~2100 m^2/g).

The electrodes were prepared by mixing 92.5 wt% KCU-C 4-1-4 and 7.5 wt% polytetrafluoroethylene (PTFE) with ethanol (60 wt% PTFE) to form a slurry. The slurry was ground using a mortar and pestle and dried by placing it in an oven at 80 ºC for an hour to obtain a dough-like paste. The paste was then rolled into a film and then pressed onto a stainless steel mesh. The electrochemical performance was characterized by cyclic voltammetry (CV). CV experiments were carried out using a three-electrode configuration with Pt as the counter electrode, Ag/AgCl as the reference electrode and with 1M H_2SO_4 as the electrolyte in the potential range between 0-1V. Different sweep rate values ranging from 2 to 200 mV/s were used. Electrochemical impedance spectroscopy (EIS) measurement was performed using a sinusoidal signal of 10 mV over the frequency range from 100 kHz to 2 mHz. The specific capacitance, energy density and power density are calculated using the following formula:

$$E = \frac{1}{8} C_S \left(V - V_{drop}\right)^2$$

$$P = \frac{1}{2} \left(V - V_{drop}\right) \left(\frac{I}{2m}\right)$$

$$C_s = 2\left(\frac{I}{m}\right)\left(\frac{dt}{dV}\right)$$

where:
m is the mass of single electrode
I is the current
V is the maximum applied potential (1V)
V_{drop} is the IR drop
dV/dt is the rate of potential decline during the discharge (excluding IR drop)
C_s is the specific capacitance of the material
E is the specific energy density
P is the specific power density

The capacitive frequency response was calculated from the EIS data using the following formula:

$$C = \frac{1}{j\mu Z} = \frac{1}{j\mu\left(\mathrm{Re}(Z) + j\,\mathrm{Im}(Z)\right)}$$

$$|C| = \left[\{\mathrm{Re}(C)\}^2 + \{\mathrm{Im}(C)\}^2\right]^{1/2}$$

$$\mu = 2\pi f$$

6.3.3 EDLC Electrodes from KCU-C Carbons – Discussion of Results

The performance of the KCU-C 4-1-4 material as an EDLC electrode was explored and the results are shown in Figures 6.5 and 6.6. Using the KCU 4-1-4 sample in a three electrode setup with 1M H_2SO_4 as the electrolyte, a specific capacitance of 221 F/g was obtained at a scan rate of 2 mV/s, with 64% retention even at a two orders of magnitude higher scan rate of 200 mV/s. These values compare favorably with the values reported in the literature for other porous carbons [164] and particularly when compared to other HPC systems [123, 131]. The sample also shows promising capacitive frequency response, calculated from electrochemical impedance spectroscopy data, retaining 50% of its maximum capacitance even when the

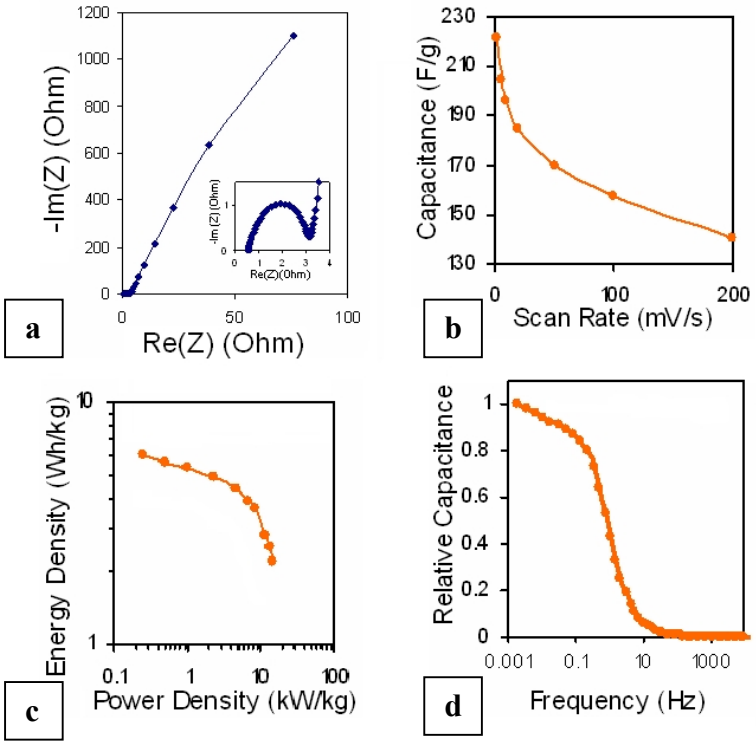

Figure 6.5: EDLC data for KCU-C 4-1-4 showing (a) a Nyquist plot using a sinusoidal signal of 10 mV over the frequency range from 100 kHz to 2 mHz, where Re(Z) represents the real impedance and Im(Z) represents the imaginary impedance, (b) the variation of specific capacitance with sweep rate, (c) a Ragone plot showing specific energy Vs. specific power and (d) the Capacitive frequency response for the electrodes. Reproduced with permission from Estevez et al. (2013) [152].

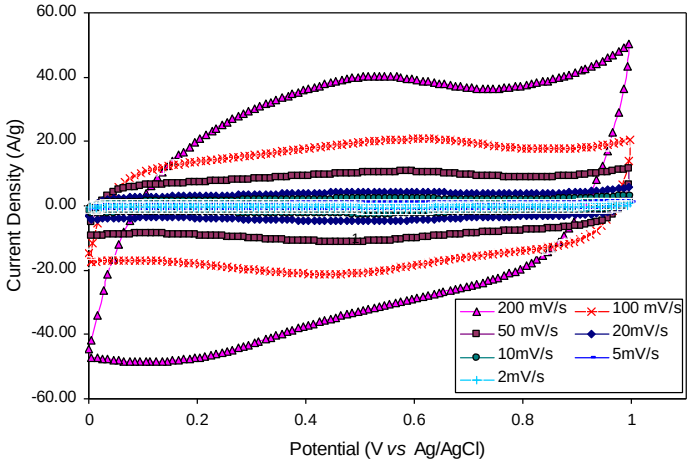

Figure 6.6: Cyclic voltammetry results for KCU-C 4-1-4 as an EDLC electrode. Reproduced with permission from Estevez et al. (2013) [152].

frequency increases to 0.73 Hz. Symmetric cells prepared from KCU-C 4-1-4 delivered a specific energy density up to the order of 6 Wh/kg and a power density in the range of 14 kW/kg, measured using galvanostatic charge-discharge testing.

The results from the KCU-C 4-1-4 EDLC show potential, as the specific capacitance of our materials compare very well with current high SSA carbon EDLCs [164]. These results become even more notable when one considers the potential optimization of the KCU-C available. The activation techniques have still not been completely honed and some development remains. As the activation process gets perfected, it will lead to higher surface areas and thus, higher specific capacitance EDLCs. Furthermore, the unusually high pore volumes present in our KCU-C materials should enable the loading of transition metal oxide nanoparticles onto the HPCs. These carbon-oxide composite materials have been shown to enhance the capacitance of the material by adding a faradaic component from a redox reaction present in various oxides.

In all, our preliminary results from using our KCU-C materials as EDLC electrodes show good results when compared to the literature and demonstrate a potential to yield even better EC materials as various procedures are developed and optimized. Further work is needed to realize the potential of these carbon systems.

6.4 KCU-C Materials used as a Solid Support for Amine Based CO_2 Capture

6.4.1 Introduction to Solid Supports for Amine Based CO_2 Capture

The capture of carbon dioxide has garnered much interest as CO_2 has been identified as one of the main contributors to climate change [169]. Of the various approaches for capturing CO_2, amine scrubbing is the industry standard. The process entails using an aqueous amine solution (25-30 wt%) to capture the CO_2 via an extensively studied zwitterion mechanism to form carbamates. The mechanism involves using temperature to control the direction of the reaction(s) (Figure 6.7). At a lower temperature of approximately 40 °C the CO_2 is captured and can be released afterwards by simply raising the temperature (to 100-140 °C) regenerating the amine, leaving it ready to reabsorb CO_2 [170].

Although amines (such as monoethanolamine) are currently used for CO_2 capture, they have some inherent issues. Typically, the amine solutions are corrosive, exacerbating production costs. Furthermore, the energy costs required for regeneration can be considerable, raising the price of generating electricity by over 60% in conventional power plants [171]. To combat these issues, amine sorbents supported onto porous scaffolds have been proposed as potential solutions to these problems [172]. Lately there has been much interest in developing multi-modal (macropore and mesopore dominated) support materials in the form of metal oxides [173-175] for amine based CO_2 capture. However, the synthesis of most of such porous metal oxide based sorbents involve the use of costly non renewable chemicals such as surfactants or pore expanders, which limits their use for large scale CO_2 capture. Our HPCs with their inherent high pore volumes and specifically, the samples with large pore sizes have the potential to be excellent alternative candidates for amine based CO_2 capture.

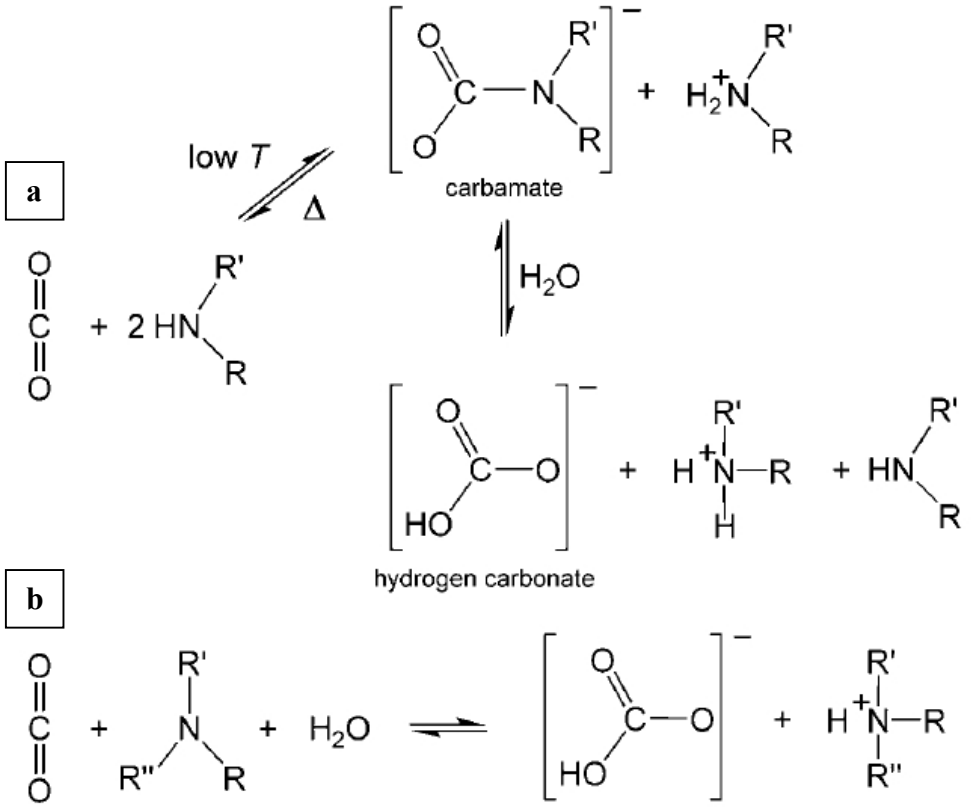

Figure 6.7: Mechanism for the chemical absorption of CO_2 via (a) primary or secondary and (b) tertiary amines. Reproduced with permission from D'Alessandro et al. (2013) [170].

6.4.2 KCU-C Carbons as Solid Support for Amine Based CO_2 Capture

As previous work within our research group has shown [171], better CO_2 capture tends to correlate with porous solid supports containing larger pores and higher pore volumes. Thus, a KCU-C 4-3 sample, with ultralarge mesopores (Figure 6.8) of ~50 nm, SSA of 760 m^2/g and a mesopore volume of 3.6 cm^3/g was synthesized. The KCU-C 4-3 sample was impregnated with polyethylenimine (PEI), achieving a PEI loading of 73 wt%. The composite sorbent preparation for amine based CO_2 capture

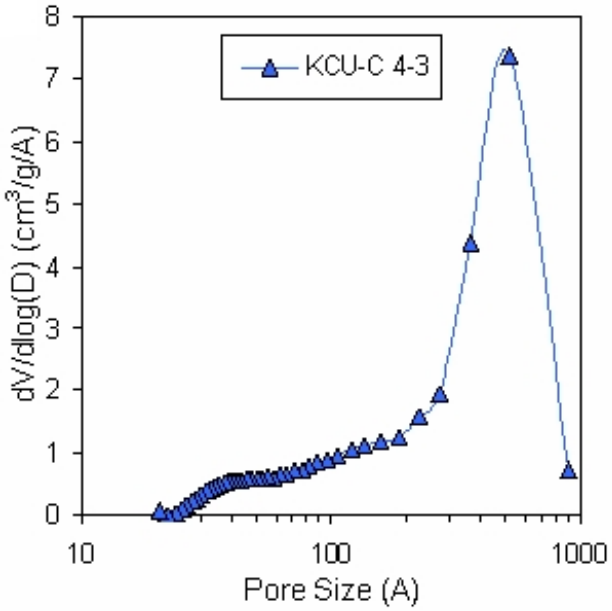

Figure 6.8: BJH pore size distribution for KCU-C 4-3 synthesized using 4nm colloidal silica and silica/glucose ratio of 3. The sample has a BET surface area of 760 m^2/g and a mesopore volume of 3.6 cm^3/g. KCU-C 4-3 sample was impregnated with amine and used for CO_2 capture. Reproduced with permission from Estevez et al. (2013) [152].

was accomplished by mixing polyethylenimine (PEI) (average M_w ~800) with absolute methanol to obtain a 20 wt% solution. The sorbents were then prepared by adding a fixed amount of this 20 wt% solution to 25 mg of KCU-C 4-3. The mixture was sonicated and kept under 70 mbar at 40 ºC for at least 12 h. CO_2 sorption measurements were performed using a TA Instruments Q500 thermal graphic analyzer. Sorption tests were performed with 1 atm of dry CO_2. For the sorption tests, 5-10 mg of the PEI-carbon composite was placed in a platinum pan, heated to 100 ºC @ 10 K/min under N_2 (40 ml/min flow rate) and held at 100 ºC for 40 min to remove any moisture and CO_2 sorbed from air. The sorbent was then cooled to 75 ºC @ 10 K/min and the gas was switched over to CO_2 while the test chamber was held at 75 ºC

for 45 min. The CO_2 capacity of the sorbents (in mmol/g) was calculated based on the weight gain of the sorbent during the adsorption. Tests were also conducted with 10% CO_2-90% N_2, under dry and moist (by passing the gas through a water bubbler maintained at room temperature) conditions.

6.4.3 KCU-C Carbons for CO_2 Capture – Discussion of Results

After the impregnated KCU-C 4-3 sample was prepared, CO_2 capture capacity was briefly evaluated. As shown in Figure 6.9, a sharp weight gain was observed after the sorbent was exposed to CO_2 in the first 5 min and 97% of the adsorption (4.1 mmol/g) was obtained after 10 min. A capacity of up to 4.2 mmol/g was achieved after 45 min, which is among the highest reported value for amine-impregnated carbon-based sorbents [176]. More importantly, for dilute CO_2 (10% CO_2-90% N_2 gas mixture), the sorption capacity measured under dry and moist conditions was the same, unlike physisorption of moist dilute CO_2 in microporous carbons, which is severely affected by the presence of moisture [177].

These initial results are quite promising in light of recent work by Schuette et al. [178]. Their work focused on analyzing the economics of using a 20% monoethanolamine (MEA) solution versus a mesoporous solid impregnated with PEI at a power plant modeled to produce 1060 tons of CO_2 per day. For the costs of capturing 90% of the CO_2, it was calculated that if the CO_2 capture capacity is less than 3 mmol/g, the economics favored the MEA solution. Conversely, as the CO_2 capture capacity exceeds 4 mmol/g, the solid sorbent becomes economically

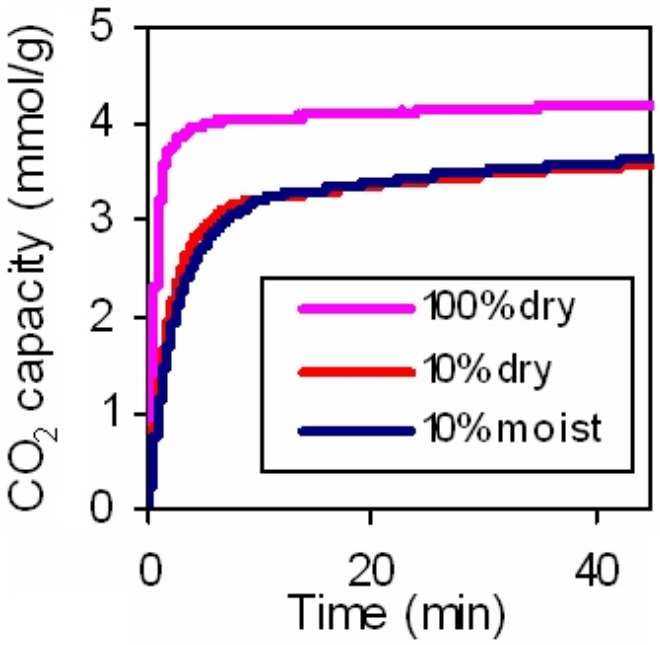

Figure 6.9: CO_2 sorption capacity of PEI-KCU-C 4-3 (73 wt% PEI) composite. Reproduced with permission from Estevez et al. (2013) [152].

favorable. Thus our PEI impregnated KCU-C 4-3 scaffold shows feasibility as a sorbent for CO_2 capture as its capacity was measured at above 4 mmol/g.

6.5 Conclusions

The successful use of our KCU-C materials in three different applications was accomplished. In all three applications: Solid support for amine based CO_2 capture, Li-S battery cathode and EDLC supercapacitor, the HPCs performed at a level that favorably compares to results from recent literature. This was achieved using the same family of HPC materials, showing the versatility of our KCU-C system. The three applications typically employ porous carbon using all three of the different length scales (micro- meso- and macropores). The porous carbons utilized in EDLCs, C@S

cathodes and solid supports for CO_2 capture are characteristically microporous, mesoporous and large mesoporous/macroporous respectively. This consistently good performance across these various length scales lends experimental credence to our claim of facile tunability in our KCU-C system.

CHAPTER 7

CONCLUSIONS AND OUTLOOK

Well dispersed nano-hybrid systems have been presented in this dissertation that can be used as a complete system to address a material's multifaceted prerequisite properties (such as in the catalyst layer of a PEM fuel cell); or that can be used as precursor materials such as the silica-glucose system that enables the facile synthesis of hierarchically porous carbon systems. Both systems use ice templating synergistically as a versatile and facile technique to imbue macroporosity and circumvent dispersity issues by *setting* an intermediate structure as a solid and then applying a process that would cause aggregation if the structure wasn't "locked" into place as a solid. The techniques and results presented in this dissertation should provide a good foundation for future work in the applications described within. Also, the versatility of the synthesis techniques demonstrated herein should provide a modifiable platform for functions and applications not covered in this work.

Achieving Mesoporosity via Ice Templating through Indirect Means

In chapter 2, a novel synthesis technique for a macroporous nano-hybrid material was proposed for a PEM fuel cell catalyst layer. One of the limitations of the resultant material was that the macropores were bigger than pores found in a typical catalyst layer. Smaller mesopores would result in higher surface areas that enable more effective loading of the platinum nanoparticles. Large macropores have the potential

to be useful, in that macropores can mitigate pore blocking issues that can affect smaller mesopores on the cathode side where water is produced. Thus a hierarchical porous system, similar to the porous carbon system introduced in Chapter 4, can perhaps prove useful, combining the advantages of both pore length scales. In order to add mesoporosity to the nano-hybrid system shown in Chapter 2, a removable template approach need not be employed as it was in the HPC materials. Simply adding a high surface area, mesoporous conducting material to the initial Nafion®, GO and Pt salt suspension before ice templating could ensure a hierarchical material with both marco- and mesopores. As a proof of concept, we incorporated hollow mesoporous silica spheres (approximately 140 nm in size), synthesized by Dr. Genggeng Qi in our research group [179], into an aqueous suspension of Nafion® and GO and then used ice templating to set the nano-hybrid material into a macroporous structure (Figure 7.1). The resultant material was a hierarchical porous structure with the mesoporous silica nanoparticles making up the macroporous walls and the Nafion-GO nanocomposite acting as the binder holding the silica together (Figure 7.2).

The silica was used as a proof of concept and for the sake of convenience, but one of the various mesoporous carbon nanoparticles that have been synthesized in the literature can be utilized in future research. There may be issues getting the carbon to disperse in an aqueous suspension, but here the amphiphilic nature of Nafion® could help disperse the hydrophobic carbon material. The mesoporous carbon could even be functionalized with oxygen groups as in the case of the GO and then reduced later alongside the GO and Pt salt. It is important to note that the suspension used for ice templating need only be well dispersed for as long as it takes it to freeze under liquid

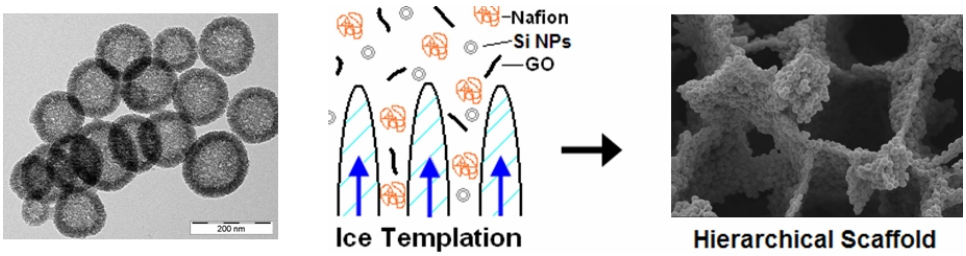

Figure 7.1: Proposed synthesis scheme in order to introduce mesoporosity into a macroporous nano-hybrid system.

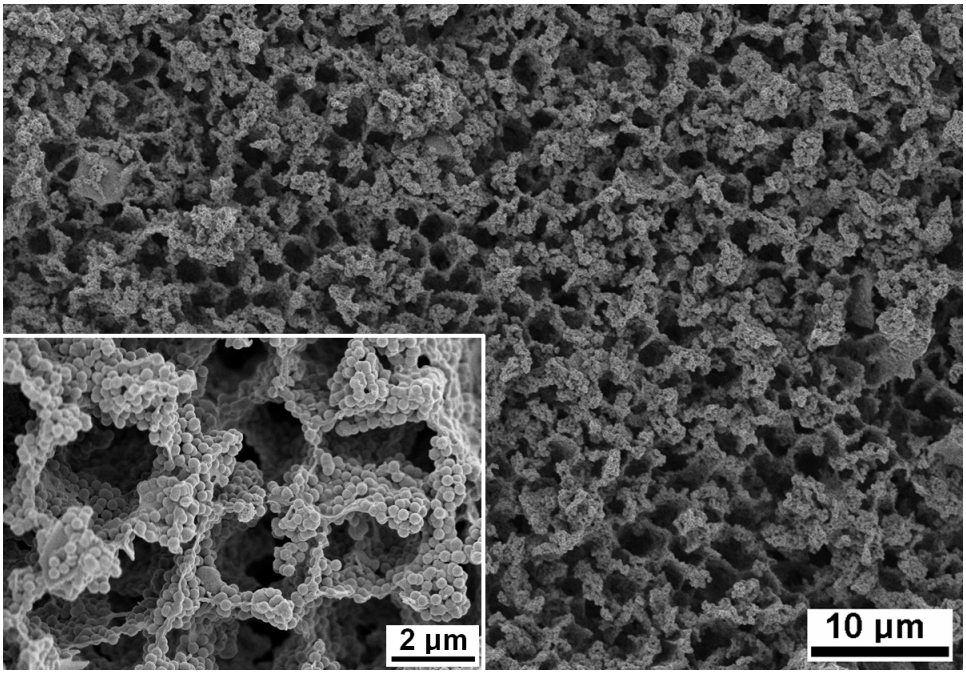

Figure 7.2: SEM images of a macroporous Nafion-GO nanocomposite, whose macroporous walls are made up of hollow mesoporous silica spheres. Larger image reveals the monolithic character of the material, while the inset image shows the 140 nm silica spheres in the macroporous walls.

nitrogen, typically a few minutes, greatly diminishing possible aggregation. Once again, with ice templating, the flexible nature of the technique enables a multitude of possible porous nano-hybrid systems. The properties of the synthesized material are quite adaptable depending on the constituent components utilized and thus, can be

optimized for the desired application.

Using Ice Templating with Other Porous Carbon Systems

Graphene (as discussed in Chapter 2) has come under considerable research due to its desirable properties including a high specific surface area (roughly 2600 m^2/g for a single GS) and ballistic electrical conductivity. A macroporous GS structure could be an effective electrochemical electrode; with the macropores providing ions easy access to the high surface area GS, while the intrinsically high electrical conductivity would allow for the facile transport of electrons throughout the structure.

By using a GO suspension and adding a hydrophilic carbon precursor such as glucose, a macroporous GO-glucose composite material could be synthesized via ice templating. Pyrolysis at a high temperature (~1000 °C) in an inert environment could enable the simultaneous carbonization of the glucose and thermal reduction of the GO into GS.

Having all the materials readily available and with the facile and inexpensive nature of ice templating, we were able to produce such a material. Figure 7.3 reveals the monolithic nature of the C-GS macroporous carbon. The glucose acts as a binder when the material is a macroporous GO-glucose composite and after being pyrolyzed, the carbon can act as firm attachment points between the graphene sheets. The higher magnification images in Figure 7.3 show that the well dispersed GO sheets stay well dispersed after ice templating and pyrolysis, which is consistent with a nanoplatelet

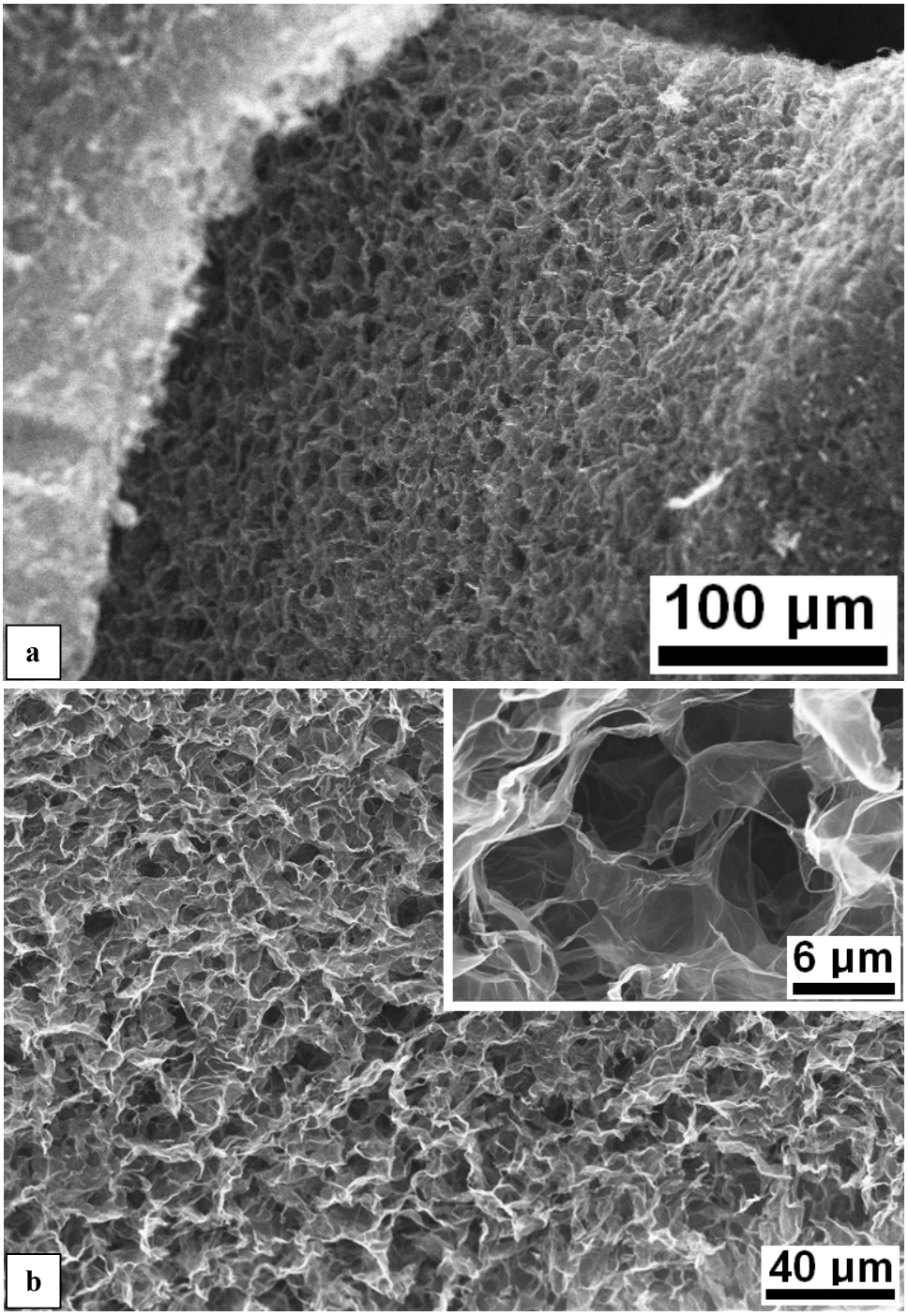

Figure 7.3: SEM image of a C-GS macroporous scaffold showing the (a) monolithic and (b) macroporous nature of the material. Inset image reveals a higher magnification SEM image where the graphene sheets are observed.

structure pinned by carbon interconnects.

APPENDIX A

NITROGEN SORPTION ISOTHERMS

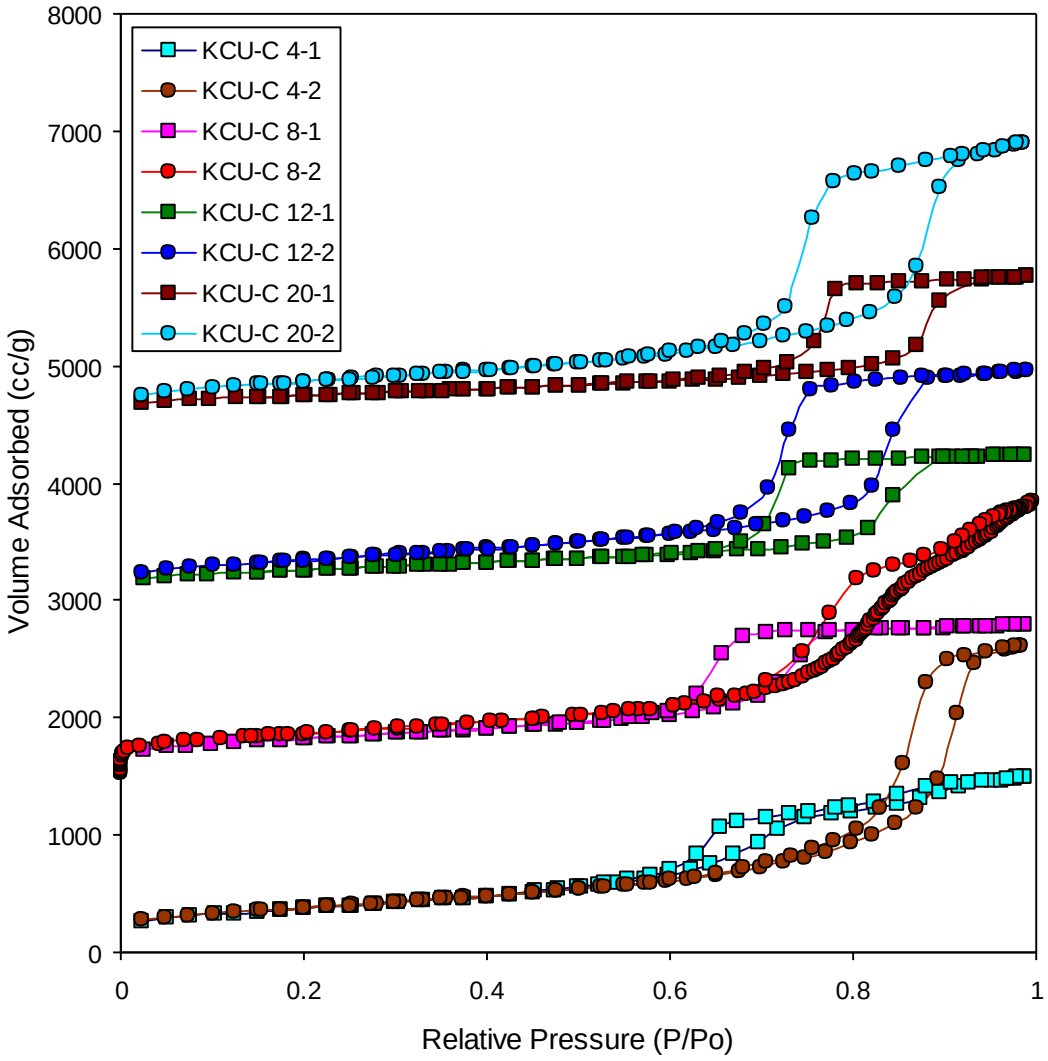

Figure A.1: Nitrogen sorption isotherms for the KCU-C samples revealed in section 5.4.3. The curves for KCU-C 8-y, KCU-C 12-y, KCU-C 20-y are offset vertically by 1500, 3000, 4500 cc/g respectively. Reproduced with permission from Estevez et al. (2013) [152].

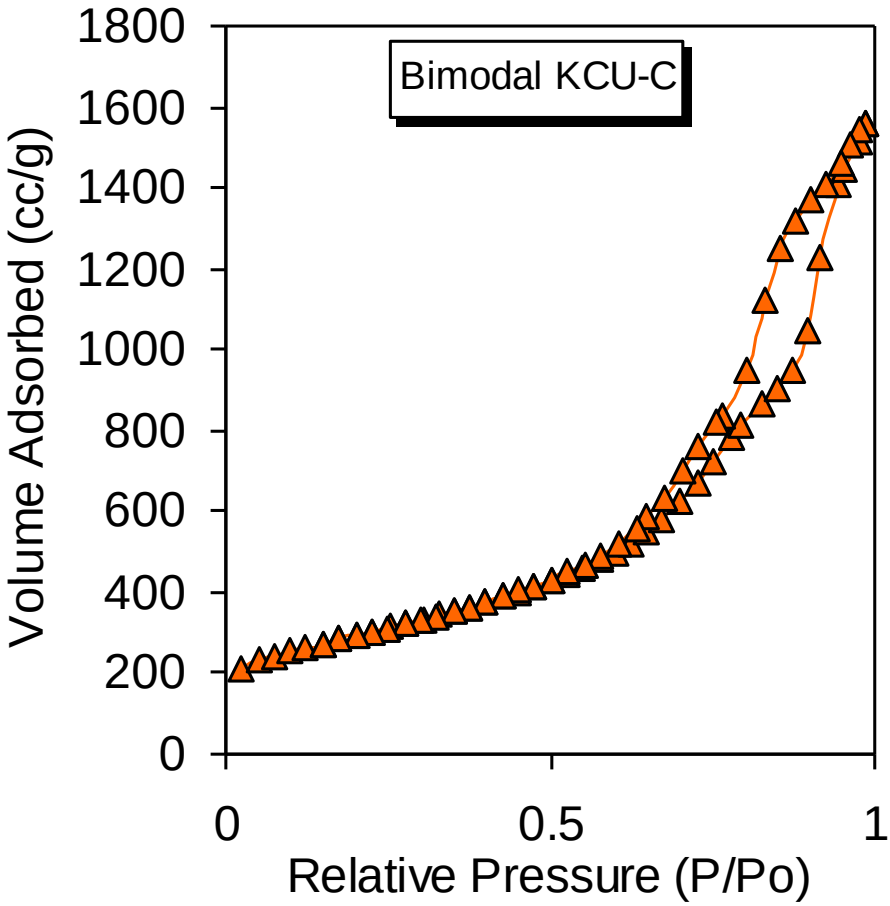

Figure A.2: Nitrogen sorption isotherms for the KCU-C bimodal sample discussed in section 5.4.3. Reproduced with permission from Estevez et al. (2013) [152].

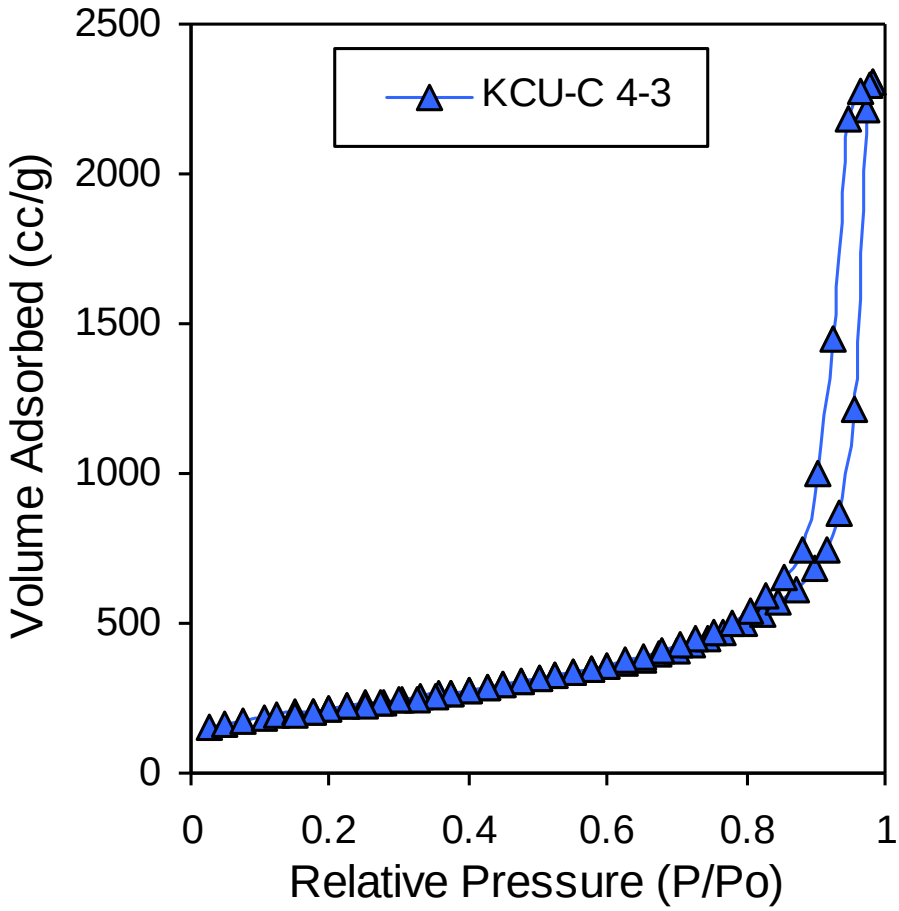

Figure A.3: Nitrogen sorption isotherms for the KCU-C 4-3 sample discussed in section 6.6.2. Reproduced with permission from Estevez et al. (2013) [152].

REFERENCES

[1] HD Wagner and RA Vaia, *Materials Today*, **7**: 32-37 (2004).

[2] E Katz and I Willner, *Angewandte Chemie (International ed. in English)*, **43**: 6042-6108 (2004).

[3] R Feynman, *Caltech Engineering and Science*, **23**: 22-36 (1960).

[4] X Zhang, B Sun and RH Friend, *Nano Letters*, **6**: 2-6 (2006).

[5] CJ Murphy et al., *J. Phys. Chem. B*, **109**: 13857-13870 (2005).

[6] DAC Brownson and CE Banks, *The Analyst*, **135**: 2768-78 (2010).

[7] TW Odom, J Huang, P Kim and CM Lieber, *Nature*, **391**: 62-64 (1998).

[8] ET Thostenson, Z Ren and T Chou, *Composites Science and Technology*, **61**: 1899-1912 (2001).

[9] T Ramanathan, S Stankovich, DA Dikin, et al., *Journal of Polymer Science: Part B: Polymer Physics*, **45**: 2097-2112 (2007).

[10] K Chrissafis, G Antoniadis, KM Paraskevopoulos et al., *Composites Science and Technology*, **67**: 2165-2174 (2007).

[11] BR Cuenya, *Thin Solid Films*, **518**: 3127-3150 (2010).

[12] S Lee and VH Perez-Luna, *Analytical Chemistry*, **77**: 7204-7211 (2005).

[13] SR Beyer, S Ullrich, S Kudera et al., *Nano Letters*, **11**: 4897-4901 (2011).

[14] S Behrens, K Rahn, W Habicht et al., *Advanced Materials*, **14**: 1621-1625 (2002).

[15] G Carja, H Chiriac and N Lupu, *Journal of Magnetism and Magnetic Materials*, **311**: 26-30 (2007).

[16] M Alexandre and P Dubois, *Materials Science and Engineering*, **28**: 1-63 (2000).

[17] R Rodriguez, R Herrera, LA Archer and EP Giannelis, *Advanced Materials*, **20**: 1-6 (2008).

[18] P Judeinstein and C Sanchez, *Journal of Materials Chemistry*, **6**: 511-525 (1996).

[19] EP Giannelis, *Advanced Materials*, **8**: 29-35 (1996).

[20] WE Gacitua, AA Ballerini and J Zhang, *Maderas. Ciencia y tecnologia*, **8**: 159-178 (2005).

[21] SS Ray and M Okamoto, *Progress in Polymer Science*, **28**: 1539-1641 (2003).

[22] O Breuer and U Sundararaj, *Polymer Composites*, **25**: 630-645 (2004).

[23] AP Kumar, D Depan, NS Tomer and RP Singh, *Progress in Polymer Science*, **34**: 479-515 (2009).

[24] S Pavlidou and CD Papaspyrides, *Progress in Polymer Science*, **33**: 1119-1198 (2008).

[25] RA Vaia, KD Jandt, EJ Kramer and EP Giannelis, *Macromolecules*, **28**: 8080-8085 (1995).

[26] A Okada, M Kawasumi, T Kurauchi and 0 Kamigaito, *Polymer Preprints,* **28**: 447 (1987).

[27] M Knite, V Teteris, B Polyakov and D Erts, *Materials Science and Engineering*, **19**: 15-19 (2002).

[28] W Bauhofer, JZ Kovacs, *Composites Science and Technology,* **69**: 1486-1498 (2009).

[29] BZ Jang and A Zhamu, *Journal of Materials Science*, **43**: 5092-5101 (2008).

[30] S Jijima, *Nature*, **354**: 56-58 (1991).

[31] X Xie, Y Mai and X Zhou, *Materials Science and Engineering*, **49**: 89-112 (2005).

[32] JJ Gooding, *Electrochimica Acta*, **50**: 3049-3060 (2005).

[33] KS Novoselov, AK Geim, SV Morozov, D Jiang et al., *Science*, **306**: 666-669 (2004).

[34] X Du, I Skachko, A Barker and EY Andrei, *Nature Nanotechnology*, **3** : 491-495 (2008).

[35] IW Frank, DM Tanenbaum, AM van der Zande and PL McEuen, *Journal of Vacuum and Technology B*, 2**5**: 2558-2561 (2007).

[36] Y Zhu, S Murali, MD Stroller et al., *Science*, **332**: 1537-1541 (2011).

[37] N Sheng, MC Boyce, DM Parks et al., *Polymer*, **45**: 487-506 (2004).

[38] T Ramanathan, AA Abdala, S Stankovich et al., *Nature Nanotechnology*, **3**: 327-331 (2008).

[39] LM Viculis, JJ Mack, RB Kaner, *Science*, **299**: 1361 (2003).

[40] H Shioyama, T Akita, *Carbon*, **41**: 179-181 (2003).

[41] S Gilje, S Han, M Wang et al., *Nano Letters*, **7**: 3394-3398 (2007).

[42] WS Hummers, Jr. and RE Offeman, *J. Am. Chem. Soc.*, **80**: 1339 (1958).

[43] S Stankovich, DA Dikin, RD Piner et al., *Carbon*, **45**: 1558-1565 (2007).

[44] H Li, S Pang, X Feng et al., *Chemical Communications*, **46**: 6243-6245 (2010).

[45] D Zhang, S Zu and B Han, *Carbon*, **47**: 2993-3000 (2009).

[46] DN Dybtsev, AL Nuzhdin, H Chun et al., *Angewandte Chemie Int. Ed.*, **45**: 916-920 (2006).

[47] P Horcajada, C Serre, G Maurin et al., *J. Am. Chem. Soc.*, **130**: 6774-6780 (2008).

[48] AC McKinlay, RE Morris, P Horcajada et al., *Angew. Chem. Int. Ed*, **49**: 6260-6266 (2010).

[49] MC Gutierrez, MJ Hortiguela, JM Amarilla et al., *J. Phys. Chem. C*, **111**: 5557-5560 (2007).

[50] CAL Colard, RA Cave, N Grossiord et al., *Advanced Materials*, **21**: 2897-2898 (2009).

[51] J Rouquerol, D Avnir, CW Fairbridge et al., *Pure & Appl. Chem*, **66**: 1739-1758 (1994).

[52] M Mozafari, F Moztarzadeh, m Rabiee et al., *Ceramics International*, **36**: 2431-2439 (2010).

[53] H Zhang and A Cooper, *Soft Matter*, **1**: 107-113 (2005).

[54] JY Ying, CP Mehnert and MS Wong, *Angew. Chem. Int. Ed.*, **38**: 56-77 (1999).

[55] RM Rioux, H Song, JD Hoefelmeyer et al., *J. Phys. Chem. B,* **109**: 2192-2202 (2005).

[56] C Yu, X Dong, L Guo et al., *J. Phys. Chem. C,* **112**: 13378-13382 (2008).

[57] SA El-Safty, M Mekawy, A Yamaguchi, et al., *Chem. Commun.*, **46**: 3917-3919 (2010).

[58] I Grigoriants, L Sominski, H Li et al., *Chem. Commun*., 921-923 (2005).

[59] XW Lou, D Deng, JY Lee and LA Archer, *Chem. Mater*., **20**: 6562-6566 (2008).

[60] Z Ma, T Kyotani, Z Liu et al., *Chem. Mater*., **13**: 4413-4415 (2001).

[61] Z Yang, Y Xia and R Mokaya, *J. Am. Chem. Soc.*, **129**: 1673-1679 (2007).

[62] B Xu, F Wu, R Chen et al., *Electrochemistry Communications*, **10**: 795-797 (2008).

[63] AR Studart, UT Gonzenbach, E Tervoort and LJ Gauckler, *J. Am. Ceram. Soc.*, **89**: 1171-1789 (2006).

[64] MC Gutierrez, ML Ferrer and F del Monte., *Chem. Mater.*, **20**: 634-648 (2008).

[65] S Deville, E Maire, G Bernard-Granger et al., *Nature Materials,* **8**: 966-972 (2009).

[66] J Halloran, *Science,* **311**: 479-480 (2006).

[67] S Deville, E Saiz, RK Nalla and AP Tomisa, *Science*, **311**: 515-518 (2006).

[68] C Suwanchawalit, AJ Patil, RK Kumar et al., *Journal of Materials Chemistry*, **19**: 8478-8483 (2009).

[69] E Munch, E Saiz , AP Tomsia and S Deville, *J. Am. Ceram. Soc.*, **92**: 1534-1539 (2009).

[70] H Zhang, I Hussain, M Brust et al., *Nature Materials*, **4**: 787-793 (2005).

[71] JA Talalay, US Patent 2,432,353 (1947).

[71] L Talalay, A Talalay, US Patent 3,238,172 (1966).

[73] A Stein, *Advanced Materials*, **15**: 763-775 (2003).

[74] Y Xia, Z Yang and R Mokaya, *Nanoscale*, **2** 639-659 (2010).

[75] H Nishihara, Q Yang, P Hou et al., *Carbon*, **47**: 1220-1230 (2009).

[76] H Marsh FR Reinoso, *Activated Carbon*, Elsevier Inc. © 2006

[77] CT Kresge, ME Leonowicz, WJ Roth et al., *Nature,* **359**: 710-712 (1992).

[78] D Zhao, J Feng, Q Huo et al., *Science,* **279**: 548-552 (1998).

[79] M Templin, A Franck, A Du Chesne et al., *Science*, **278**: 1795-1798 (1997).

[80] Y Meng, D Gu, F Zhang et al., *Chem. Mater.*, **18**: 4447-4464 (2006).

[81] R Ryoo, SH Joo, S Jun, *Journal of Physical Chemistry B*, **103**: 7743-7746 (1999).

[82] SH Joo, SJ Choi, I Oh, et al., *Nature,* **412**: 169-172 (2001).

[83] S Han and T Hyeon, *Chem. Commun.*, 1955-1956 (1999).

[84] J Lee, J Kim and T Hyeon, *Advanced Materials,* **18**: 2073-2094 (2006).

[85] MS Wilson and S Gottesfeld, *Journal of Applied Electrochemistry*, **22**: 1-7 (1992).

[86] E Antolini, *Journal of Applied Electrochemistry*, **34**: 563 (2004).

[87] ID Raistrick, JW Van Zee, RE White, K Kinoshita and HS Burney, *Proceedings of the Symposium on Diaphrams, Separators and Ion Exchange Membranes*, The Electrochemical Society: page 172 (1986).

[88] S Srinivasan, EA Ticianelli, CR Derouin and A Redondo, *J. Power Sources*, **22**: 359 (1988).

[89] EA Ticianelli, CR Derouin, A Redondo and S Srinivasan, J. *Electrochem. Soc.*, **135**: 2209 (1988).

[90] J Aizenberg, J Weaver, M Thanawala et al., *Science,* **309**: 275 (2005).

[91] X Guo and G Kim, *Plasma Chemistry Plasma Processing*, **30**: 75 (2010).

[92] S Litster and G McLean, *Journal of Power Sources*, **130**: 61 (2004).

[93] MS Wilson, US Patent 5,234,777 (1993).

[94] Z Qi, MC Lefebre, PG Pickup, *Journal of Electroanalytical Chemistry*, **459**: 9 (1998).

[95] Y Wan, KAM Creber, B Peppley and VT Bui, *Polymer*, **44**: 1057 (2003).

[96] CNR Rao, K Biswas, KS Subrahmanyam and A Govindraraj, *Journal of Materials Chemistry*, **19**: 2457 (2009).

[97] S Stankovich, DA Dikin, GHB Dommett et al., *Nature*, **442**: 282 (2006).

[98] KA Mauritz and RB Moore, *Chem. Rev.*, **104**: 4535 (2004).

[99] S Slade, SA Campbell. TR Ralph and FC Walsh, *Journal of The Electrochemical Society*, **149**: A1556 (2002).

[100] S Ansari, A Kelarakis, L Estevez and EP Giannelis, *Small*, **6**: 205 (2010).

[101] L Estevez, A Kelarakis, Q Gong et al., *Journal of the American Chemical Society*, **133**: 6122 (2011).

[102] T Matsuo, A Pavan, A Peterlin, et al., *J. Colloid Interface Sci.*, **24**: 241 (1967).

[103] KA Narh, PJ Barham and A Keller, *Macromolecules*, **15**: 464 (1982).

[104] S Deville, *Advanced Engineering Materials*, **10**: 155 (2008).

[105] BH Yoon, EJ Lee, HE Kim and YH Koh, *J. Am. Ceram. Soc.*, **90**: 1753 (2007).

[106] BH Yoon, CS Park, HE Kim, YH Koh, *J. Am. Ceram. Soc.*, **90**: 3759 (2007).

[107] VI Lozinsky, IV Bakeeva, EP Presnyak et al., *J. Appl. Polym. Sci.*, **105:** 2689 (2007).

[108] S Bandi, M Bell and DA Schiraldi, *Macromolecules*, **38**: 9216 (2005).

[109] RT Olsson, MAS Azizi Samir, G Salazar-Alvarez et al., *Nature Nanotechnol.*, **5**: 584 (2010).

[110] E Antolini, *J. Mater. Sci.*, **38:** 2995 **(**2003).

[111] M Aktary, CE Lee, Y Xing et al., *Langmuir*, **16:** 5837 (2000).

[112] W Li, M Waje, Z Chen et al., *Carbon*, **48**: 995 (2010).

[113] J Lu, I Do, LT Drzal, et al., *ACS Nano*, **9**: 1825 (2008).

[114] B Seger and PV Kamat, *J. Phys. Chem. C.*, **113**: 7990 (2009).

[115] N Shang, P Papakonstantinou, P Wang, SRP Silva, *J. Phys. Chem. C.*, **114**: 15837 (2010).

[116] S Guo, D Wen, Y Zhai et al., *ACS Nano*, **4**: 3959 (2010).

[117] J Zou, J Liu, A Karakoti et al., *ACS Nano*, **12**: 7293 (2010).

[118] SM Kwon, HS Kim and HJ Jin, *Polymer*, **50**: 2785 (2009).

[119] D-W Wang, F Li, M Liu et al., *Angew. Chem. Int. Ed.*, **47**: 373 (2008).

[120] A Taguchi, J Smatt and M Linden, *Advanced Materials*, **15**: 1209 (2003).

[121] W Chen, H Zhang, Y Huang and W Wang, *Journal of Materials Chemistry*, **20**: 4773-4775 (2010).

[122] J Balach, MM Bruno, N Gustavo Cotella et al., *Journal of Power Sources*, **199**: 386 (2012).

[123] W Xing, CC Huang, SP Zhuo et al., *Carbon*, **47**: 1715 (2009).

[124] C Song. J Du, J Zhao et al., *Chem. Mater.*, **21**: 1524 (2009).

[125] J Schuster, G He, B Mandlmeier et al., *Angew. Chem. Int. Ed.*, **51**: 3591 (2012).

[126] Y Liang, D Wu and R Fu, *Sci. Rep.*, **3**: 1119 (2013).

[127] F Xu, R Cai, Q Zeng et al., *J. Mater. Chem.*, **21**: 1970 (2011).

[128] S Wenzel, T Hara, J Janek and P Adelhelm, Energy Environ. Sci., **4**: 3342 (2011).

[129] Z Chen, J Wen, C Yan et al., *Adv. Energy Mater.*, **1**: 551 (2011).

[130] Z-L Wang, D Xu, J-J Xu et al., *Adv. Funct. Mater.*, **22**: 3699 (2012).

[131] Z Lei, N Christov and XS Zhao, *Energy Environ. Sci.*, **4**: 1866 (2011).

[132] H Jiang, PS Lee and C Li, *Energy Environ. Sci.*, **6**: 41 (2013).

[133] Z Li, Z Xu, X Tan et al., *Energy Environ. Sci.*, **6**: 871 (2013).

[134] V Flexer, N Brun, O Courjean et al., *Energy Environ. Sci.*, **4**: 2097 (2011).

[135] K Katuri, ML Ferrer, MC Gutierrez et al., *Energy Environ. Sci.*, **4**: 4201 (2011).

[136] RT Mayers, C Tsouris, JO Kiggans et al., *J. Mater. Chem.*, **20**: 8674 (2010).

[137] C Tsouris, R Mayes, J Kiggans et al., *Environ. Sci. Technol.*, **45**: 10243 (2011).

[138] GP Hao, WC Li, D Qian et al., *J. Am. Chem. Soc.*, **133**: 11378 (2011).

[139] AH Lu, GP Hao, Q Sun et al., *Macromol. Chem. Phys.*, **213**: 1107 (2012).

[140] H Nishihara and T Kyotani, *Adv. Mater.*, **24**: 4473 (2012).

[141] GS Chai, IS Shin and JS Yu, *Adv. Mater.*, **16**: 2057 (2004).

[142] S Zhang, L Chen, S Zhou et al., *Chem. Mater.*, **22**: 3433 (2010).

[143] Y Deng, C Liu, T Yu et al., *Chem. Mater.*, **19**: 3271 (2007).

[144] Z Wang and A Stein, *Chem. Mater.*, **20**: 1029 (2008).

[145] Z Wang, F Li, NS Ergang and A Stein, *Chem. Mater.*, **18**: 5543 (2006).

[146] A Taguchi, JH Smatt and M Linden, *Adv. Mater.*, **15**: 1209 (2003).

[147] RW Pekala, JC Farmer, CT Alviso et al., *Journal of Non-Crystalline Solids*, **225**: 74 (1998).

[148] J Biener, M Stadermann, M Suss et al., *Energy Environ. Sci.*, **4**: 656 (2011).

[149] H Nishihara, SR Mukai and H Tamon, *Carbon*, **42**: 899 (2004).

[150] SL Candelaria, R Chen, YH Jeong and G Cao, Energy Environ. Sci., **5**: 5619 (2012).

[151] MB Bryning, DE Milkie, MF Islam et al., *Adv. Mater.*, **19**: 661 (2007).

[152] L Estevez, R Dua, N Bhandari et al., *Energy Environ. Sci.*, **6**: 1785 (2013).

[153] S Deville, C Viazzi and C Guizard, *Langmuir*, **28**: 14892 (2012).

[154] K Xia, Q Gao, J Jiang and J Hu, *Carbon*, **46**: 1718 (2008).

[155] AB Lamb, RB Wilson and NK Chaney, *Journal of Industrial and Engineering Chemistry*, **11**: 420 (1919).

[156] M Sevilla and AB Fuertes, *Carbon*, **56**: 155 (2013).

[157] MC Gutierrez, D Carriazo, A Tamayo et al., *Chem. Eur. J.*, **17**: 10533 (2011).

[158] M Mecklenburg, A Schuchardt, YK Mishra et al., *Adv. Mater.*, **24**: 3486 (2012).

[159] A Lu, W Schmidt, B Spliethoff and F Schuth, *Adv. Mater.*, **15**: 1602 (2003).

[160] X Ji, KT Lee and LF Nazar, *Nature Materials*, **8**: 500 (2009).

[161] G He, X Ji and L Nazar, *Energy Environ. Sci*., **4**: 2878 (2011).

[162] J Schuster, G He, B Mandlmeier, T Yim et al., *Angew. Chem. Int. Ed.*, **51**: 3591 (2012).

[163] R Kotz and M Carlen, *Electrochimica Acta*, **45**: 2483 (2000).

[164] Y Zhang, H Feng, X Wu et al., International Journal of Hydrogen Energy, **34**: 4889 (2009).

[165] JR Miller, *Ectrochim. Acta*, **52**: 1703 (2006).

[166] JP Zheng, *J. Electrochem. Soc.*, **152**: A1864 (2005).

[167] C-Z Yuan, B Gao and X-G Zhang, *J. Power Sources*, **173**: 606 (2007).

[168] MN Patel, X Wang, DA Slanac et al., *J. Mater. Chem.*, **22**: 3160 (2012).

[169] PM Cox, RA Betts, CD Jones et al., *Nature*, **408**: 184 (2000).

[170] DM D'Alessandro, B Smit and JR Long, *Angew. Chem. Int. Ed.*, **49:** 6058 (2010).

[171] G Qi, Y Wang, L Estevez et al., *Energy Environ. Sci.*, **4**: 444 (2011).

[172] W Chaikittislip, H-J Kim and CW Jones, *Energy Fuels*, **25**: 5528 (2011).

[173] G Qi, L Fu, BH Choi and EP Giannelis, *Energy Environ. Sci.*, **5**: 7368 (2012).

[174] Q Wang, J Luo, Z Zhong and A Borgna, *Energy Environ. Sci.*, **4**: 42 (2010).

[175] C Chen, S-T Yang, W-S Ahn and R Ryoo, *Chem. Commun.*, 3627 (2009).

[176] CC Hwang, Z Jin, W Lu et al., *ACS Appl. Mater. Interfaces*, **3**: 4782 (2011).

[177] S Choi, JH Drese and CW Jones, *ChemSusChem*, **2**: 796 (2009).

[178] GF Schuette, EG Latimer, JB Cross and E Esen, *Fifth Annual Conference on Carbon Capture and Sequestration*, Alexandria, Virginia (2006).

[179] G Qi, Y Wang, L Estevez et al., *Chem. Mater.*, **22**: 2693 (2010).

[180] L Qiu, JZ Liu, SL Chang, Y Wu and D Li, *Nat. Commun.*, **3**: 1241 (2012).